Technische Universität München

Lehrstuhl für Biologische Bildgebung

Engineering Hybrid Optical and Optoacoustic Microscopy for Extended Depth Penetration

Paul Vetschera

Vollständiger Abdruck der von der Fakultät für Elektrotechnik und Informationstechnik der Technischen Universität München zur Erlangung des akademischen Grades eines

Doktors der Naturwissenschaften (Dr. rer. nat.)

genehmigten Dissertation.

Vorsitzender: Prof. Dr.-Ing. Klaus Diepold

Prüfer der Dissertation:

1. Prof. Vasilis Ntziachristos, Ph.D.

2. Prof. Dr.-Ing. Christian Jirauschek

3. Prof. Dr.rer.nat. Axel Haase

Die Dissertation wurde am 18. 04. 2019 bei der Technischen Universität München eingereicht und durch die Fakultät für Elektrotechnik und Informationstechnik am 23. 11. 2019 angenommen.

Abstract

Scientific discovery in biomedical optics has traditionally been driven by the search to see smaller structures, i.e. to increase resolution in order to render the invisible visible. Purely optical methods can achieve the highest resolution of any imaging technique, but they are strongly limited in penetration depth due to photon scattering in tissue, which hinders visualization of biological processes in opaque and thicker specimens. Over the past decade, scientists have been addressing this limitation with the innovative method of multispectral optoacoustic tomography (MSOT), which relies on the absorption of short laser pulses in tissue and the subsequent generation of ultrasonic waves. The method thus combines the strong optical contrast of both endogenous and exogenous absorbers in tissue with scalable acoustic resolution and penetration depth.

In the present work, an optical microscopy system is combined with MSOT to take advantage of the high resolution of optical microscopy and the high penetration depth of MSOT. This hybrid approach allows the visualization of developmental processes in model organisms such as zebrafish *(Dario rerio)* over longer lifespans that are not accessible by purely optical techniques, and may become useful for imaging cancer development, tissue regeneration and metabolic disorder. The system described in this thesis is based on single plane illumination microscopy (SPIM), which has recently become a state-of-the art light sheet microscopy technique due to its high speed and hence low photo-toxicity. The combination of SPIM and MSOT for this work is based on a broad illumination wavelength range that allows the visualization and spectral differentiation of endogenous and exogenous absorbers in deep tissue. The MSOT-SPIM system in this work is applied to the imaging of genetically expressed labels such as the green fluorescent protein in developing zebrafish with high resolution and sensitivity. As another promising approach to further boost the contrast in optoacoustic imaging, a second part of this thesis describes the work on reversibly switchable fluorescent proteins. A custom-made spectrometer built for this thesis enables the characterization of these proteins in optoacoustics, which can be a further step toward high resolution imaging of

biological processes at imaging depths unaccessible to optical microscopy. These proteins may be useful contrast agents for the hybrid MSOT-SPIM system developed in this work, as well as for other optoacoustic imaging systems in use.

Acknowledgements

Working on a PhD thesis over more so many years is a challenging endeavor that would not have been possible without the support of so many people. First of all, I want to thank my supervisor Prof. Vasilis Ntziachristos for giving me the opportunity to work in the exciting field of biomedical imaging. I highly appreciated the degree of freedom in performing research that I had at the Institute of Biological and Medical Imaging (IBMI) and all the exceptional technical and financial means to pursue scientific discovery and development.
I want to thank Dr. Murad Omar, who was my group leader and mentor most of the time of my PhD studies and always had an open door to discuss technical problems. Likewise, I want to thank Dr. Andriy Chmyrov, who took over after Murad's leave and gave a strong support with his deep expertise in optics. Sincere thanks go to Dr. Andrei Chekkoury, who introduced me into optoacoustic tomography in his setup, where I could learn many of the techniques and tricks that were used in the hybrid system. Moreover, I want to thank Dr. Benno Koberstein-Schwarz, who was working closely with me on the hybrid system and was a partner in crime in the lab. We went through many ups and downs together performing experiments with our system. I want to thank all the other Tech2See consortium members at IBMI who contributed to the successful completion of the project: Dr. Josefine Reber, Dr. Christiane Ogorek, Dr. Claudia Hildebrand, Dr. Amy Lin and Prof. Daniel Razansky. Also, I am grateful for the support of Prof. Gil Westmeyer, Dr. Hérnan Lopez-Schier, Panagiotis Symvoulidis, Laura Pola-Morell, and Gema Valera for their kind support in providing zebrafish samples.
I am deeply indepted to our collaborators from Carl Zeiss AG, in particular Dr. Tobias Schmitt-Manderbach, who was our main partner in the project and who became a second mentor working on the hybrid system. His deep expertise was a great asset in making the project a success and he was always willing to help when new technical components were needed. Likewise, I want to thank Dr. Christian Dietrich, Dr. Lars Omlor, Dr. Wibke Hellmich and Dr. Timo Mappes, who were also working closely on the project with us.

Furthermore, I'm deeply grateful for the very fruitful collaboration with the cell engineering group at IBMI, to Dr. André Stiel, Dr. Juan-Pablo Fuenzalida-Werner and Kanuj Mishra. It was a great pleasure to work with them at the boundary between engineering physics and cell biology. I wish to thank Dr. Chapin Rodriguez, who not only was a fantastic support in every aspect of scientific writing and improved my writing considerably, but also a great entertainer during lunch breaks. This great comradeship applies as well to the rest of our lunch group in the past years, especially to Antonios Stylogiannis, Ludwig Prade, Dr. Roland Boha and Dr. Hailong He - I will never forget the hilarious discussions we had during lunch breaks! Moreover, I'm indebted to Dr. Luis Déan-ben, who was an incomparable source of expertise at the institute. Whenever severe technical problems arose, Luis was willing to help and more than often could provide solutions. Finally, I wish to thank the Admin team at IBMI, in particular Susanne Stern, Silvia Weinzierl and Zsuzsanna Öszi, who made every aspect of administrative issues run so smoothly. I wish to thank Prof. Karl-Hans Englmeier, who never hesitated to support me in any academic or personal issue arising at the institute. I particularly want to thank Georg Wissmeyer, who was a strong support over the last years and a great friend to talk to in any academic and personal affair. Also, I want to thank many others institute members who I had many interesting discussions with and created a good working atmosphere: Andrei Bereznoi, Ivan Olefir, Dr. Jiao Li, Hong Yang, Yuanhui Huang, Dr. Ara Gharazyan, Dr. Gael Diot, Dr. Gali Sela, Dr. Nicolas Bezière, Dr. Andreas Bühler, Roman Shnaiderman, Johannes Rebling, Ivana Ivankovic, Ben McLarney, Dr. Matthias Schwarz, Dr. Christian Zakian, Dr. Dominik Soliman, Markus Seeger, Dr. Miguel Pleitez, Shyam Sri, Marco Mette and many more.

Finally, I'm deeply thankful to my friends and family for all their support in many aspects of life, a PhD without this strong back-up would not have been possible.

Contents

List of abbreviations

A	Aperture
AM	Amplifier
AR	Acoustic resolution
AS	Absorption spectrometer
BphP1	Bacterial Phytochrome
CAD	Computer-aided design
CL	Cylindrical lens
CNR	Contrast-to-noise ratio
CT	Computated tomography
CW	Continuous-wave
DAQ	Data acquisition
DP	Dove prism
DPF	Days post fertilization
ES	Electronic shutter
FB	Fiber bundle
FFT	Fast Fourier transform
FOV	Field of view
FP	Fluorescent proteine
FW	Filter wheel
FWHM	Full width at half maximum
GFP	Green fluorescent protein
GPU	Graphics processing unit
HOMO	Highest occupied molecular orbital
HWP	Half-wave plate
ICG	Indocyanine green
L	Lens
LMR	Light mixing rod
LUMO	Lowest unoccupied molecular orbital
MC	Microcontroller
MF	Multimode fiber

MFP	Mean free path
MIP	Maximum intensity projection
MORSOM	Multi orientation raster-scan optoacoustic mesoscopy
MRI	Magnetic resonance imaging
MS/s	Megasamples per second
NA	Numerical aperture
NIR	Near-infrared
NSOM	Near-field scanning optical microscopy
OA	Optoacoustic
OCT	Optical coherence tomography
OPO	Optical Parametric Oscillator
OR	Optical resolution
PBS	Polarizing beam splitter
PC	Personal computer
PGE	Photoacoustic generation efficiency
PVDF	Polyvinylidence difluoride
QY	Quantum yield
R	Reference chip
ROI	Region of interest
rsFP	Reversibly switchable fluorescent protein
RSOM	Raster-scan optoacoustic mesoscopy
S	Sample chip
SC	Sample chamber
sCMOS	Scientific complementary metal-oxide-semiconductor
sfGFP	Superfolder green fluorescent protein
SNR	Signal-to-noise ratio
SPIM	Single plane illumination microscopy
STED	Stimulated Emission Depletion
TFMP	Transport mean free path
TOF	Time of flight
WL	Whitelight lamp

1 Introduction

Scientific advances have traditionally been driven by the discovery of new laws. The discovery of new laws such as Newton's gravitational laws or Maxwell's fundamental equations in electrodynamics have not only altered our understanding of the universe, but they also had tremendous impact on our daily life, yielding a vast range of applications that nobody at the time could have imagined. At the same time, another major driving force in science has traditionally been the development of tools. For example, the invention of the telescope finally allowed the refutation of geocentrism, leading to the Copernican revolution. The development of the first microscope enabled the discovery of the microscopic world, including bacteria and beyond [1].

The human desire to see the unseen and the importance of the findings have led to tremendous progress in the development of microscopic tools. Mankind's search to see smaller and smaller structures by applying optical methods has led to tremendous progress in the field of optical microscopy and led to indispensable tools such as confocal and two-photon microscopy. These techniques rely on using an aperture to backscattered light outside of the focal plane. For centuries, however, the resolution of these tools has been limited by Abbe's criterion, which was regarded as defining physical limitation for more than 100 years. This limitation has only recently been overcome by the invention of super-resolution microscopy techniques such as near-field scanning optical microscopy (NSOM) and stimulated emission depletion (STED) microscopy [2, 3].

In the same way as scientists have worked to see even smaller structures, they have also struggled to see deeper into living organisms. However, because of scattering, purely optical microscopy methods cannot image deeper than 1 mm without chemical clearing [4]. This physical limitation has led to the discovery of novel contrast mechanisms which allow imaging beyond the depths that can be achieved using purely optical methods. These contrast mechanisms include the absorption of X-ray radiation, the reflection of ultrasonic waves, or the detection of

radiowaves emitted by oscillating atomic nuclei in a strong magnetic field (magnetic resonance imaging, MRI). The absorption of X-ray radiation is applied as a tool in clinical diagnostics in both planar imaging and computed tomography (CT). However, all these non-optical imaging approaches have several drawbacks compared to optical imaging [5]. X-ray radiation exhibits poor contrast in soft tissue and is strongly ionizing, which can cause genetic damage and thus cancer and other disorders. Ultrasound imaging is a state-of-the art imaging modality in clinics: it can reveal morphological details even deep within tissue, since tissue weakly scatters ultrasound. However, ultrasound imaging provides mediocre resolution and poor contrast. This limitation is due to its dependence on strong acoustic impedance mismatches, such as at the interface of tissue and bone. MRI allows deep anatomical tissue imaging with strong contrast and also functional imaging of e.g. brain activities, but it typically exhibits resolutions of ~ 1 mm and is cost intensive.

All these drawbacks of the methods mentioned show the need for a novel imaging contrast mechanism for microscopic applications that can uniquely combine strong contrast with penetration depths not accessible by purely optical methods. Recently, this niche has been addressed by a novel imaging approach: optoacoustic (OA) imaging (also referred to as photoacoustic imaging). This innovative technique relies on the absorption of short light pulses that cause thermal expansion in the sample, which then contracts and thereby generates an ultrasonic pressure wave. In this way, the method combines the strong optical contrast based on the absorption of light with the deep penetration depth of ultrasound imaging. Strong endogenous absorbers in biological tissue such as hemoglobin, melanin, waters and lipids can be used as sources of contrast depending on the illuminating wavelength. Furthermore, the method is highly scalable, allowing either high resolution based on optical focusing or penetration down to depths of 7 cm [4, 6].

In biological and medical research, state-of-the-art optical microscopy such as confocal microscopy, two-photon microscopy or single plane illumination microscopy (SPIM) are fundamental tools for scientific discovery. Microscopic tools are particularly important when addressing developmental biological processes (morphogenesis) in model organisms such as the fruit fly *(Drosophila melanogaster)*, zebrafish *(Danio rerio)* and mice [7]. Recently, zebrafish have become workhorse in the scientific community, due to abundant brood, low cost and easy accessibility to all developmental stages [8]. Consequently, zebrafish have become a model for cancer research,

metabolic disorders, immunology and tissue regeneration [9–13]. It has become a wide-spread organism for drug testing and toxicity testing on specific organs [14]. These studies rely on thin and transparent zebrafish larvae while older specimen cannot be used because they are opaque and consequently not accessible to purely optical methods. In this way, zebrafish remain unexploited as a model for studying long-term progression of disease or long term effects of drugs. Chemical clearing can render model organisms transparent, but it is restricted to *ex vivo* applications due to its high toxicity.

To overcome these limitations, next-generation microscopy tools are needed to be able to track the whole zebrafish development from larval stage to adulthood. SPIM has already successfully demonstrated its value in fast, high resolution, volumetric microscopic imaging of zebrafish in the larval stage [15], such as for imaging of the beating zebrafish heart *in vivo* [16]. As a source of contrast, specific structures of the fish are genetically labeled with fluorescent proteins (FPs) such as the green fluorescent protein (GFP). In contrast to focal spot scanning in confocal and two-photon microscopy, the light sheet illumination used in SPIM allows fast imaging and thus vastly reduces photobleaching within the sample. This is particularly important for a hybrid imaging approach, when the sample is illuminated multiple times for multi-modality data acquisition. In contrast to purely optical microscopy, optoacoustic tomography provides high-resolution imaging at unprecedented depths in juvenile and adult zebrafish when the animals have grown opaque and too thick for optical methods. Optoacoustic imaging of juvenile and adult zebrafish has already been demonstrated in several publications, but so far these images have been limited to two-dimensional sectional images [17–20], their resolution has been compromised by limited view detection [21], or they have not imaged genetically labeled structures deep in the fish [22], such as with GFP [17] and eCrimson [19]. Furthermore, the image quality in terms of resolution and contrast remains to be improved. For deep optoacoustic imaging in zebrafish, the main endogenous source of contrast is the strong absorbance of light by melanin, blood, water and lipids [23, 24].

1.1 Thesis objectives

With all the potential demonstrated in previous research, the objective of this thesis was to develop such a novel hybrid microscope combining SPIM with optoacoustic

tomography and to overcome the limitations of each modality in tracking the whole zebrafish development from larval stage to adulthood. A first proof of principle demonstrator combining SPIM and optoacoustic imaging was published by our group by Lin et al. [25], however this demonstrator did not exploit the depth imaging potential of optoacoustic imaging techniques. It could not not provide volumetric 3D images and did not demonstrate any imaging of genetic labeling with optoacoustics. In contrast to the previously published hybrid modality, the novel system described in this thesis is based on a tomographic optoacoustic approach in order to achieve the maximum imaging depth while maintaining high resolution. Furthermore, the goal is to obtain three-dimensional, volumetric hybrid images of the fish and to volumetrically demonstrate the detection of genetically labeled structures with fluorescent proteins such as GFP at unprecedented imaging depths. The tomographic approach for optocoustics is initially based on linear transducer arrays that record a high number of projections for high quality imaging. The multispectral illumination provided by the system allows multispectral optoacoustic imaging and subsequent spectral differentiation of endogenous absorbers such as melanin, hemoglobin and lipids. Further development of the system led to a switch to single-element detectors for increased sensitivity.

In the second part of this thesis, a hybrid absorption-optoacoustic spectrometer is developed to characterize reversibly switchable fluorescent proteins (rsFPs) to further increase the contrast-to-noise ratio (CNR) in optoacoustic imaging. When applied as genetic label in biological organisms, these proteins can push the CNR up to a factor of ~ 50 by either differential on- and off-switching or temporal unmixing schemes [26, 27]. Based on the characterization provided by the hybrid spectrometer, these proteins can become a useful tool for increased contrast in the hybrid MSOT - SPIM system and other optoacoustic imaging modalities.

1.2 Thesis outline

This thesis describes the design and development of such a novel hybrid imaging tool combining SPIM and optoacoustic tomography. First, this thesis describes the theoretical background of optical microscopy methods based on the defining interaction mechanisms between photons and tissue. These interaction mechanisms can be summarized by scattering and absorption (chapter 2). Moreover, the principles of optoacoustic imaging and various approaches of optoacoustic imaging

systems and their technological implementation are discussed. Chapter 3 describes the hybrid SPIM and optoacoustic tomography system that was further developed as part of this thesis. It describes in detail the SPIM and optoacoustic system based on linear transducer arrays, its implementation and multiple applications such multispectral optoacousctic imaging of water/lipid contrast in zebrafish. Chapter 4 describes the next-generation implementation of the system based on single-element transducers, which exhibit a higher sensitivity compared to array detectors. Chapter 5 deals with a newly developed hybrid absorption and optoacoustic spectrometer that is used to characterize reversibly switchable proteins. These proteins can further increase the CNR in optoacoustic imaging by using temporal unmixing schemes. Finally a conclusion is given in order to demonstrate how both the hybrid MSOT-SPIM system and the hybrid absorption-optoacoustic can create impact in biological discovery by means of high-resolution *in vivo* imaging at depths not accessible to purely optical microscopy.

2 Theoretical background

Optical tools have had a tremendous impact on biomedical research and medical treatment in the past decades. For example, the development of optical based techniques such as super-resolution microscopy [2, 3] has been paradigm changing in microscopy by overcoming the Abbe limit, stating that no structure beyond $\frac{\lambda}{2NA}$ of the incident light beam can be resolved. Also, the invention of optical coherence tomography (OCT) has revolutionized ophthalmological imaging and led to tremendous benefit to patients as a tool in clinical diagnostics [28, 29]. All these advances in research and clinical applications are based on a few physical interaction mechanisms of light and biological tissue. These fundamental interaction mechanisms can be roughly classified by scattering and absorption principles [30]. In this chapter, the principles of interaction mechanism between light and tissue are discussed. Furthermore, the fundamentals of microscopy, in particular SPIM are presented as well as the principles governing optoacoustic imaging approaches.

2.1 Light propagation in tissue

When biological tissue is irradiated by a photon, the light particle is either scattered, transmitted (only in transparent tissue at the respective wavelength) or absorbed [31]. Scattering also includes processes such as reflection, diffraction and refraction which can be summarized simplistically as certain form of scatter [30]. As an example, the body of zebrafish larvae younger than 7 days post fertilization (dpf) is mostly transparent for the human eye (i.e. in the visible wavelength range from 400 - 700 nm), but it exhibits numerous opaque melanin pigments. When fully illuminated at a wavelength of e.g. 500 nm, a high share of the incident photons is transmitted through the body, whereas another part is scattered on small internal structures and the last share is absorbed, mostly by the strongly absorbing melanin pigments on the fish surface. Figure 2.1 illustrates the interaction mechanisms between photons in the visible range and the zebrafish larva body.

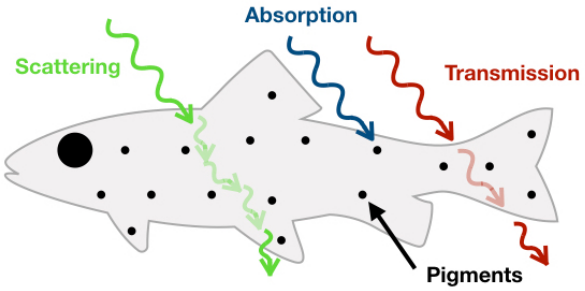

Figure 2.1: Interaction mechanisms of photons in the visible range with biological tissue.

In contrast, adult zebrafish at the age of about two months appear opaque to the human eye, due to the strong optical extinction in the fish, which is based on scattering and absorption. Thus, practically no photons pass through the fish without scattering and only very few photons pass through the fish at all due to the strong absorbance of numerous tissue components.

2.1.1 Scattering in biological tissue and implications for imaging

As introduced by this illustrative example, transparency or opacity of biological tissue strongly depend on the thickness of the sample and the composition of the tissue components. The defining characteristics of transparency or opacity of biological tissue components can be described by the sum of the individual extinction coefficients μ_e of each tissue component, which is composed by the scattering coefficient μ_s and absorption coefficient μ_a:

$$\mu_e = \mu_s + \mu_a = \sum N_s \sigma_s + \sum N_a \sigma_a \tag{2.1}$$

where σ_s, σ_a (cm^2) correspond to the individual cross sections for each scatterer and absorber respectively and N_s, N_a are the number densities (cm^{-3}) for all scatterers [5].

However, since the absolute photon extinction depends on the sample thickness, the exponential attenuation of an incident photon flux I_0 as a function of the penetration depth z can be explained by Beer's law:

$$I = I_0 \cdot e^{-\mu_e z} \tag{2.2}$$

Generally, scattering can be categorized into elastic and inelastic scattering, where a photon collides with a particle without or with energy exchange respectively. Elastic scattering in biological tissue is based on the inhomogeneous polarization densities in tissue (Rayleigh scattering) and microscopic index variations. Rayleigh scattering takes place when the colliding particle is small compared to the photon wavelength. The cross section of the particle is then inversely proportional to the photon wavelength [5, 30].

$$\sigma_{Rayleigh} \propto \frac{1}{\lambda^4} \tag{2.3}$$

Furthermore, photons are scattered isotropically in all directions with equal probability in Rayleigh scattering processes. In contrast, Mie scattering takes place when the particle size is similar to the photon wavelength and scattered photons usually propagate in the forward direction.
Inelastic scattering processes in biological tissue can be summarized by Raman scattering, where an electron is excited to a virtual state and a photon of a higher or lower energy is released immediately. The difference in wavelength / energy between the incident and the emitted photon is referred to as Stokes or anti-Stokes transition for lower or higher energy of the emitted photon, respectively. Brillouin scattering corresponds to the creation of an hypersonic wave after optical excitation [32]. In tissue, however, the scattering coefficients for inelastic scattering are orders of magnitudes lower than those of elastic scattering [30, 33].
Scattering in turbid media such as biological tissue is defined by the level of disorder of the microstructure of the medium, which shapes its macroscopic transparency or opacity. This can be characterized by two important properties of photons propagating in the turbid media, the mean free path (MFP) and the transport mean path (TMFP). Whereas the mean free path is reciprocal to the extinction coefficient

$$MFP = \frac{1}{\mu_e} \tag{2.4}$$

the transport mean path is defined as the reciprocal to the reduced scattering coefficient $\mu_s^{'} = \mu_s(1-g)$ and can be written as [4]:

$$TMFP = \frac{1}{\mu_s^{'}} \tag{2.5}$$

The anisotropy factor g denotes the degree of forward scattering, which can be

expressed as $g \approx 1$ for highly forward scattering and $g \approx 0$ for isotropic scattering [34]. In biological tissue, g is typically between 0.8 and 1. Furthermore, the mean path length is defined as the mean total distance a photon has propagated through the medium [35]. This magnitude has recently received attention in the scientific community, since it has been shown to be invariant of the microsctructure for homogenous and isotropic illumination, only depending on the surface structure and thickness of the medium. The mean free path of a photon in biological tissue is ~ 100 μm. The effect on photons scattered in tissue can be visualized by the scattering profile for photons as a function of penetration depth on a logarithmic scale. Figure 2.2 illustrates the classification of photon propagation in tissue in four regimes, which define the corresponding level of scattering [5, 36]: First, photons in the ballistic regime broadly keep their general direction - thus this range is defined from the point of entry of the photon into the medium up to the aberration limit or the MFP [4,5]. With increasing anisotropy of the photons, the quasi-ballistic regime is defined for propagation depths z, with $MFP \leq z \leq TMFP$. At propagation depths deeper than the TMFP, photon diffusion strongly increases up to depths of ~ 5 mm in the quasi-diffusive regime and subsequently the diffusive regime.

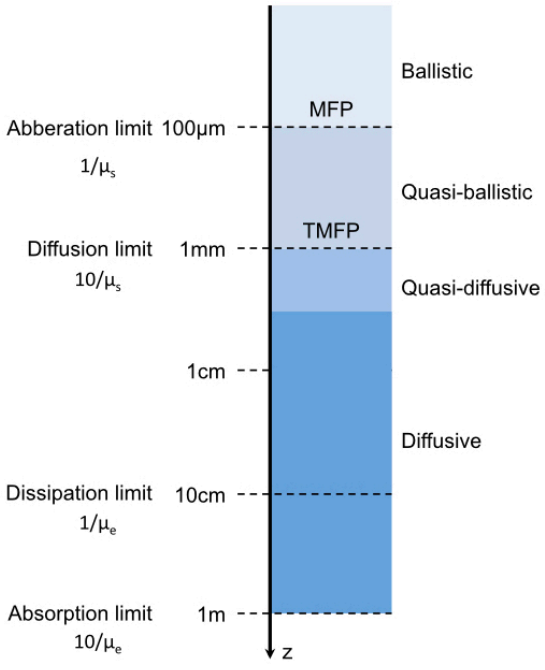

Figure 2.2: Regimes of scattering in biological tissue. Adapted from [36].

Optical microscopy techniques are strongly limited by scattering, thus the maximum penetration depth is given by the diffusion limit at 1 mm [6]. In fact, backscattered optical signals are already weak and the imaging depth is usually lower.

2.1.2 Absorption in biological tissue

Interaction mechanisms of photons with matter

The interaction mechanisms of photons with molecules along the whole electromagnetic wavelength spectrum include several physical principles which depend on the energy of the incident photon. This goes along with Einstein's famous equation $E = hf$ which demonstrates the higher energy of high-frequency/short wavelength electromagnetic waves. The interaction mechanisms of electromagnetic waves with matter can be categorized by their respective energy levels. From lower to higher energies, these mechanisms can be summarized by molecular rotation, vibration, molecular vibration, electron excitation, ionization, Compton scattering and pair production [37]. Table 2.1 gives an overview of the interaction mechanisms and their respective wavelength range / energy level.

Mechanism	**Wavelength range**	**Energy level**
Molecular rotation	Microwave	μeV - meV
Molecular vibration	Infrared	meV - eV
Electron excitation	Visible	eV
Ionization	Ultraviolett	3eV - 120 keV
Compton scattering	Low X-ray	120 - 1022 keV
Pair production	X-ray, gamma	$\geq$1.022 MeV = $2m_ec^2$

Table 2.1: Interaction mechanisms of photons with matter depending on the energy of the incident photon [38].

Since the objective of this thesis only deals with the interaction of photons in the visible and near-infrared range with biological tissue, this section only focuses on the corresponding mechanism of electron excitation. For information on the other processes, the reader is referred to [5,37,39]. The electron excitation process and the subsequent relaxation can be explained using Jablonski diagrams, which illustrate electron excitation and corresponding relaxation mechanisms in molecular orbitals (figure 2.3).

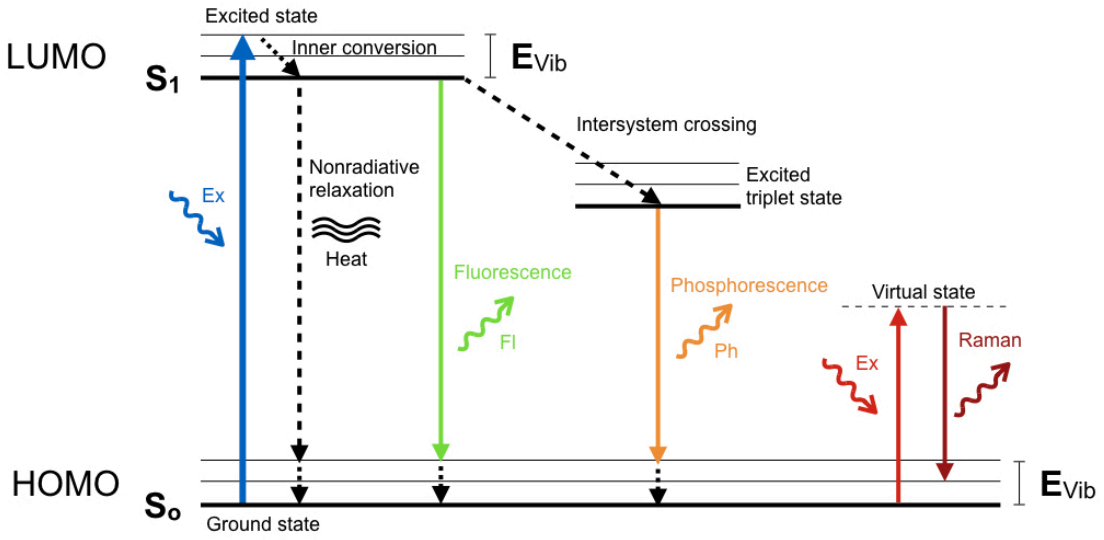

Figure 2.3: Jablonski diagram explaining electron excitation and possible relaxation mechanisms. Adapted from [5, 36, 40].

When a photon in the corresponding energy range is absorbed by a molecule, an electron of the highest occupied molecular orbital (HOMO) is excited to the lowest unoccupied molecular orbital (LUMO) [40, 41]. Consequently, the electron relaxes via non-radiative energy release to the lowest energy level of the LUMO within picoseconds. Subsequently, it then returns to the HOMO via radiative or non-radiative energy release within several nanosecond and then to the ground state within picoseconds. Radiative relaxation involves emission of another photon of lower energy, which is a process named luminescence. It can be further categorized into fluorescence or phosphorescence, depending on the electron's life time in the excited state [5]. Fluorescent relaxation happens in the timescale of several nanoseconds, after vibrational relaxations named inner conversion of the electron in the LUMO state. Phosphorescence takes place after intersystem crossing to an excited triplet state and is typically in the scale of milliseconds. The emitted photon in both relaxation processes has lower energy than the excitation photon due to the vibrational relaxations before and after the fluorescence or phosphorescence emission. The resulting difference in wavelength is referred to as Stokes shift [42]. In case of non-radiative relaxation, the energy is converted into kinetic energy of the molecule which corresponds to a local temperature increase from a macroscopic perspective. For a sufficient number of incident photons and molecules, a pressure wave is generated which can be detected as optoacoustic signal The detected optoacoustic signal is thus composed by the vibrational relaxations within the LUMO and the

non-radiative relaxations from the LUMO to the HOMO [40]. The detailed process of the pressure wave generation is explained later in this chapter. Furthermore, as explained in the section about scattering, the electron can be excited to a virtual state with immediate relaxation and emission of a photon (Raman scattering). In that case, the emitted photon can be of higher or lower energy than the incident photon, depending on the initial vibrational energy level of the electron in the HOMO state. Again, the difference in wavelength is referred to as Stokes transition when the emitted photon is of lower energy. In case of higher energy, the difference is referred to as anti-Stokes shift [5].

Absorption and its use as contrast mechanism

Based on the different energy gaps between the ground and the excited state as well as different vibrational and rotational levels, molecules exhibit distinct levels of absorption for each incident wavelength in the respective energy range (for electron excitation, visible and near-infrared). Over sufficiently broad illuminating wavelength ranges, this allows to spectrally distinguish between different molecules that absorb in the electron excitation range and the absorption spectrum of the molecule can be regarded as its respective "fingerprint". In biological tissue, the most predominant absorbers in the visible range are melanin and oxygenized and de-oxygenized hemoglobin, in the near-infrared region lipid as well as water [23, 36]. Figure 2.4 shows the absorption spectra of these predominant tissue components. As can be seen, the absorption coefficient of melanin and hemoglobin in the visible range (400 - 700 nm) is stronger by approximately two orders of magnitude than the one of other tissue components such as lipid and water. Thus, hemoglobin and melanin are the main sources of endogenous contrast. However, melanin is usually strongly localized e.g. in the skin or on the retina, thus it is usually not a major source of contrast in deeper layers of biological samples [23].

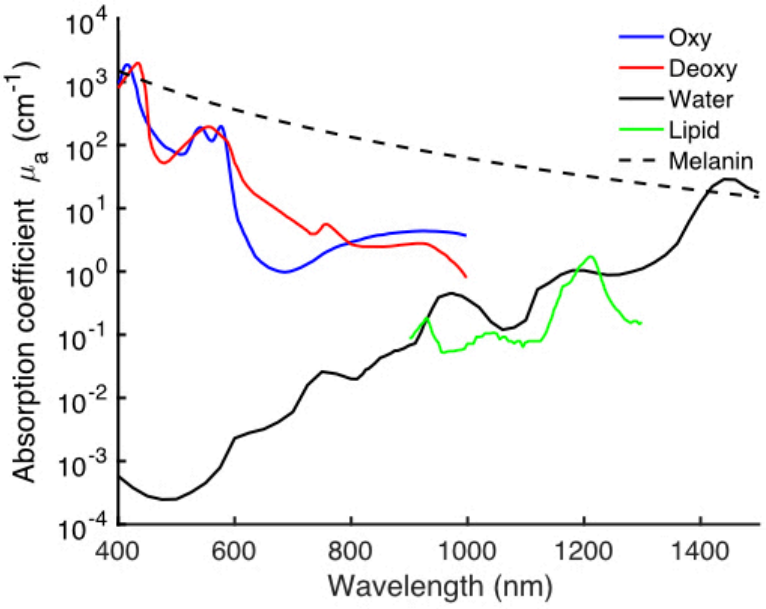

Figure 2.4: Spectra of the prevalent absorbers in biological tissue: Oxy and deoxy hemoglobin, melanin, lipids, water. Data from [43–46].

Strong exogenous sources of contrast include nanoparticles, organic dyes and fluorescent and non-fluorescent proteins [23, 24, 47]. Nanoparticles such as golden nanoparticles can be particularly designed to generate strong optoacoustic signals but so far they are restricted to preclinical imaging [23, 48]. In contrast, organic dyes such as indocyanine green (ICG) and methylene blue can be injected into the sample or the patient as exogenous source of contrast *in vivo* even for clinical applications. Fluorescent proteins such as GFP have however the unique ability to be genetically expressed at specific regions of the specimen, thus allowing to be used as a highly accurate source of contrast for *in vivo* optical microscopy [49, 50]. The key characteristics of FPs are their respective absorption and fluorescence emission spectrum, which restrict the illuminating wavelength range for imaging applications. The absorption and the emission spectrum are however mirrored, due to the Stokes shift between the incident and the emitted photon based on vibrational relaxation which takes place before fluorescence relaxation [42]. The difference in energy of the incident and emitted photons can thus be directly seen in the shift of the absorption and emission peaks of the respective spectra. As an example, figure 2.5 illustrates the mirrored absorption and emission spectrum of eGFP (enhanced GFP) and the corresponding Stokes shift.

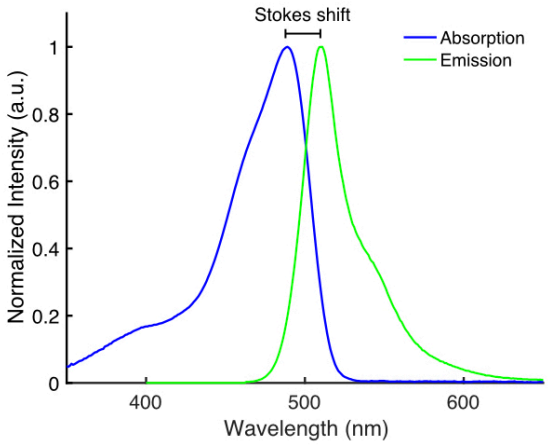

Figure 2.5: Mirrored absorption and fluorescence emission spectra of eGFP (enhanced GFP) and the corresponding Stokes shift. Data from [51].

The FPs used in fluorescent microscopy however usually exhibit a high quantum yield (QY), thus a high share of the incident energy is transferred into the fluorescence relaxation pathway and not available for non-radiative relaxation. For example, wild-type GFP has a QY of about 77 %, the widely-used eGFP exhibits a QY of 60 % [52, 53]. Thus both GFP and eGFP only exhibit weak photoacoustic generation efficiency (PGE). Hence, to detect fluorescent proteins like GFP in optoacoustics, either high pulse energies in the illumination or a high acoustic detection sensitivity are needed. However, genetically labeled FPs such as eGFP have already been successfully used as sources of contrast in optoacoustic imaging [17, 54, 55].

2.2 Optical microscopy imaging principles

In the previous section, the influence of scattering and absorption on light propagation was discussed. These two factors limit light propagation in biological tissue and also determine the current limitations of optical microscopy techniques. The two major characteristics of any microscopic imaging modality are resolution and penetration depth, which allow the classification of contemporary microscopic imaging systems.

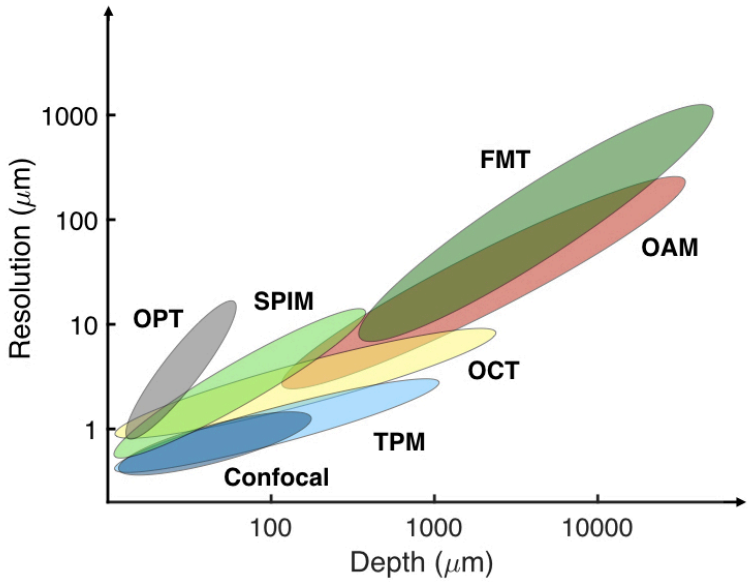

Figure 2.6: Classification of microscopic imaging modalities (excluding super-resolution modalities). FMT: Fluorescence molecular tomography, OAM: Optoacoustic mesoscopy, OCT: Optical coherence tomography, OPT: Optical projection tomography, SPIM: Single plane illumination microscopy, TPM: Two-photon microscopy. Adapted from [4, 6, 29, 36].

As illustrated in figure 2.6, purely optical microscopy techniques such as two-photon microscopy and confocal microscopy can achieve the highest resolutions up to the diffraction limit of $\sim \lambda/2$, however their penetration depth is strongly limited by scattering and absorption. On the other hand, modern imaging modalities like fluorescence molecular tomography (FMT) and optoacoustic mesoscopy do no achieve the same resolution, but can penetrate deep into tissue up to depths of several cm [4, 6]. In this section, the principles of the predominant optical microscopic imaging modalities and their applications are briefly explained.

2.2.1 Confocal microscopy

Conventional (fluorescence) microscopy methods are large affected by backscattered light that is emitted from out of focus planes. This changed dramatically when the first confocal microscope was introduced by Minsky's patent [56]. The basic idea of a confocal microscope was to block any out of focus backscattered light by a pinhole. With this approach, not only the signal-to-noise ratio (SNR) of the image can be improved, but also the resolution is subsequently only limited by the diameter of the focal spot of the incident light beam. Thus, the diffraction-limited resolution d_f for the confocal microscope is limited by the numerical aperture (NA)

of the objective and the wavelength λ of the light beam [57, 58]:

$$d_f = 1.22\frac{\lambda}{NA} \tag{2.6}$$

Confocal microscopes are usually based on laser illumination due to high monochromaticity and throughput efficiency. The implementation of confocal microscopes can vary e.g. by sample scanning, beam scanning or by spinning discs [57, 58]. Applications are often based on fluorescent labels attached to antibodies applied to cells. Thus, one major limitation is the strong photobleaching of the fluorescent sample in the focus of the illumination beam. In general, the application range of confocal microscopes is strongly restricted by the sample thickness. Depending on the diameter of the microscope's pinhole, the depth of focus is either short for small pinholes thus limiting the imaging depth. Larger pinholes allow to image deeper at planes below the focus, which however generates more fluorescent signals from planes below the focus and can consequently be seen as uniform glow on the images [59].

2.2.2 Two-photon microscopy

The strong limitation to thin fluorescent samples in confocal microscopy has been overcome in the early 1990ies by introducing nonlinear illumination techniques such as two-photon microscopy [60]. The main principle of two-photon microscopy is based on the generation of a fluorescent photon by absorbing two photons that exhibit the double wavelength instead of one single photon at the respective absorption maximum of the fluorescent sample. The absorption of the two-photon is usually driven by pulsed laser illumination within $\sim$ 0.5 fs and consequently requires high repetition rates for the illuminating lasers [61]. Due to the higher wavelengths, the excitation usually takes place in the near-infrared (NIR) region from typically 700 - 1000 nm, the fluorescent emission usually remains in the visible spectrum for samples labeled with typical fluorescent proteins such as GFP and mCherry. The NIR illumination has three major advantages: Scattering in the NIR region is much weaker (λ^{-4} dependence for Rayleigh scattering which is dominant in biological tissue, see equation 2.3) than in the visible range, thus allowing higher penetration depths. Second, photobleaching within the sample is weaker for incident photons at lower energy. Furthermore, in contrast to the continous-wave (CW) illumination in confocal microscopes, the short laser pulses in two-photon microscopes are spatially confined, so that absorption only takes place in

the focus [57], which allows to axially adjust the focal spot position. Consequently, by scanning in three dimensions, two-photon microscopy can achieve penetration depths that can exceed 1 mm [62]. As a drawback, the time consuming scanning in three dimensions limits the imaging field of view. Two-photon microscopy can also be extended to three-photon excitation with excitation wavelengths at typically 1600 - 1800 nm [63]. In addition, microscopic techniques based on second- and third-harmonic generation have been demonstrated. These modalities exploit the electron excitation to a virtual state and immediate relaxation. However, second- and third-harmonic generation imaging techniques require samples with structures at dimensions that are in resonance with the incident excitation frequency [61, 63].

2.2.3 Optical coherence tomography

Optical coherence tomography is another innovative imaging approach that has been able to overcome penetration depth limitations of conventional and confocal microscopy systems. In turbid media like biological tissue, OCT can achieve penetration depths up to 1 - 2 mm [64]. The technique relies on an interferometric imaging approach with low-coherent light where the backscattered signal from a biological sample and the reflected light from a mirror are brought into interference [28]. First imaging approaches where demonstrated in retinal imaging, however the method can also be used as microscopy tool in order to enhance the depth information of confocal microscopes [65]. In contrast to confocal or multiphoton microscopy approaches, the technique only relies on backscatter of light and not on absorption and subsequent fluorescent emission due to its intrinsic need for low-coherence between the sample and the reference arm. It can consequently not be used for imaging of labeled biological structures of interest. Nevertheless OCT remains a powerful tool for anatomical imaging [4].

2.2.4 Optical projection tomography

The previously mentioned 3D optical imaging techniques (confocal microscopy, two-photon-microscopy, OCT) all exhibit high resolution, the penetration depth in biological tissue however remains limited to a maximum of 1-2 mm [61, 64]. In contrast, optical projection tomography (OPT) has demonstrated imaging depths of up to 15 mm while maintaining the resolution at 5 - 10 μm [66]. The method is based on detecting transmitted light through a chemically cleared sample that is embedded in agar and rotated over 360°. The recorded projections are then

combined to a 3D image volume with mathematical algorithms. The mathematical algorithms vary. The first OPT system introduced by Sharpe in 2002 was based on a basic back-projection similar to that in X-ray CT. However more advanced forms of back-projection algorithms have been introduced since then [67]. OPT scans can be performed in two different ways, either by illuminating the sample and measuring the absorption or by measuring the transmitted light/the emitted fluorescence from the sample [68]. The latter is also referred to as fluorescence molecular tomography and will be discussed in the next subsection. The main limitation of OPT is the requirement for chemical clearing of the sample in order to reduce scattering and to render the sample partially transparent. Thus, its application range is restricted to *ex vivo* measurements for thicker samples. Thin, transparent samples like young zebrafish larvae < 7 dpf can however be imaged *in vivo*.

2.2.5 Fluorescence molecular tomography

Fluorescence molecular tomography is based on the same principles like fluorescence OPT with the difference of using point-sources for illumination and different reconstruction models [4, 69]. The illumination through a point source leads to higher resolution in turbid media [70]. The method has been improved by implementing mathematical forward models including scattering as a parameter and been referred as mesoscopic fluorescence tomography [71]. Consequently, *in vivo* imaging is possible at penetration depths not accessible to OPT.

2.2.6 Single plane illumination microscopy

Single plane illumination microscopy (SPIM) which is also referred to as selective plane illumination microscopy is another optically sectioning fluorescent microscopy technique that enables fast, volumetric 3D imaging at high resolutions [72]. The basic concept of the technique relies on optical sectioning of the sample from two sides by a light sheet in the focal plane of the objective. The light sheet is created by focusing the beam on an aperture with a cylindrical lens. The sample is consequently linearly translated through the light sheet, the generated fluorescence signals are detected orthogonally to the illumination with a camera (see figure 2.7). The major advantage of SPIM is the fast scanning in only one dimension, which strongly reduces the photobleaching of fluorophores in the sample compared to confocal or two-photon microscopy [73].

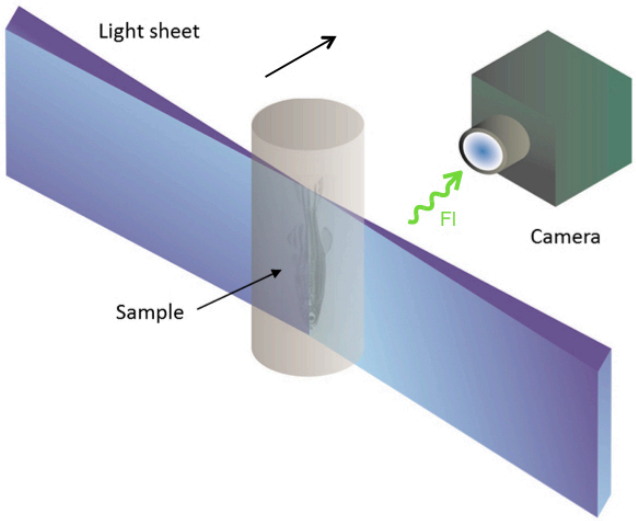

Figure 2.7: Scheme of a typical single plane illumination microscope. The sample is embedded in an agar cylinder, which is translated through the light sheets towards the camera using motor stages. The top arrow indicates the scanning direction. The camera consequently detects the generated fluorescence signals at each scanning position, so that a volumetric image stack is acquired after the scan.

SPIM setups are usually able to perform the linear translation scans at multiple angular rotations. The acquired dataset at multiple rotation angles can subsequently be reconstructed into a multi-view dataset to compensate for the worse axial resolution in the scanning direction and to improve the imaging depth [74, 75]. The image fusion is usually based on the use of fluorescent beads (typical diameter of 10 μm). More details on SPIM and relevant implementations and hybrid approaches will be discussed later.

2.3 Optoacoustic imaging principles

As discussed previously, optoacoustic imaging has the ability to "go deeper"than purely optical microscopy [4]. The method relies on the absorption of light and subsequent non-radiative relaxation. The optoacoustic (photoacoustic) effect is generally defined as the generation of ultrasound waves by a thermal expansion mechanism based on the absorption of electromagnetic radiation [76–78]. In other words, when energy is deposited on an absorber, fast thermal expansion and contraction of the absorber generates an acoustic pressure wave.

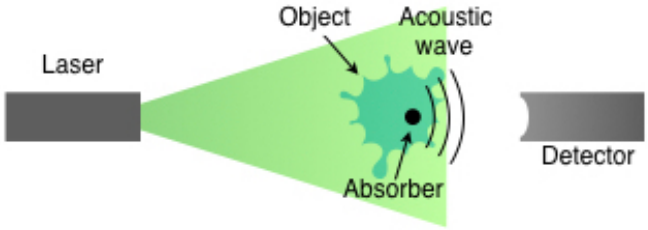

Figure 2.8: The optoacoustic effect: when short light pulses are absorbed, the energy is converted into heat and acoustic pressure waves are generated.

2.3.1 Optoacoustic signal generation

The optoacoustic effect can mathematically be explained by a wave equation that can be derived from the generalized Hooke's law (eq. 2.7) and the equation of motion (eq. 2.8) [5]:

$$\nabla \cdot \mathbf{z}(\mathbf{r},t) = -\kappa p(\mathbf{r},t) + \beta T(\mathbf{r},t) \tag{2.7}$$

$$\rho \frac{\partial^2 \mathbf{z}(\mathbf{r},t)}{\partial t^2} = -\nabla p(\mathbf{r},t) \tag{2.8}$$

where the vector $\mathbf{z}$ corresponds to the spatial displacement and p to the generated pressure at a location $\mathbf{r}$ and time t. T denotes the temperature, ρ the medium density, β the thermal coefficient of volume expansion and κ the isothermal compressibility which is defined as:

$$\kappa = \frac{C_p}{\rho v_s C_v} \tag{2.9}$$

where C_p and C_v correspond to the specific heat capacity at constant pressure and constant volume as well as v_s to the speed of sound, respectively.
By applying the divergence on 2.8, we obtain:

$$\rho \frac{\partial^2}{\partial t^2} \left(\nabla \mathbf{z}(\mathbf{r},t)\right) = -\nabla^2 p(\mathbf{r},t) \tag{2.10}$$

Hence, inserting the generalized Hooke's law 2.7 yields:

$$\left(\nabla^2 - \frac{\partial^2}{\partial^2 t}\right) p = -\frac{\beta}{\kappa v_s} \frac{\partial^2}{\partial t^2} T(\mathbf{r},t) \tag{2.11}$$

Now, the temperature can be substituted by the thermal heat function, which describes the thermal energy per time and volume deposited by the illumination.

$$\rho C_v \frac{\partial^2}{\partial^2 t} T - \alpha_{th} \nabla^2 T = H(\mathbf{r},t) \tag{2.12}$$

where α_{th} corresponds to the thermal diffusivity [5]. In thermal confinement, the heat conduction $\nabla^2 T$ can be neglected. This requirement is fulfilled, when the illumination time is much smaller than the thermal relaxation time τ_{th} which can be expressed mathematically by:

$$\tau_{th} = \frac{d_c^2}{\alpha_{th}} \tag{2.13}$$

This means that the time for the heat propagation in the sample needs to be much higher than the actual illumination time. Furthermore, the condition of stress confinement needs to be taken into account. Stress propagation can be neglected when the illumination time is much smaller than the ratio τ_r between the diameter of the absorber d_c and the speed of sound v_s.

$$\tau_r = \frac{d_c}{v_s} \tag{2.14}$$

Consequently, the wave equation for the photoacoustic effect can be written as [77]:

$$\left(\nabla^2 - \frac{\partial^2}{\partial^2 t}\right) p = -\Gamma \frac{\partial}{\partial t} H(\mathbf{r},t) \tag{2.15}$$

with the dimensionless Grüneisen parameter which is defined as:

$$\Gamma = \frac{\beta}{\kappa \rho C_v} = \frac{\beta v_s^2}{C_p} \tag{2.16}$$

Analogously to point-source problems in electrodynamic, the photoacoustic wave equation can be solved with a Green's function ansatz for an infinite medium:

$$G(\mathbf{r},t;\mathbf{r}',t') = \frac{\delta(\mathbf{r}-\mathbf{r}',t-t')}{4\pi|\mathbf{r}-\mathbf{r}'|} \tag{2.17}$$

Which can be interpreted as a point source emitting a spherical wave. By inserting the Green's function, one obtains:

$$p(\mathbf{r},t) = \frac{\beta}{\kappa v_s}\int_0^{t'} dt' \int_V G(\mathbf{r},t;\mathbf{r}',t')\frac{\partial^2 T(\mathbf{r}',t')}{\partial t'^2}d\mathbf{r}' = \tag{2.18}$$

$$= \frac{\beta}{4\pi\kappa v_s}\int_0^{t'} dt' \int_V \frac{\delta(\mathbf{r}-\mathbf{r}',t-t')}{|\mathbf{r}-\mathbf{r}'|}\frac{\partial^2 T(\mathbf{r}',t')}{\partial t'^2}d\mathbf{r}' \tag{2.19}$$

and consequently for $t' = t - \frac{|\mathbf{r}-\mathbf{r}'|}{v_s}$

$$p(\mathbf{r},t) = \frac{\beta}{4\pi\kappa v_s}\int_V \frac{1}{|\mathbf{r}-\mathbf{r}'|}\frac{\partial^2 T(\mathbf{r}',t-\frac{|\mathbf{r}-\mathbf{r}'|}{v_s})}{\partial t'^2}d\mathbf{r}' \tag{2.20}$$

This is the forward solution of the photoacoustic wave equation, which describes the pressure propagation as a function of temperature change. Hence, light /energy deposition must change as a function of time, which can be technically achieved by either short laser pulses or fast modulated light sources. The stronger the heating flux per unit time, the stronger the pressure wave. Since the pressure wave is proportional to the temperature change, OA 'signatures' of the heat function can be measured [79]. This can be emphasized by replacing the temperature change with the thermal heat function (eq. 2.12):

$$p(\mathbf{r},t) = \frac{\beta}{4\pi C_p}\int_V \frac{1}{|\mathbf{r}-\mathbf{r}'|}\frac{\partial H(\mathbf{r}',t-\frac{|\mathbf{r}-\mathbf{r}'|}{v_s})}{\partial t'}d\mathbf{r}' \tag{2.21}$$

Likewise, the volumetric expansion of the absorber volume V during optical excitation can be expressed by [5]:

$$\frac{dV}{V} = -\kappa p + \beta T \tag{2.22}$$

In thermal and stress confinement, the volumetric expansion $dV/V \approx 0$. With the

temperature T expressed as a function of the optical fluence Φ and η_{th} corresponding to the percentage of heat conversion,

$$T = \frac{\mu_a \Phi(\mathbf{r})}{\rho C_v} \tag{2.23}$$

the initial pressure p_0 can be rewritten as

$$p_0 = \frac{\beta T}{\kappa} = \frac{\mu_a \eta \Phi}{\kappa \rho C_v} \tag{2.24}$$

Hence, the initially generated pressure p_0 can thus be written with the Grüneisen parameter Γ (2.16) yielding [5]:

$$p_0 = \mu_a \Gamma \eta_{th} \Phi \tag{2.25}$$

Using the relation between the heat function H and the optical fluence Φ,

$$H = \mu_a \eta_{th} \Phi \tag{2.26}$$

finally yields the relation for the initial pressure as a function of the heat function:

$$p_0 = \Gamma H \tag{2.27}$$

Optoacoustic signal generation of a point-like absorber

As an example for a simplified case of the pressure generation by an absorber, the wave generation by a spherical point-like absorber is discussed here. Since the pressure generation is radially symmetric, only the radial propagation along the radius r needs to be taken into account. By applying equation 2.19 to a spherical absorber of radius R, one finally obtains [5]:

$$p(\mathbf{r},t) = \frac{r + v_s t}{2r} p_0(r + v_s t) + \frac{r - v_s t}{2r} p_0(-r + v_s t) + \frac{r - v_s t}{2r} p_0(r - v_s t) \tag{2.28}$$

Consequently, the pressure p(r) is split into three terms of interest, depending on the radial distance from the source r in respect to the pressure wave propagation $v_s t$ and the distance: a converging term towards the center (1), a diverging term

that is generated by the converging term (2), and a further converging spherical wave (3) [5]. Hence, equation 2.28 and its frequency content can be computationally simulated in Matlab.

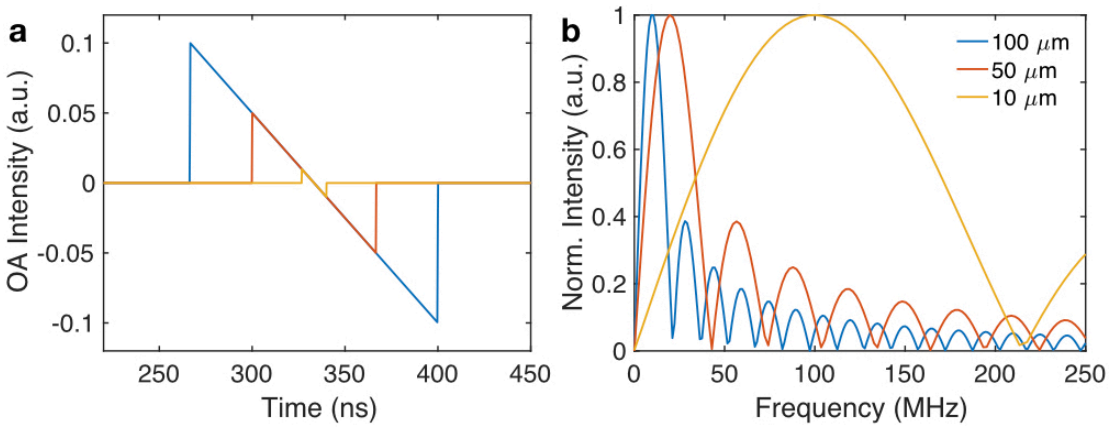

Figure 2.9: Simulated optoacoustic signals based on equation 2.28 generated by spherical absorber at various diameters measured at a distance of 500 μm from the center of the sphere. a) Time-domain signals, b) Frequency-domain signals. Adapted from [5].

Figure 2.9 a), shows the optoacoustic signals of three spherical absorbers with a diameter of 10, 50 and 100 μm respectively. As can be seen in the figure, smaller structures absorb less energy and consequently generate shorter and weaker optoacoustic signals scaling with the diameter of the sample. Furthermore, the main lobe of the frequency spectrum of spherical absorbers is symmetric around their central frequency (see figure 2.9 b). Again, the smaller the sphere, the shorter is the generated pulse, which increases the generated central frequency and the frequency bandwidth.

2.3.2 Sound propagation in tissue

One of the major advantages of optoacoustic imaging compared to purely optical techniques, is the weak scattering of ultrasound in comparison to light scattering in tissue, which is about three orders of magnitudes weaker [6]. Since biological tissue consists $\sim$ 80 % out of water, the speed of sound in tissue corresponds approximately to the speed of sound in water, which is $v_s \approx 1500$ m/s (in contrast to air, where $v_s \approx 330$ m/s). In general, the speed of sound in any material can be expressed by:

$$v_s = \sqrt{\frac{1}{\rho\kappa}} \tag{2.29}$$

where ρ corresponds to the density of the material and κ to its adiabatic compressibility [80]. By multiplying the speed of sound v_s with the material density ρ, the acoustic impedance is defined as

$$Z = v_s\rho \tag{2.30}$$

Consequently, when sound waves propagate from one medium to another, the wave can be either reflected, transmitted or refracted depending on ratio of the respective acoustic impedances Z_1 and Z_2. The corresponding reflection and transmission coefficients R and T are given by [34]:

$$R = \Big(\frac{Z_2 - Z_1}{Z_2 + Z_1}\Big)^2 \qquad T = \frac{4Z_2Z_2}{(Z_2 + Z_1)^2} \tag{2.31}$$

As can be deducted from the equations 2.31, a small difference in the acoustic impedance between two media leads to high transmission, whereas a high difference causes strong reflections. This has several consequences for imaging: ultrasound imaging relies on reflection of acoustic waves, thus a high difference between Z_2 and Z_1 such as at the interface between bone and tissue is a strong source of contrast. On the other hand, optoacoustic imaging is based on the small mismatches in acoustic impedance between different biological tissue layers so that the acoustic signals generated by optical absorption can be detected. For the same reason, optoacoustic imaging usually takes place with the samples immersed in a water bath, so that the strong acoustic mismatch between biological tissue and air can be circumvented. Analogue to refraction of electromagnetic waves, refraction between layers of different acoustic impedance is described by Snell's law, which is given by:

$$\frac{sin(\theta_1)}{sin(\theta_2)} = \frac{v_{s1}}{v_{s2}} = n \tag{2.32}$$

where θ_1 and θ_2 correspond to the angle of incidence and to the angle of refraction in regard to the perpendicular axis of reference. The refraction index n is typically $n \approx 1$ for biological tissue. Following equation 2.32 with $n \approx 1$, acoustic refraction in biological tissue can usually be neglected for optoacoustic imaging and forward

propagation of sound waves in tissue can be assumed [80].

Optoacoustic signal attenuation

Acoustic attenuation in biological tissue is usually based on the absorption on the cellular or molecular level, however at higher frequencies acoustic scattering cannot be neglected anymore [81]. This is typically due to thermal diffusion and friction losses. Mathematically, the optoacoustic pressure wave attenuation can be written as an exponential as [82].

$$p(r) = p(0)e^{\alpha(f)r} = p(0)e^{|\alpha_0|f^m r} \tag{2.33}$$

where $\alpha(f)$ corresponds to a frequency dependent attenuation coefficient and m to an exponent that is empirically determined for the medium. In biological tissue, the frequency-dependence is typically linear with $m \approx 1$ and can be written as [82]:

$$\alpha_0 = 0.5\ dBMHz^{-1}cm^{-1} \tag{2.34}$$

In contrast, for water the dependence is approximately quadratic ($m \approx 2$) with:

$$\alpha_0 = 0.00217\ dBMHz^{-2}cm^{-1} \tag{2.35}$$

This has important consequences for imaging applications. For example, OA signals at a frequency of 20 MHz propagating through 1 cm of biological tissue are attenuated by 10 dB. This frequency typically corresponds to the central frequency of the ultrasound detectors used in this thesis.

2.3.3 Ultrasound detection

In optaocoustic imaging, it is typically necessary to detect pressure signals in Pa or even mPa range [83], whereas ultrasound imaging signals typically lie in the kPa range [84]. Ultrasound detection can be based on all-optical detection principles or on the piezoelectric effect. Optical methods are either based on changes of the intensity of a probe beam (refractometric methods) or the deflection of a probe beam (deflection based methods) [84]. The physical detection principle of these detectors is typically based on interferometry such as a Fabry-Pérot interferometer [85, 86], Bragg gratings [87–89] and micro-ring-arrays [90, 91]. Since piezoelectric

detectors are the most common detectors in optoacoustic imaging and in this thesis, only piezoelectric transducers are used, this section only discusses piezoelectric methods. The piezoelectric effect relies on the generation of an electromagnetic field after changing the spatial dimensions of a piezoelectric material [92]. This applies to the inverse process, meaning that applying an electromagnetic field on an piezoelectric material can generate ultrasonic waves. Ultrasound imaging relies on the generation of ultrasonic waves with the piezoelectric element and subsequent detection of the backscattered waves with the same element. Naturally, the most common piezoelectric material is quartz [93], however materials used for sensing are typically poly-crystalline ferroelectric ceramic materials like lead zirconate titanate ($Pb(Zr,Ti)O_3$, also known as PZT), which exhibits much stronger piezoelectric characteristics than quartz [92]. As an alternative, piezo-composite materials such as polyvinylidence difluoride (PVDF) can be chosen for the active element. Figure 2.10a) illustrates a typical piezoelectric single-element detector and its main components.

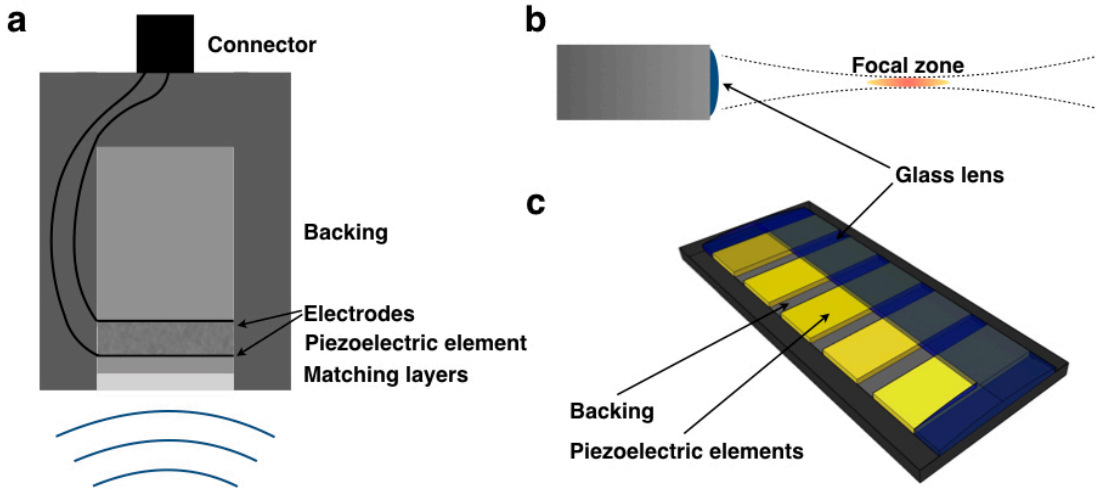

Figure 2.10: Working principle of piezoelectric transducers. a) Cross-sectional view of a flat single-element transducer. The main components include the matching layers, the piezoelectric element, the backing and the electrodes. b) Spherically focused single-element detector using a glass lens. c) Scheme of a linear-transducer array with a glass lens for cylindrical focusing. The distance between the center of two detector elements is referred to as pitch, the lateral width of an element as elevation. Adapted from [92, 94].

Typically, the thickness of the active element determines the central-frequency and the bandwidth of the detector. The bandwidth is defined as the frequency range from a low to a high cutoff frequency, where the detection sensitivity is -6 dB lower than the detection sensitivity at the central frequency. In order to achieve better

coupling efficiencies with the surrounding medium, the acoustic impedances of the detector and the surrounding medium should be as similar. Thus, several matching layers are put in front of the piezoelectric element to optimize the coupling efficiency to the surrounding medium, which is water or ultrasound gel [95]. Another problem of piezoelectric elements are reflections and back-reflections of the acoustic wave within in the active element, which causes oscillations and consequently leads to a poor axial detection resolution. Thus, a backing material is inserted into the rear part of the detector in order to dampen these oscillations. Typically, the backing material exhibits a similar acoustic impedance as the active element so that the oscillations are minimized. However, the strong dampening of the oscillations results in a loss of detection sensitivity [92].

Moreover, the shape of the detector surface can be mechanically curved in order to enable spherical, cylindrical or even conical focusing of the detector. The focal zone of the detector is defined as the area of the spatial sensitivity field in which the sensitivity is not less than - 6 dB of the maximum [96]. For focused detectors, PVDF has the advantage over ceramic detectors that it is less stiff and can thus be shaped more easily in the manufacturing process. As an alternative to mechanical deformations of the detector surface, acoustic (glass) lenses can be put on the detector surface for focusing (see figure 2.10b)). This is particularly important for high-frequency transducers where the active element needs to be thin and the crystal is consequently highly fragile. The same applies to high frequency transducer arrays with small elements, which are also used for this work [94] (see chapter 3). Figure 2.10c) depicts the scheme of a typical linear transducer array. Recently, capacitive micromachined ultrasonic transducers (cMUT) are emerging into the field of optoacoustic imaging [97, 98]. The method relies on capacitor cells in a silicon chip, thus a dense number of cells can be integrated in a cost effective way [99–101]. One of its key advantages is its broad angular detection. However, the technology is not as sensitive as PZT transducers yet and further development is needed.

2.3.4 Optoacoustic imaging methods

Based on the governing physical equations discussed previously, the optoacoustic effect can be exploited for biomedical imaging. Various optoacoustic imaging implementations have been designed in the past decade, which comprehend a broad application range. As for microscopic imaging modalities in general, the OA

imaging modalities can be classified by their resolution and penetration depth. For OA imaging systems, the scalability of resolution and penetration depth can be mathematically approximated by the rule of thumb [6]:

$$\frac{penetration\,depth}{resolution} \sim 200 \tag{2.36}$$

In terms of OA imaging approaches, OA modalities can be categorized into the microscopic and mesoscopic regime, which is separated at a penetration depth limit smaller and higher than 1 mm [4]. An alternative classification is provided which defines optoacoustic microscopy by a lateral resolution < 50 μm [102].

Optoacoustic microcopy

Optoacoustic microscopy systems can again be categorized by their resolution in either acoustic resolution (AR) or optical resolution (OR) systems [36]. Whereas in OR optoacoustic microscopy systems the lateral resolution is defined by the focal spot size of the focused incident beam, in AR systems the lateral resolution is given by the focal spot size of the focused detector. Since the optical focus only depends on the NA of the objective and the wavelength of the illumination beam, OR systems can focus tighter and thus achieve the higher spatial resolution. On the other hand, optical focusing is not needed for AR approaches. AR modalities can however achieve better penetrations depths, due to the weaker scattering of sound in tissue [103]. OR systems are usually applied to thin samples, thus they can be built with epitaxial or transmission illumination. In contrast, AR modalities are usually applied to thick samples where a high penetration depth is needed, thus AR systems are typically based on epitaxial illumination. Figure 2.11 demonstrates the scheme of both modalities. One promising implementation of AR systems is raster-scanning optoacoustic mesoscopy (RSOM) and its advanced implementation of multi-orientation raster-scanning optoacoustic mesoscopy (MORSOM). RSOM allows high penetration depths up to 5 mm at lateral resolutions of $\sim$ 20 μm [22, 104, 105]. Furthermore, the technique demonstrated whole-body imaging of juvenile zebrafish by means of optoacoustics.

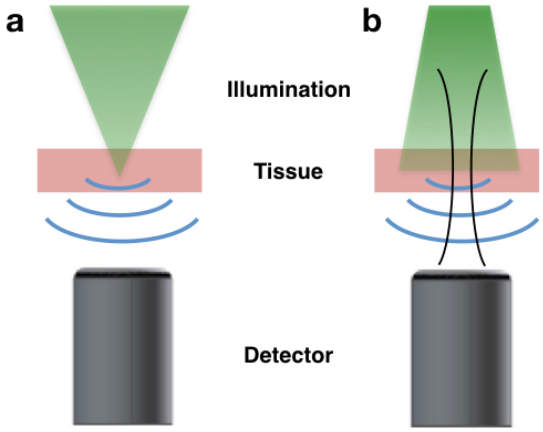

Figure 2.11: a) Principle of optical resolution (OR-OAM) optoacoustic microscopy. A focused beam defining the lateral system resolution illuminates biological tissue, the OA signals generated in a spatially confined region of interest (ROI) are detected with an arbitrary ultrasound transducer. b) Acoustic resolution (AR-OAM) optoacoustic microscopy: A divergent beam illuminates a broad ROI of biological tissue, a spherically-focused transducer detects the generated OA signal within its spatially confined sensitivity field.

Optoacoustic tomography

Optoacoustic tomography which is also referred to as photoacoustic computed tomography [6, 102], is based on broad illumination (which is typically generated by a fiber of a diffusor), acoustic detection at numerous positions and subsequent image reconstruction [36]. The implementation of the acoustic detection can vary from ring-arrays [106, 107], linear arrays [108–111], two-dimensional arrays [112], hemispherical arrays [113, 114], to spiral scanning with hemispherical arrays [115] or all optical-detection based on Fabry-Pérot interferometers [85]. The image reconstruction is based on acoustic inversion algorithms that can be classified in the four categories of time- and frequency- domain back-projection, time-reversal and model-based algorithms [116]. Details on image formation will be discussed in the next section. As in AR optoacoustic microscopy, the axial resolution for OA tomography is determined by the central frequency and the bandwidth of the detector, the lateral resolution by the focal spot size of the detector. By increasing the detector frequency range, OA tomography systems achieve resolutions at the price of penetration depth. On the higher penetration depth side of OA tomography systems, penetration depths of 7 cm can be achieved at spatial resolutions of ~ 720 μm [6]. One exciting feature of OA tomography systems that are e.g. based on ring-arrays is the ability of real-time imaging with multispectral illumination. This

allows instantaneous unmixing of specific endogenous and exogenous absorbers in real-time [117]. Figure 2.12 shows the scheme of typical OA tomography systems based on ring-arrays and linear arrays.

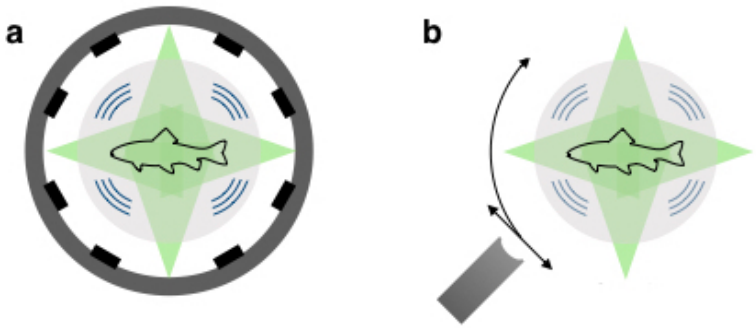

Figure 2.12: Principles of optoacoustic tomography. a) Scheme of a typical OA tomography system based on a ring-array. The sample is illuminated homogenously, OA signals are detected by numerous ring-array elements all around the sample. b) Scheme of a OA tomography system based on a linear transducer array. The array is translated and rotated over a wide angular range around the sample.

2.3.5 Image formation in optoacoustic tomography

When a certain number of optoacoustic signals (also referred to as projections or time transients) has been acquired in an optoacoustic tomography system, the signals need to be computationally reconstructed in order to obtain the underlying two or three dimensional image visualizing the absorption of light. This is fundamentally different from OR optoacoustic microscopy, where the OA peak-to-peak signal intensity is used for the 2D image formation. As mentioned before, several methods have been demonstrated to be suitable for reconstruction in optoacoustic tomography to solve the underlying inversion problem between pressure and absorption. These can be classified in optimization-based and analytical inversion algorithms. Time-reversal and model-based algorithms belong to the first and, time- and frequency-domain back-projection to the second category [116, 118].

The image formation based on solving the inversion problem goes back to the optoacoustic wave equation 2.21 that was derived before. The equation can be simplified since the energy deposition is much shorter than the time resolution of acoustic detectors [116]. Thus, the energy absorption can be approximated by

$H(\mathbf{r},t)\delta(t)$ and the OA wave equation can be rewritten as:

$$p(\mathbf{r},t) = \frac{\beta}{4\pi C_p}\frac{\partial}{\partial t}\int_V \frac{H(\mathbf{r}')}{|\mathbf{r}-\mathbf{r}'|}d\mathbf{r}' \tag{2.37}$$

Model-based algorithms

In brief, model-based algorithms solve the inverse problem by creating a discrete model matrix $\mathbf{M}$ that back-projects the deposited heat energy $\mathbf{H}$ to the measured pressure $\mathbf{p}$ [116, 119–121]. This can be formulated as:

$$\mathbf{p} = \mathbf{MH} \tag{2.38}$$

The model matrix $\mathbf{M}$ is only parametrized by the geometry of the transducer elements and the speed of sound, the inversion problem can thus be solved by a least-square minimization between the theoretical pressure generated by the model matrix and the discrete absorption grid $\mathbf{MH}$ and the measured pressure $\mathbf{p_m}$ [120, 121].

$$\mathbf{H_{sol}} = \arg\min \|\mathbf{p_M} - \mathbf{MH}\|^2 \tag{2.39}$$

For optimal results, a (Tikhonov) regularization term can be added which results in:

$$\mathbf{H_{sol}} = \arg\min \|\mathbf{p_M} - \mathbf{MH}\|^2 + \lambda^2 \|\mathbf{H}\|^2 \tag{2.40}$$

Model-based reconstructions allow to implement detector properties such as the electric and the spatial impulse response as well as detector surface considerations and usually show enhanced image quality compared to back-projection [122, 123]. However, due to the matrix multiplication, the method is computationally highly intensive in terms of RAM storage for three dimensional, high-resolution applications and thus typically applied in low resolution imaging modalities with a low number of projections (typically < 1000). Parallelization on graphics processing units (GPU) can accelerate the computation and symmetry considerations can significantly reduce the number of projections by a factor of ~ 400 [123]. However, due tothe high-resolution (~ 35 μm) and high number of projections (typically $> 10^6$) acquired in the hybrid system described in this thesis, only back-projection algorithms are

used.

Back-projection in optoacoustic tomography

Back-projection algorithms go back to CT, where X-ray radiation is detected and signals are consequently back-projected for the image formation using a Radon transform [124, 125]. This concept was transferred to optoacoustic imaging in the early 90ies [126]. An analytical solution for the inverse problem in optoacoustic tomography with a universal back-projection algorithm was proposed by Xu et al. [127]. The method relies on the time reversal of the detected ultrasound time ransients and subsequent summation and interpolation of the reversed signals on a defined grid plane or a grid volume for 2D or 3D applications respectively. For the simple case of a tomographic reconstruction of an OA point source in a 2D reconstruction grid, the predefined speed of sound v_s ($\sim$ 1500 m/s in water) and the knowledge of the time of flight t_{fl} (TOF) of the N-shaped OA signal of the point-like absorber allow to project the signal on a circle at a distance of $r = v_s \cdot t_{fl}$. With an increasing number of recorded transients, the back-projected arcs from detector positions all around the sample will intersect to form the image of the point absorber at its position in respect to the detector positions. Figure 2.13 illustrates the principle of 2D back-projection in OA tomography.

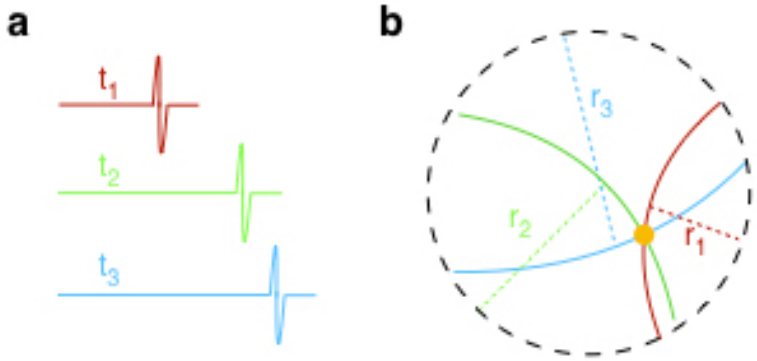

Figure 2.13: Principles of back-projection in OA tomography. a) Detected OA signal transients generated by a point absorber at three different detector positions that are shifted by $\sim 120°$. b) Reconstruction arcs at the respective detector positions and distances along with the radii $r_i = v_s t_i$. Adapted from [116].

As for any statistical problem, also in OA the SNR increases along $\propto \sqrt{N_{pro}}$, with N_{pro} being the number of projections acquired by the OA tomography modality [107]. In the case of the image reconstruction of a point absorber in OA tomography, the CNR increases likewise with $\sqrt{N_{pro}}$.

Mathematically, the universal back-projection formula describes the solution for the initial pressure p_0 to the optoacoustic wave equation 2.37 by time-reversal from the time of the detection t' [127]. As demonstrated in equation 2.27, for homogenous illumination, the initial pressure is directly linked to the heating function and thus to the absorption of the incident laser pulse. In the interest of conciseness, only the solution is presented here, the complete derivation can be found in [5, 127, 128]. The initial pressure calculated via back-projection can thus be written as:

$$p_0(\mathbf{r}) = \int_{\mathbf{\Omega_0}} b(\mathbf{r_0},t' = |\mathbf{r} - \mathbf{r_0}|)\frac{d\Omega_0}{\Omega_0} \tag{2.41}$$

with the back-projection function $b(\mathbf{r_0},\mathbf{t}')$ that is defined as:

$$b(\mathbf{r_0},t') = 2p(\mathbf{r_0},t') - 2t'\frac{\partial p(\mathbf{r_0},t')}{\partial t'} \tag{2.42}$$

and composed by the sum of the measured pressure p and the derivative of the measured pressure. Figure 2.14 illustrates the geometric realization of back-projection in OA tomography.

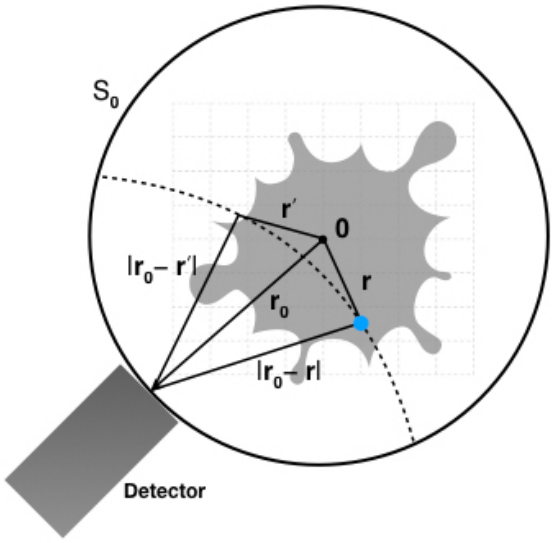

Figure 2.14: Back-projection of an absorber (blue dot) in optoacoustic tomography. The OA signal is generated at a distance $\mathbf{r}$ to the center of the tomographic setup, the transducer detects the OA signal at a distance $\mathbf{r_0}$. Subsequently, the time-reversed signal is spherically back-projected at a distance $|\mathbf{r} - \mathbf{r_0}| = v_s * t_{fl}$ from the detector where t_{fl} corresponds to the time of flight. Adapted from [127, 128].

The first term (i.e. the measured pressure) is referred to as "delay and sum"[129],

the derivative in the second term serves as ramp filter in order to suppress low frequency signals [5, 127]. Typically, relatively high frequencies dominate the frequency spectrum, thus the first term can be neglected and b can be approximated for a filtered back-projection:

$$b(\mathbf{r_0},t') \approx -2t' \frac{\partial p(\mathbf{r_0},t')}{\partial t'} \tag{2.43}$$

The back-projection formula 2.41 then projects $b(\mathbf{r_0},t')$ on a spherical surface, which is weighted by the contributions of the detector element surface to the reconstruction with $d\Omega_0/\Omega_0$ which can be expressed by:

$$d\Omega_0 = \frac{dS_0}{|\mathbf{r}-\mathbf{r_0}|^2} \cdot \left[\frac{\mathbf{n}_0^S \cdot (\mathbf{r}-\mathbf{r_0})}{|\mathbf{r}-\mathbf{r_0}|}\right] \tag{2.44}$$

where dS_0 corresponds to the infinitesimal detector surface element of the detector and $\mathbf{n}_0^S$ to its perpendicular unit vector. The back-projection formula is based on the assumption that the detector is a point detector. In OA tomography however, usually spherically or cylindrically focused detectors are used. Consequently, the detector surface S_0 is virtually put in the focus of the detector and the back-projection is based on virtual point detectors. Back-projection algorithms are usually executed on GPUs in order to accelerate computation.

Resolution in optoacoustic tomography

The spatial resolution and penetration depth are the key characteristics of any biomedical imaging system. As demonstrated previously, the width of an OA signal generated by any absorber and its respective frequency spectrum are determined by the absorber's size. Hence, the theoretically achievable resolution corresponds to the higher frequency spectrum emitted by the absorber, however limitations of the detection in terms of the detector's frequency bandwidth and sensing aperture usually do not allow to achieve the ultimately achievable resolution [130]. Further aspects limiting the resolution include the illuminating pulse length, the reconstruction method, acoustic inhomogeneities in the sample and the covered detection (angle). For this work, an illumination pulse length respecting the thermal and stress confinement is assumed and acoustic inhomogeneities are neglected due to the relatively small sample dimensions. A universal back-projection algorithm as introduced by Xu et al. [127] is applied and the detection angle of the system

described in this work is 360°. Hence, only the detector bandwidth and the detector geometry need to be taken into account.

For the work in this thesis, the ultrasound detection is based on a tomographic detection approach using a linear transducer array and spherically-focused single-element detectors. Thus, the in-plane resolution within the tomographic region of interest (ROI) is determined by the detector's acoustic bandwidth whereas the axial resolution is determined by the pitch of the array or the NA of the single-element detector respectively. The in-plane resolution can hence be mathematically expressed with [131]:

$$Res \approx 0.8\lambda_{max} \tag{2.45}$$

where λ_{max} corresponds to the maximum detectable wavelength by the detector. For example, at a speed of sound $v_s = 1480$ at room temperature and $\sim$ 30MHz maximum detectable frequency at the -6 dB sensitivity drop for the array and the single element detector, theoretical in plane resolutions of ~ 40 μm can be obtained in the hybrid system. However, frequencies beyond the 30 MHz at -6 dB sensitivity drop can still be detected at weaker sensitivity, thus slightly better resolutions can be achieved. Perpendicular to the in-plane resolution, the transversal resolution can be approximated by [102]:

$$Res_{trans} \approx \sqrt{a^2 + \left[(r/r_0)d\right]^2} \tag{2.46}$$

where a corresponds to the axial resolution, r_0 to radius of the tomographic system, r to the radius of the absorber (in respect to the tomographic center) and d to the diameter of the detector element.

2.3.6 Spectral unmixing of absorbers

As for many remote sensing systems, pixels underlying an image can be composed by several spectral components which are summed up to a final pixel intensity value. The decomposition of the constituent spectral features and their respective proportion in such a mixed pixel is referred to as spectral unmixing [132, 133]. The concept goes back to the 1920ies, when chemical components were investigated by reflectance spectroscopy and it has found a broad range of applications since

then. Nowadays, spectral unmixing algorithms can rely on strong computational power and can in general be categorized into linear and non-linear approaches, depending on the complexity of the problem. Three major steps are considered to solve a linear unmixing problem which include: Dimension reduction (optional), endmember determination (determination of the number of spectra constituents) and finally inversion (estimating the proportion of each spectrum in the mixed pixel) [132, 133]. For linear problems, this can be mathematically expressed by [132–134]:

$$\mathbf{I} = \mathbf{SF} + \mathbf{n} \tag{2.47}$$

with **I** describing the M x N pixel image matrix with M being the number of spectra and N the dimensions of the mixed pixels. **S** corresponds to the M x K spectral matrix, with K being the number of relevant absorbers in the dataset. **F** denotes the unknown K x N matrix for the fractions of each spectrum for each pixel respectively and **n** is a noise matrix.

In optoacoustic imaging, spectral unmixing algorithms have firstly been introduced to extract the spectral contribution to the mixed image pixels of fluorescent proteins with a weak PGE such as GFP and mCherry from strong endogenous absorbers such as hemoglobin and melanin in Drosophila melanogaster pupa and adult zebrafish [17]. Mathematically, the spectral inversion problem for the absorbed energy $H(\mathbf{x},\lambda)$ in the optacoustic reconstructions can be formulated as follows [135]:

$$H(\mathbf{x},\lambda) = \mu_a(\mathbf{x},\lambda)\Phi(\mathbf{x},\lambda,\mu_e) \tag{2.48}$$

where $\Phi(\mathbf{x},\lambda,\mu_e)$ corresponds to the light fluence in the absorbing medium and λ to the illumintating wavelength. The absorption coefficients $\mu_a(\mathbf{x},\lambda)$ can now be rewritten as the sum of their K spectral components with their respective molar absorption coefficients $a_k(\lambda)$ and concentrations $C_k(\mathbf{x})$:

$$\mu_a(\mathbf{x},\lambda) = \sum_{k=1}^{K} C_k(\mathbf{x}) a_k(\lambda) \tag{2.49}$$

Hence, inserting 2.49 into 2.48 yields:

$$H(\mathbf{x},\lambda) = \Phi(\mathbf{x},\lambda,\mu_e) \sum_{k=1}^{K} C_k(\mathbf{x}) a_k(\lambda) \tag{2.50}$$

This linear unmixing algorithm following equation 2.47 has been the first approach to multispectral unmixing of absorbers in optoacoustic imaging [17]. Since then, the unmixing methods in optocoustic imaging have tremendously evolved towards more advanced algorithms respecting specific imaging modalities and sample thickness. These methods include blind source unmixing, where no information about the constituent spectra is required before inversion [136]. This is especially interesting for thicker samples, when scattering and photon attenuation do not allow to assume quasi homogenous illumination in deeper tissue layers anymore [137]. Recently applied algorithms include the wavelength-dependent fluence attenuation in tissue, which particularly demonstrates potential for tissue oxygenation estimations in thick samples such as mice [138]. However, these approaches by Tzoumas et al. consider samples diameters of several centimeters in contrast to the several millimeter diameter samples such as zebrafish in the hybrid system. Thus, wavelength dependent fluence attenuation is neglected in this work and a linear approach as suggested by Razansky et al. [17] in 2009 for small sample diameters is chosen.

Consequently, the inversion problem can be solved using a least-squares minimization in order to minimize the error of the measured (reconstructed) $H(\mathbf{x},\lambda)$ and predicted energy absorption of a specific absorber with [135]:

$$\arg\min \varepsilon = \frac{1}{2} \left\| H(\mathbf{x},\lambda) - H(\mathbf{x},\lambda) \right\|^2 + P^2 \tag{2.51}$$

which finally results in a set of N linear equations for N illuminating wavelengths λ_N [17]:

$$H(\mathbf{x},\lambda) = \sum_{k=1}^{K} C_k(\mathbf{x}) a_k(\lambda) \tag{2.52}$$

2.4 Conclusion

In this chapter, the physical principles underlying optical and optoacoustic imaging were discussed, which can be summarized by photon absorption and scattering. Consequently, this chapter describes state-of-the-art optical microscopy modalities

such as confocal and two-photon microscopy as well as SPIM. Advantages and disadvantages of these modalities are discussed, highlighting that SPIM is well suited to be combined with other imaging modalities due to its high speed and thus low photobleaching. The following section describes the fundamentals of optoacoustic imaging, starting from the initial pressure generation of absorbers. Subsequently, this chapter discusses ultrasound propagation, attenuation and detection and gives an overview of OA imaging modalities such as OA microscopy and tomography. This highlights the unique potential of OA tomography due to its high-resolution, strong contrast and high penetration depth as a promising tool for studying long term development in model organisms, particularly when combined with SPIM.

3 Engineering hybrid optical microscopy and optoacoustic tomography

3.1 Introduction

As described in chapter 2, state-of-the-art optical microscopy methods include confocal microscopy, two-photon microscopy (including multiphoton microcopy) and SPIM. However, confocal microscopy and two-photon microscopy are based on scanning of a spherically focused beam spot and are thus relatively slow particularly for 3D imaging applications. In contrast, SPIM illuminates the sample with a light sheet, thus allowing to image volumetrically in 3D at much higher speeds. Consequently, light sheet illumination reduces the photobleaching of labeled fluorescent proteins in the sample due to the decreased scanning time and the reduced illuminating energy density compared to a focal scanning spot. SPIM is thus highly advantageous for imaging of early embryonic development in model organisms such as zebrafish [7, 15]. However, the penetration depth of purely optical methods is limited to a few hundred micrometers without chemical clearing of the sample, hence SPIM alone cannot be applied to deep imaging of morphogenesis in older and thicker samples. Optoacoustic tomography however successfully demonstrated the ability to go deeper than microscopy [4]. Combining SPIM and optoacoustic tomography into a hybrid system thus allows to track biological development of model organisms such as zebrafish at high resolution and over longer timescales from the embryonic stage to adulthood. This chapter gives an introduction into a novel hybrid SPIM and optoacoustic tomography imaging modality and describes the experimental apparatus that was designed and developed at the Institute for Biological and Medical Imaging in cooperation with Carl Zeiss AG. Parts of this chapter are based on a manuscript of a publication in preparation by Vetschera et al. [139].

Besides the direct high-resolution imaging of morphogenesis in deeper tissue layers,

the novel hybrid SPIM - OA tomography system can address various biological and medical applications particularly for zebrafish. Due to the strong reproduction of zebrafish, they are a well suited as a low-cost model organism that has caught broad interest in the scientific community in research areas such as cancer research, diabetes and tissue regeneration [11,12,140–142]. It has been recently demonstrated that zebrafish xenografts are a valuable model to investigate various types of cancer therapy, since the xenografts from patients develop faster in zebrafish than in other model organisms such as mice [143]. Furthermore, zebrafish are used to study tumor growth, angiogenesis and metastasis [9]. Zebrafish are a popular organism for drug testing, particularly in the emerging field of personalized medicine [14]. All these studies and biomedical research applications have so far been restricted to young and transparent zebrafish larvae, which are accessible to purely optical microscopy techniques. However, purely optical techniques cannot image deeper than a few hundred micrometers [4] and thus cannot be applied to older zebrafish which have grown thick and opaque. Hence, purely optical techniques do not allow any scientific knowledge gain about the long-term course of diseases and long-term effects of drugs and potential side effects. Moreover, morphogenesis can be affected until adulthood by disease and therapy respectively. The hybrid system combining SPIM and optoacoustic tomography now opens a new door to study all these interesting applications from the larval stage until adulthood.

Earlier experiments addressing hybrid SPIM and optoacoustic imaging were performed by Lin et al. [25]. The demonstrated system was based on linear translation of a sample embedded in an agar cylinder through a light sheet generated by a pulsed laser. Fluorescent and generated OA signals were simultaneously detected with a scientific complementary metal-oxide-semiconductor (sCMOS) camera and a linear transducer array respectively. Figure 3.1 illustrates the scheme and working principle of the system.

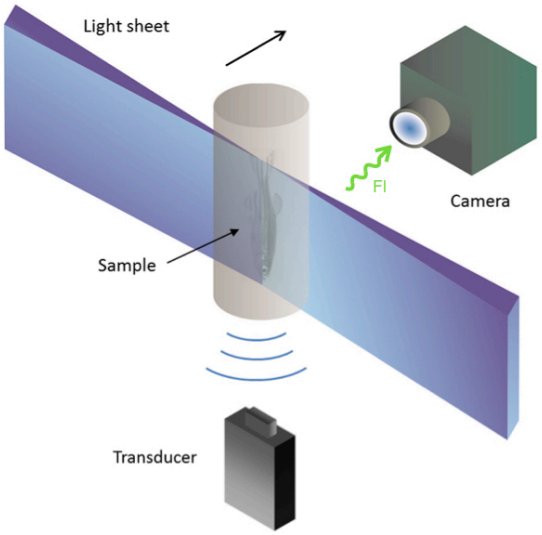

Figure 3.1: Detection principle of the first hybrid OA-SPIM system. The sample was linearly translated through a light sheet generated by a pulsed laser, while both fluorescence and OA signals were detected with a sCMOS camera and a linear transducer array, respectively. The top arrow indicates the scanning direction. Adapted from [25].

The method demonstrated the potential of hybrid fluorescence and optoacoustic imaging by showcasing the complementary fluorescent and absorption contrast of an adult zebrafish. However, this basic approach has several limitations: It only provides one-sided signal extraction for both fluorescence and optoacoustc signal, thus reducing the image quality and penetration depth. Furthermore, no intrinsic structures such as organs within the sample can be resolved and no optoacoustic contrast of the fluorescence labels is presented.

The limitations of the OA modality in the first hybrid system clearly show the need for a different OA implementation into the next-generation hybrid system. Optoacoustic tomography based on linear transducer array is a promising candidate to meet the requirements for the novel hybrid system. The method is also referred to as multispectral optoacoustic mesoscopy and has recently shown several advantages in high-resolution, volumetric OA imaging [110, 111, 144–146], particularly by demonstrating *in vivo* imaging of tumors in mice. The tomographic method presented by Gateau et al. [110, 111] is based on a linear transducer array that is rotated and linearly translated around the sample over almost 180° (see figure 2.12b). Using a 24 MHz cylindrically focused transducer array (Vermon, France), the technique enables an in-plane resolution of ~ 30 μm and ~ 110 μm resolution along 128 transducer elements. Hereby, the method allows to visualize volumetric

image stacks of 9 mm length in three dimensions [111]. Due to the thin sensitivity field of the cylindrically focused transducer array, the scanning geometry based detector rotation and translation yields significantly higher image quality compared to basic rotation of the detector [110, 145]. Due to its tomographic approach, the method can achieve better penetration depths than raster-scanning optoacoustic techniques such as RSOM. However, the system presented only covers an angular range of nearly 180° due to spatial limitations of the transducer rotation. Hence, an improved image quality can be expected for a larger angular detection span. Due to all these advantages, OA tomography based on linear transducer arrays was selected for the implementation into the hybrid system.

3.2 Experimental setup

The design of the experimental demonstrator was developed in close cooperation between researchers at the Institute of Biological and Medical Imaging and the corporate research and technology department of Carl Zeiss AG (Jena, Germany). The demonstrator is a versatile imaging platform that includes illumination beam paths for SPIM and OA tomography. Figure 3.2 shows computer-aided design (CAD) visualizations and photographs of the system.

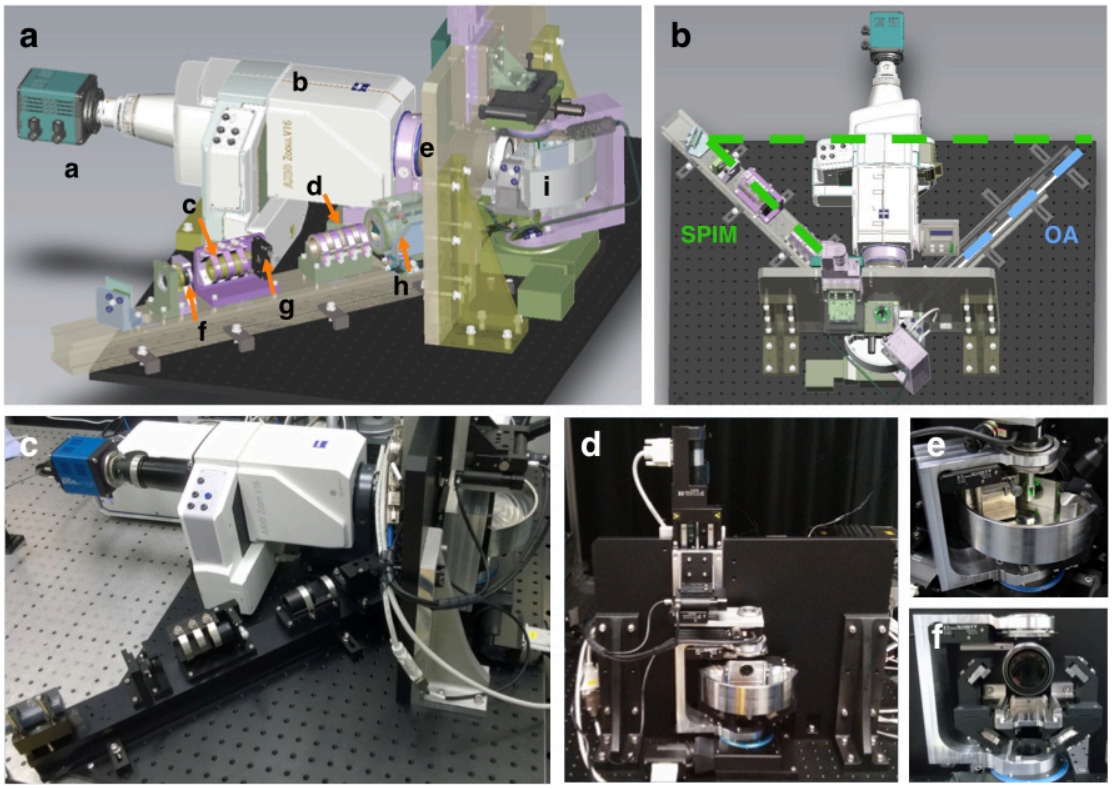

Figure 3.2: CAD visualization and photographs of the hybrid system. a) CAD side view of the hybrid system, depicting the SPIM illumination path: (a) sCMOS camera, (b) optical zoom, (c) cylindrical lens, (d) focusing lens, (e) camera objective, (f) adjustable pinhole for alignment, (g) adjustable aperture slit, (h) diaphragm prism and (i) sample chamber. b) CAD visualization top view of the hybrid system, the illumination paths for SPIM and OA tomography are marked in green and blue respectively. c) Side view photograph of the system, d) front view photograph of the system, e) photograph of the sample chamber in the system and f) illumination path into the sample chamber. The CAD visualizations are a courtesy of Carl Zeiss AG, Germany.

The modality includes a full optical element base for both a SPIM and an OA tomography system, enabling light sheet and a broad, homogenous illumination in the sample chamber for both modalities, respectively. Light sheet illumination for SPIM is created by cylindrically focusing the collimated beam on a slit aperture, the homogenous illumination is generated by spherically focusing the beam on a diffusor and subsequent coupling of the light pulses into a light-mixing rod (LMR). A flip mirror allows to easily switch between the illumination paths for SPIM and OA tomography, an electronic flip mirror (MFF101/M, Thorlabs, Germany) later replaced the mechanical mount to enable computer controlled flipping. Figure 3.3 shows a detailed illustration of the optical beampath for both modalities of the hybrid system.

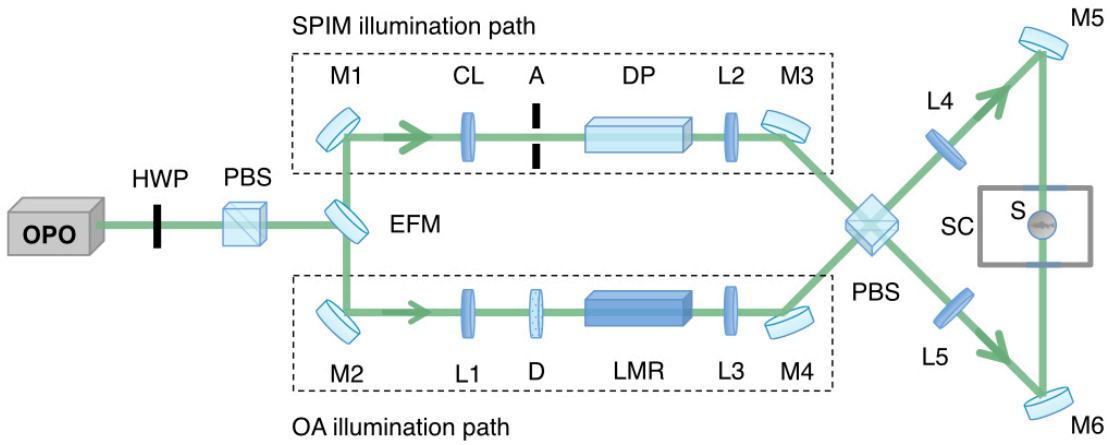

Figure 3.3: Illumination paths of the hybrid system. Nanosecond laser pulses emitted by an optical parametric oscillator (OPO) are firstly transmitted through a motorized half-wave plate (HWP), determining the polarization and consequently the pulse energy after transmission through the polarizing beam splitter (PBS). An electronic flip mirror subsequently determines the beam path for SPIM or OA tomography illumination. In SPIM mode, a cylindrical lens (CL) focuses the pulse on an adjustable slit aperture (A), the generated light sheet is consequently rotated by a dove prism (DP). In OA illumination mode, the laser pulse is spherically focused on a diffusor by a focusing lens (L) and then coupled into a light mixing rod (LMR) generating a squared, homogenous illumination profile. The exchangeable lens L3 allows to chose the length of the squared beam profile in the sample chamber (SC) to be 5, 7 or 10 mm^2 by working as a telescope in combination with the lenses L4 and L5. For both beam paths, the pulse is split by a second PBS to enable double-sided illumination on the sample (S). Adapted from [139]

Nanosecond laser pulses are generated by an optical parametric oscillator (OPO) laser (Spitlight-DPSS 250 ZHG- OPO, Innolas, Germany) that covers a broad wavelength range from 418 to 2300 nm. A half-wave plate (HWP) in a motorized rotation stage (KPRM1E/M, Thorlabs, Germany) and a polarizing beam splitter (PBS) allow to control the pulse energy by adjusting the polarization angle and subsequent polarization-sensitive deflection of the light pulses in the PBS. Afterwards, the electronic flip mirror determines the beam path of the pulse for either light sheet illumination for SPIM or a broad homogenous illumination for OA tomography. The illumination for SPIM is generated by focusing the light on an adjustable slit aperture (VA100/M, Thorlabs, Germany). The light sheet is subsequently rotated over 90° by a dove prism (DP) and then split into two by a polarizing beam splitter. The splitting allows two sided illumination in the sample chamber, where the separated beams are deflected to by two mirrors for both sides respectively. The light sheet illumination for SPIM is not sufficient for optoacoustic tomography, since optical sectioning with a light sheet only allows to

generate optoacoustic signals from the illuminated plane. The sample thus needs to be additionally scanned through the light sheet in order to obtain more depth information in OA tomography, which further increases the scan duration. Thus, broad homogenous illumination is used for OA tomography. To establish the broad, homogenous illumination for OA tomography, laser pulses are spherically focused on a diffusor and then coupled into a light mixing rod (LRM), which generates a squared illumination profile. The subsequent spherical lens L3 can be easily exchanged, thus squared homogenous beam profiles at lateral lengths of either 5, 7 or 10 mm can be obtained by choosing lenses of different focal lengths. As for the SPIM illumination, the beam is split into two fractions using the PBS and consequently deflected into the sample chamber by several mirrors. Figure 3.4 illustrates the sample chamber and the scanning geometries for both the SPIM and the OA tomography modality.

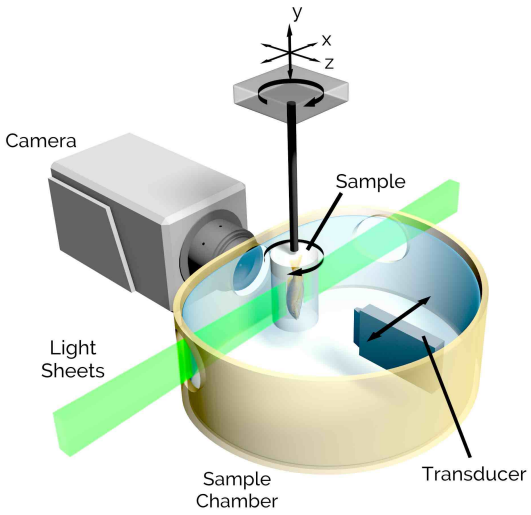

Figure 3.4: Sample chamber of the hybrid SPIM-OA system with the implemented linear transducer array. SPIM scanning is performed by linear translation of the sample through the light sheet towards the camera, which detects the generated fluorescence signals behind a suitable bandpass filter. In the OA tomography mode, squared, homogenous illumination from two sides at variable sizes from 5 - 10 mm is provided. Scanning of the sample is performed by rotating the sample over 360° and parallel vertical translation of the cylindrically focused linear array transducer at each angular position. Taken from [139].

The sample chamber is equipped with six individual motor stages: three of them allow linear translation of the sample in three dimensions and the fourth allows sample rotation over 360°. Furthermore, as indicated in figure 3.4, a translation stage allows linear translation of the ultrasound detector in x-direction. A second

rotation stage allows detector rotation over almost 90° in the sample chamber. All stages are manufactured by PI, Germany. Details on all stages are provided in the components section.

Scanning with the SPIM modality is performed by linear translation of the sample through the light sheet. This process can be repeated multiple times at various angular rotations of the sample. The emitted fluorescence signals are subsequently transmitted through a suitable bandpass filter that is mounted in the zoom system (Axio Zoom.V16, Zeiss, Germany) in front of the sCMOS camera (pco.edge 5.5, PCO, Germany). For scanning in optoacoustic tomography, the sample is rotated over 360° in discrete motion at an angular stepsize of $\sim 4°$, depending on the trade-off between image quality and speed. At each angular position, the array detector is completely translated along the whole sample width so that the cylindrically focused transducer is able to detect optoacoustic signals from the complete sample width at each angular position. The scanning process is illustrated in figure 3.5 a), whereas the alternating transducer translation at two consecutive angular rotation positions is depicted in panel 3.5 b). As an alternative scanning approach, the detector can be rotated over almost 90°. Likewise to the 360° sample rotation scanning mode, the transducer needs to be translated along the complete sample at each angular scanning position due to the thin, cylindrically focused sensitivity field. However, due to the limited angular view, the image quality on the opposite sample side of the detector is inferior compared to the 360°. A first characterization of the system was performed in close collaboration with Benno Koberstein-Schwarz and can be found in [147].

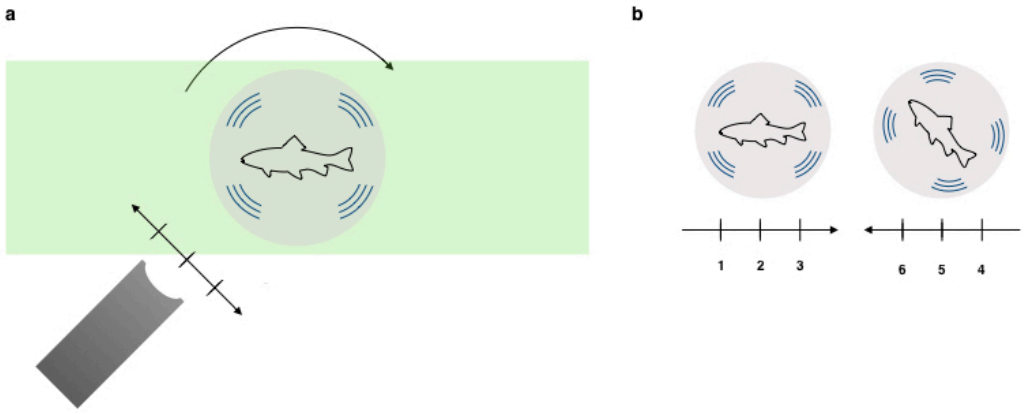

Figure 3.5: Scanning in OA tomography with the linear transducer array. a) Scheme of the scanning geometry, indicating the sample rotation over 360° and the discrete transducer translation at each angular position. b) Scanning pattern: At each predefined discrete angular position of the sample, the transducer is alternately translated in the positive and negative x-direction at discrete scanning steps. The sequence of the discrete scanning steps is marked by the respective number. The sample rotation stepsize is typically 4°, resulting in 90 angular positions during a 360° scan. The transducer stepsize is typically 100 μm, which corresponds to the spot size of the cylindrical focus of the array.

3.3 Principal components

Laser source

The multispectral illumination with sufficiently short laser pulses was provided by a Q-switched optical parametric oscillator. The OPO is driven by a Nd:YAG solid state laser that emits pulses at 1064 nm. These pulses are subsequently transmitted through a second-harmonic generator crystal (532 nm), and then guided through a third harmonic generator (355 nm) so that ultraviolet pulses at high energies are available for driving the OPO. Pulses at 355 nm are then transmitted through the nonlinear crystal, so that an signal pulse in the visible range and an idler pulse in the near-infrared region are generated. The generated wavelengths for both signal and idler depend on the incident angle of the third harmonic pulse in respect to the nonlinear crystal, the polarization of signal and idler pulses are perpendicular to each other. Thus, signal and idler can be separated at the output of the laser head with a polarizing beam splitter. The specifications of the laser are summarized in table 3.1.

Pulse length	7 ns
Pulse energy	18.5 mJ (at 488 nm)
Wavelength range	418 - 2300 nm
Spectral resolution	1 nm
Max. repetition rate	50 Hz

Table 3.1: Major specifications of the Innolas OPO laser.

Ultrasound detector

Ultrasound detection was performed by a cylindrically focused linear transducer array (Vermon, France) with 128 elements at a central frequency of 24 MHz. The scheme of such a linear transducer array has been shown in figure 2.10. Table 3.2 shows the main characteristics of the detector. With a central frequency of 24 MHz and a bandwidth of 58 %, the array can detect OA signals in the frequency range between around 17 and 31 MHz at an sensitivity drop at -6 dB.

Central frequency	**Bandwith**	**Focal length**	**Pitch**	**Elevation**
24 MHz	58 %	5.8 mm	70 μm	3 mm

Table 3.2: Specifications of the 24 MHz cylindrically focused linear transducer array from Vermon.

Data acquisition

A custom made data acquisition unit (Falkenstein, Germany) with 128 channels, a sampling rate of 125 MS/s and a resolution of 12 bit was used for data acquisition and analog to digital conversion. A built-in anti-aliasing filter cuts off the maximum detectable bandwidth to 45 MHz, which is lower than the 62.5 MHz expected by the Nyquist theorem. The unit provides a built-in amplification by a factor of 10 and a variable input impedance of 50 or 85 Ohm. Triggering is performed by the trigger signals at $\sim$ 10 V provided by the pockel cell of the OPO laser at maximum frame rate of 100 Hz.

sCMOS camera

A sCMOS camera (pco.edge 5.5, PCO, Germany) was used for fluorescence detection in the SPIM modality. The width and height of the camera is 2560 x 2160 pixels, whereas each pixel exhibits a resolution of 6.5 μm in both dimensions [148]. At the lowest magnification level (1.05) of the zoom microscope, i.e. at the largest possible field of view (FOV), this results in a resolution of 6.19 μm in both dimensions. The

low noise level of 1.1 e- med and the high dynamic range of 30 000:1 allow the detection of weak fluorescence signals. The camera was typically used at exposure time of 100-200 ms, which results in an averaged frame of 5 - 10 frames at the laser repetition rate of 50 Hz.

Motor stages

Translation of the sample and the transducer is performed by 6 motor stages from PI, Germany. Table 3.3 lists the respective stages for each direction.

Motor stage	**Type**	**Range**	**Min. stepsize**	**Max. speed**
Sample X	M-112.DG	25 mm	50 nm	1.5 mm/s
Sample Y	M-403.2DG	50 mm	200 nm	2.5 mm/s
Sample Z	M-112.DG	25 mm	50 nm	1.5 mm/s
Sample rotation	RS-40	360°	17.5 μrad	7°/s
Transducer X	M-111.DG	15 mm	50 nm	1.5 mm/s
Transducer rotation	M-061.PD	360°	17.5 μrad	90°/s

Table 3.3: Specifications of the motor translational and rotational stages used in the hybrid system. All stages are manufactured by PI, Germany.

3.4 Single plane illumination microscopy

Commercially available SPIM systems are typically based on CW illumination, however pulsed illumination is required for the OA tomography modality in the hybrid system. Thus, the illumination for the SPIM modality is equally based on the laser pulses generated by the OPO. Due to the high energy pulse energies, the pulse energy is usually reduced to 25 % by using the motorized HWP and the PBS in the system. The typical exposure time used for the sCMOS camera is 200 ms, thus 10 illumination pulses contribute to one SPIM frame at a laser repetition rate of 50 Hz. Usually, a stepsize of 10 μm is chosen for the translational motor stage in z-direction during one scan, which typically results in 400 acquired frames for a SPIM scan over 4 mm in depth.
Theoretically, the resolution in microscopy (except for super-resolution techniques) and thus also for SPIM, is only limited by Abbe's criterion with

$$d = \frac{\lambda}{2NA} \tag{3.1}$$

where λ corresponds to the illuminating wavelength and NA to the numerical

aperture of the objective lens. However, the focal spot size strongly depends on the quality of the beam profile which can be quantified by the M^2 factor [149].

$$M^2 = \frac{\pi}{4}\frac{\theta r_0}{\lambda} \tag{3.2}$$

with the focusing divergence angle θ, and the focal spot size r_0. For an ideal gaussian beam, M^2 equals 1. However, the light pulses provided by the OPO laser beam do not exhibit a perfectly gaussian beam profile due to its (anisotropic) divergence in height and width. Hence, the M^2 factor of the illumination in the hybrid system is larger than 1. Due to undersampling of the sCMOS camera at all magnification levels of the zoom system in front of the camera, the resolution for the SPIM modality in the hybrid is not limited by the technical components. Thus, the lateral resolution and consequently the FOV depend on the magnification level of the zoom system. For the lowest zoom magnification of 1.05, pixel resolutions of ~ 6.15 μm can be achieved for the largest FOV possible of $\sim 15.8 \times 13.3$ mm in x- and y-direction respectively. In contrast, at a maximum zoom magnification of 16.5, pixel resolutions of ~ 0.39 μm are possible at a FOV of 1×0.85 mm. The axial resolution along the scanning direction (z-direction) is determined by the diameter of the light sheet according to Abbe's criterion. On the the other hand, the depth resolution over lateral x-direction also depends on the depth of focus of the light sheet, which is also determined by the NA of the focusing lens. Mathematically, the depth resolution z_d can be expressed by [150]:

$$z_d = 2n\frac{\lambda}{(NA)^2} \tag{3.3}$$

with n corresponding to the refractive index of the surrounding medium. Thus, a trade-off between the focal diameter d_f and the depth resolution of the focus z_d for the focusing lens needs to be made. A high-NA objective lens generates a high axial resolution in the focus, however at the cost of a short depth of focus, which decreases the resolution over a large FOV. A low NA however results in a lower resolution in the focus but increases the focal depth and thus allows more homogenous resolution over the whole FOV [73]. For the hybrid system, an objective lens with a focal length of $f_c = 30$ mm was chosen for a more homogenous. The axial resolution was found to be around 16 μ by utilizing fluorescent beads (diameter of 200 - 300 nm) [147].

The sample rotation stage allows multiview acquisition at an arbitrary number of acquisition angles for the SPIM modality in the hybrid system. Multiview image stack fusion and deconvolution can be performed with the acquired datasets in imageJ using fluorescent beads surrounding the sample and fusion algorithms presented in [74, 75]. Fusion of several image stacks is based on the identification of the surrounding beads matching in different datasets after translation and rotation and subsequent minimization of the global displacement error. The deconvolution can be mathematically described by a Richardson-Lucy deconvolution, which is an Bayesian-based iterative expectation-maximization algorithm [75].
In the hybrid system, 50 μm fluorescent beads were put around the sample in the agar cylinder in order to take advantage of multiview fusion and deconvolution. The algorithms provided by [74, 75] can consequently fuse and deconvolve the 3D data stacks of zebrafish larvae scanned at four different angular orientations in the hybrid system at angular displacements of 90°. Figure 3.6 shows the maximum intensity projections (MIPs) of two consecutively acquired SPIM image stacks from the top (3.6 a) and side (3.6b) view. As an example for basic image stack fusion of four SPIM datasets scanned in the hybrid system, the top (3.6c) and side (3.6d) view of the fused 3D image stack are shown. For enhanced image quality, the deconvolution algorithm can be applied on the datasets. The results of the deconvolution, are shown from the top and side view in panels 3.6e) and panel 3.6f). The algorithm yields promising results for zebrafish larvae imaged in small volumetric data stacks. However, the algorithm fails for large data volumes acquired by scans of older and larger samples.

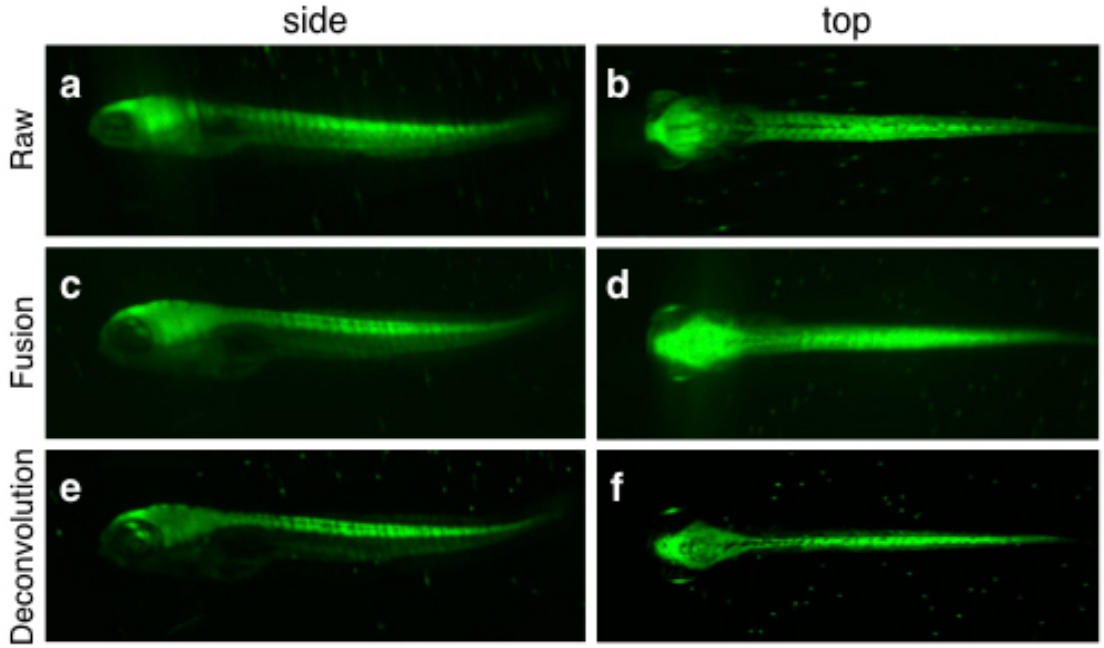

Figure 3.6: Fusion and deconvolution of multiview SPIM datasets. a) Side and b) top view MIP of zebrafish larvae acquired during two scans after 90° rotation. c,d) Side and top view MIP of the fused zebrafish image stack of four datasets shifted by 90° respectively. e,f) Side and top view MIP of the deconvolved zebrafish image stack of four datasets shifted by 90° respectively. The algorithm applied for fusion in imageJ is described in [74, 75].

3.5 Multispectral optoacoustic tomography

The hybrid system allows tracking of zebrafish development over several weeks. The key results on such a long-term study with the system can be found in our publication [139] and in [147]. This thesis thus focuses on further important capabilities of the system: one of the key advantages of optoacoustic imaging in general is its ability to visualize various absorbing tissue components deep in tissue. However, optoacoustic images are often dominated by strong endogenous absorbers like hemoglobin or melanin, which hinders the visualization of endogenous or exogenous sources of contrast that exhibit a weaker photoacoustic generation efficiency. Thus, applying multispectral illumination can be a useful technique to gain additional information about the sample. In a first basic approach, difference images can be created for the volumetric image stacks. This method allows to gain spectral information of absorbers and allows to visualize contrast of absorbers in mixed pixels that are otherwise completely overlapped by absorbers with a stronger PGE. As a more advanced approach, unmixing algorithms can be applied for more sophisticated

extraction of localized absorption in tissue. In the simplest case, it is assumed that each pixel of an optoacoustic image is a linear combination of multiple absorbing components and can thus be expressed as [134]:

$$\mathbf{I} = \mathbf{SF} + \mathbf{n} \tag{3.4}$$

with **I** describing the M x N image matrix with M being the number of wavelengths and N the image dimensions. **S** corresponds to the M x K spectral matrix, with K being the number of relevant absorbers in the dataset. **F** finally denotes the unknown K x N matrix for the fractions of each spectrum for each pixel respectively and **n** is an additional noise term.

Due to broad wavelength range covered by the OPO laser from 420 - 700 nm in the visible range and up to 2300 nm in the near-infrared region, the hybrid system can be a valuable platform for multispectral optoacoustic tomography used for imaging of different absorbers in biological tissue (see figure 2.4). For a scan in discrete motion based on the linear transducer array, multispectral data acquisition can be either provided by several consequent scans at different wavelengths or by changing the wavelength at every scanning position. Tuning of the wavelength however takes ~ 0.7 s, thus changing the wavelength at every scanning position does not fundamentally improve the scanning time. As an alternative, the sweep mode of the laser can be exploited, which allows repeated pulse-to-pulse wavelength switching along a preprogrammed pulse sequence. For an efficient use of the sweep mode, it is however required to know the first wavelength of each illumination cycle. This requirement is not met by scanning in discrete motion, thus illumination patterns based on wavelength tuning without preprogrammed sweep cycles were used.

Figure 3.7 shows first results for array-based multispectral optoacoustic tomography acquired with the hybrid system. Panels 3.7a) and 3.7b) show the side view and top view MIP of a 2-month-old wild-type zebrafish. The reconstructions acquired at 450 and 550 nm are represented in red and green respectively, thus yielding in a yellow contrast for structures absorbing at both wavelengths. Panels 3.7c-e) show the cross-sectional MIPs of the linearly unmixed ROIs highlighted in a). The linear unmixing algorithm considered reconstructions at 450, 488 and 550 nm as well as the spectra of oxygenized and de-oxygenized hemoglobin and melanin. Several anatomical structures deep in the fish are revealed, which include e.g. the gill

filaments (2), the spinal cord (6), the cardinal vein (7) and the swim bladder (8). Panel 3.7 f) shows a zoom of the panel e), highlighting the spinal cord and the cardinal vein, which were used for extracting the spectra in panel 3.7g).

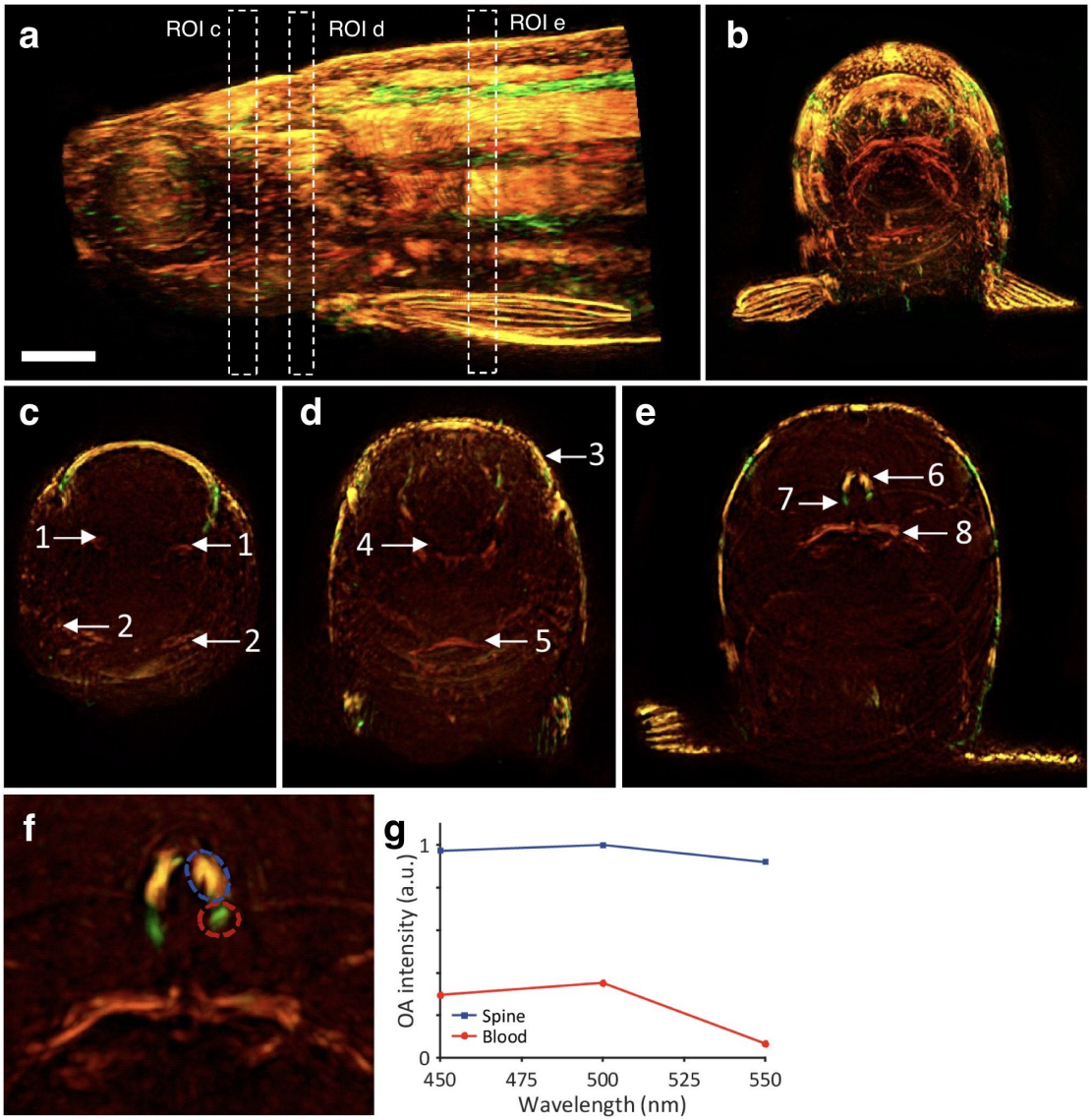

Figure 3.7: Multispectral OA tomography of a 2-month-old wild-type zebrafish. a-b) The zebrafish was measured imaged at 450 nm (green) and 550 nm (red), the superimposed reconstructions are thus represented in yellow. a) Side view MIP, b) top view MIP. (c-e) Linear unmixed ROIs marked in the MIP in panel a). Numbers annotate anatomical structures: 1, hyomandibula; 2, gill filaments; 3, semicircular canal; 4, medulla oblongata; 5, cardiac ventricle; 6, spinal cord; 7, cardinal vein; 8, swim bladder. f) Zoom of the ROI highlighted in panel e). g) Spectrum of the spine and vessel marked in panel f). The scale bar in panel a) indicates 1 mm.

3.6 Near-infrared multispectral optoacoustic tomography

As described in chapter 2, multispectral illumination in the near-infrared region offers exciting opportunities for optoacoustic tomography. First, scattering decreases with an increasing wavelength (mostly because of weaker Rayleigh scattering $\propto \frac{1}{\lambda^4}$), thus higher penetration depths can be achieved. Second, the absorption coefficients of lipids and water strongly increase as the illumination wavelength increases (see figure 2.4), thus allowing to image new features deep in biological tissue. However, several technical drawbacks need to be taken into account when extending the illumination range to the near-infrared. The pulse energies of the OPO drops from $\sim$ 18.5 mJ at the reference wavelength of 488 nm to $\sim$ 6 mJ at 750 nm. Furthermore, the optical components in the beam path for both the SPIM and the OA tomography modality are specified for the visible range, using these components in the near-infrared range results in strong losses in pulse energy. To overcome these losses, a custom-made multimode fiber bundle (CeramOptec, Germany) consisting of 430 fused fibers of 200 μm diameter was implemented to circumvent the losses in the OA tomography beampath. The fiber output consists of two channels with randomized 50:50 splitting of the single fibers so that the sample can still be illuminated from 2 sides. The fiber bundle has a NA of 0.22 at the input and at both outputs, respectively.

Imaging of absorption contrast of water and lipids deep is a highly attractive application for the hybrid system. However, pulse energy losses due to light absorption in the water bath surrounding the sample cannot be neglected anymore because of the increasing absorption coefficient of water in the near-infrared region (see figure 3.8). This limitation can be overcome by the use of heavy water (D_2O) in the sample chamber, an expensive but effective solution to reduce pulse energy losses. Figure 3.8 shows the absorption spectra of water and heavy water respectively. As demonstrated by the spectra, the absorption coefficient μ_a of heavy water is 1-2 orders of magnitude lower than the one of water at wavelengths exceeding around 700 nm, which allows to reduce the pulse energy losses in the surrounding water bath.

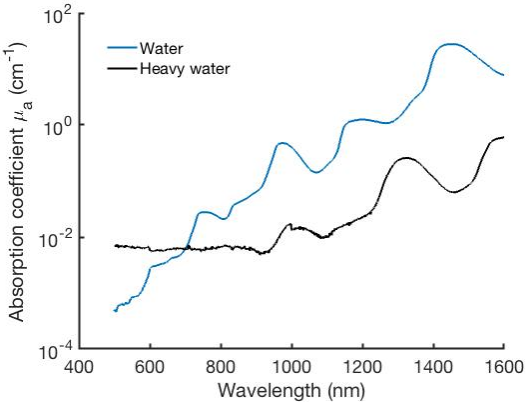

Figure 3.8: Absorption spectra of water (H_2O) and heavy water (D_2O). Data from [151].

Figure 3.9 illustrates the imaging results of multispectral OA tomography in both the visible and the NIR wavelength range after applying a linear unmixing algorithm. A 25-day-old transgenic zebrafish (Brn3c:GFP) was measured at 450, 488, 550, 600, 860 and 930 nm respectively, thus six image stacks were reconstructed via back-projection and subsequently linearly unmixed for blood, melanin and lipid. Panel 3.9a) shows the side view MIP of the unmixed volume of the zebrafish. Panel 3.9b) shows the cross-sectional MIP marked in panel 3.9a) in the region of the heart. Here, the melanin pigmentation, subcutaneous lipid and blood in the region of the heart can be observed. An enlarged MIP of the upper fin is illustrated in panel 3.9c), the inset shows a photograph acquired with the sCMOS camera of the system.

It can be observed that the black melanin pigmentation visible on the photograph corresponds to the melanin contrast of the OA MIP. This equally applies to the transparent boundary of the fin, which is only absorbing at NIR wavelengths and not in the visible range. Likewise, panel 3.9d) shows an enlarged MIP of the lower fin with a photograph of the fish as an inset. Again, the melanin pigmentation and the transparent boundaries of the fin are clearly visible in both the OA MIP and the photograph. The unmixed spectra for melanin, blood and lipid are illustrated in panel 3.9e).

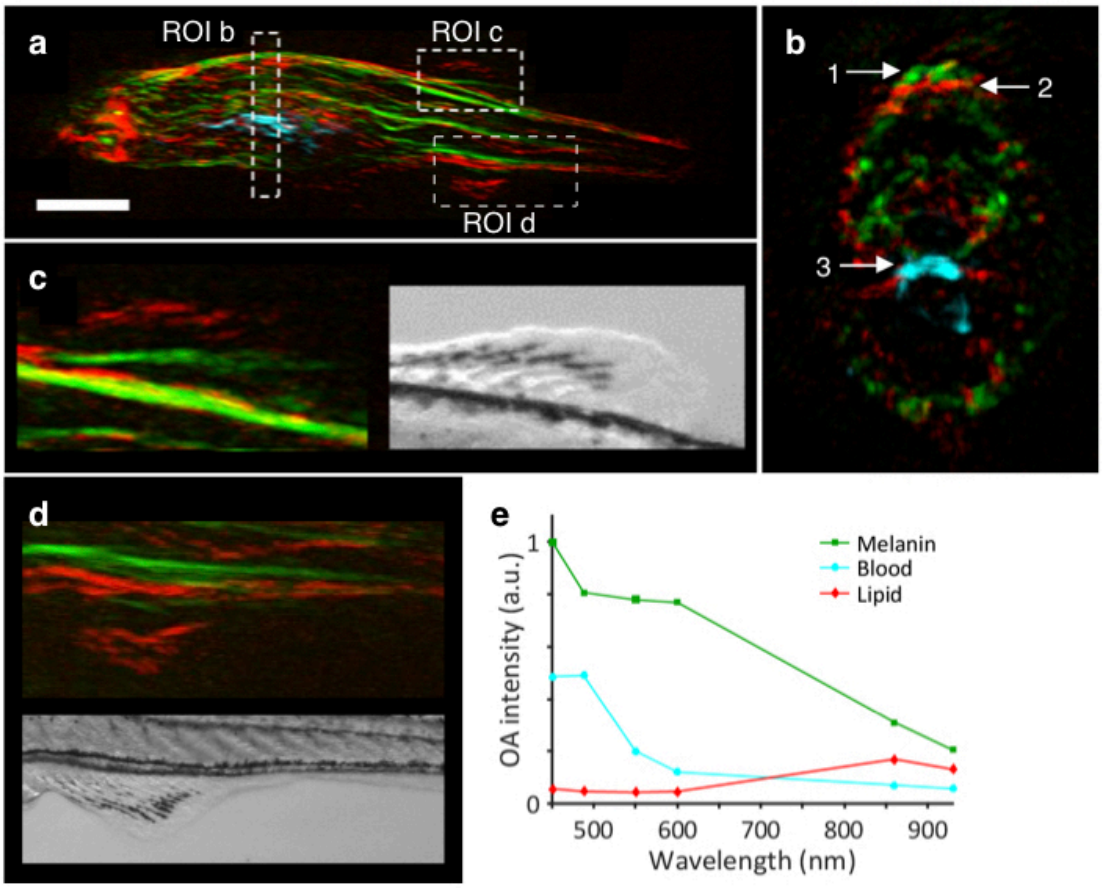

Figure 3.9: Multispectral OA tomography images of a 25-day-old transgenic zebrafish (Brn3c:GFP) in the visible and the near-infrared range. The transgenic zebrafish was measured at 450, 488, 550, 600, 860 and 930 nm and a linear unmixing algorithm was subsequently applied on the six reconstruction volumes. Melanin contrast is visualized in green, lipid/water contrast in red and blood in blue. a) Side view MIP of the unmixed volume. b) Cross-section marked in panel a), the arrows indicate the melanin pigmented skin (1), subcutaneous lipid (2) and blood in the region of the heart (3). c) Enlarged view of the upper fin from highlighted in panel a). The inset corresponds to a photograph of the same area acquired with the sCMOS camera. d) Enlarged view of the lower fin, the inset corresponds to a photograph of the same area. e) Spectra of melanin, blood and lipid which were extracted from the reconstruction volumes. The scale bar in corresponds to 1 mm.

Furthermore, the results presented in figure 3.9 can be used to approximate the content of the relevant absorbers melanin and water/lipid inside the reconstruction volumes of the fish (see figure 3.10). Panels 3.10a) and b) show the side view and cross-sectional MIP of the unmixed melanin and lipid of the 25-day-old zebrafish introduced in figure 3.9 and indicate the ROI volume used for the quantification. A total volume of 40 x 35 x 55 pixels is selected, which corresponds to a total volume of 0.32 μm^3 at a pixel resolution of 12 x 50 x 12 μm in the x-, y- and z-direction

of the system respectively. The number of pixels above a specified threshold for the melanin and lipid 3D volume can consequently be used to quantify the pixel content of melanin and lipid when divided by the total number of pixels in the volume. Panel 3.10c) shows the results for the quantification in the optoacoustic reconstruction, yielding in $\sim$ 5 % and $\sim$ 25 % of relative content for melanin and lipid respectively. The black dots indicate the results for different thresholds on the logarithmic scale. Panel 3.10d) shows the content for both melanin and lipid as a function of the logarithmic threshold. However, the results need to be interpreted with care for several reasons: first, the relative pixel content strongly depends on the intensity threshold. Second, due to stronger scattering at lower wavelengths, the acquired OA reconstructions at lower wavelengths are supposed to exhibit less absorption and thus less image pixel intensity in deeper tissue layers. No optical fluence correction is taken into account for the reconstruction, which could theoretically compensate for the weaker pixel intensities due to scattering. Furthermore, the laser pulse energy is decreasing for higher wavelengths, thus distorting the linear unmixing process. The OA reconstructions are normalized to the average pulse energy at the respective wavelength, however this is only an approximation to the problem. Furthermore, no information on pulse-to-pulse energy deviation is taken into account.

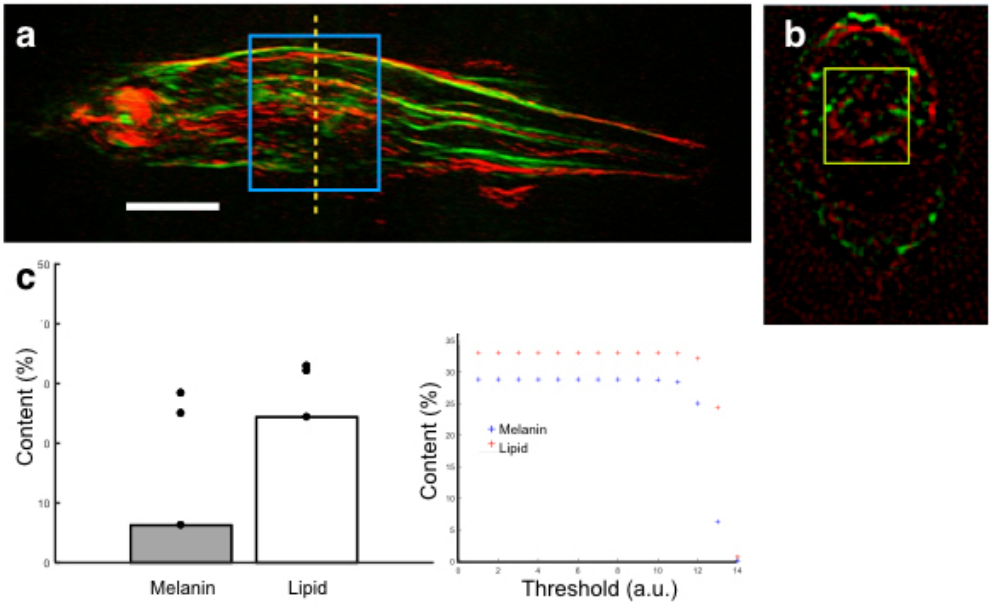

Figure 3.10: Quantification of absorbers with multispectral OA tomography reconstructions of a 25-day-old zebrafish. The transgenic zebrafish (Brn3c:GFP) introduced in figure 3.9 was measured at 450, 488, 550, 600, 860 and 930 nm and subsequently linearly unmixed afterwards for melanin and lipid. a) Side view MIP and b) cross-sectional MIP of the linearly unmixed volume. The highlighted ROIs indicate the volume of interest taken into account for the quantification. c) Relative pixel content of melanin and lipid in the volume. d) Dependence of the pixel content on the threshold. The scale bar in panel a) indicates 1 mm.

3.7 Further system implementations and applications

Optical projection tomography

Based on the existing high-resolution sCMOS camera and the translation and rotational motor stages for the sample, the hybrid SPIM - OA tomography system can also be used for optical projection tomography. A white-light or a broadband NIR LED can be put in a 3D printed holder at the opposite of the camera, thus enabling trans-illumination of the sample. As an alternative, a LED-ring array can be assembled on top of the sample allowing homogenous sample illumination. By rotating the sample over 360° at a stepsize of one degree, optical projections at each angular rotation can be acquired. In combination with a linear translation scan along the z-axis at a stepsize of 50 μm, the single projection views can be back-projected to a 3D volume with a Matlab reconstruction algorithm provided by Carl Zeiss AG. Even though the penetration depth of the acquired OPT projections is limited to $\sim$ 1 mm due to photon scattering, OPT is an additional source of contrast primarily for transparent (in the visible range) superficial structures and extends the multimodal capabilities of the hybrid system. Figure 3.11 demonstrates a hybrid MIP combining the reconstruction of OA tomography at 488 nm (green) with the respective OPT reconstruction (magenta). Panel 3.11 b) and 3.11 c) show cross-sectional MIPs with an additional OA tomography reconstruction at 930 nm (red). As can be seen, OPT does not allow to resolve intrinsic structures deep in the fish in contrast to the OA modality. Panel 3.11 d) illustrates the scheme of an OPT scan.

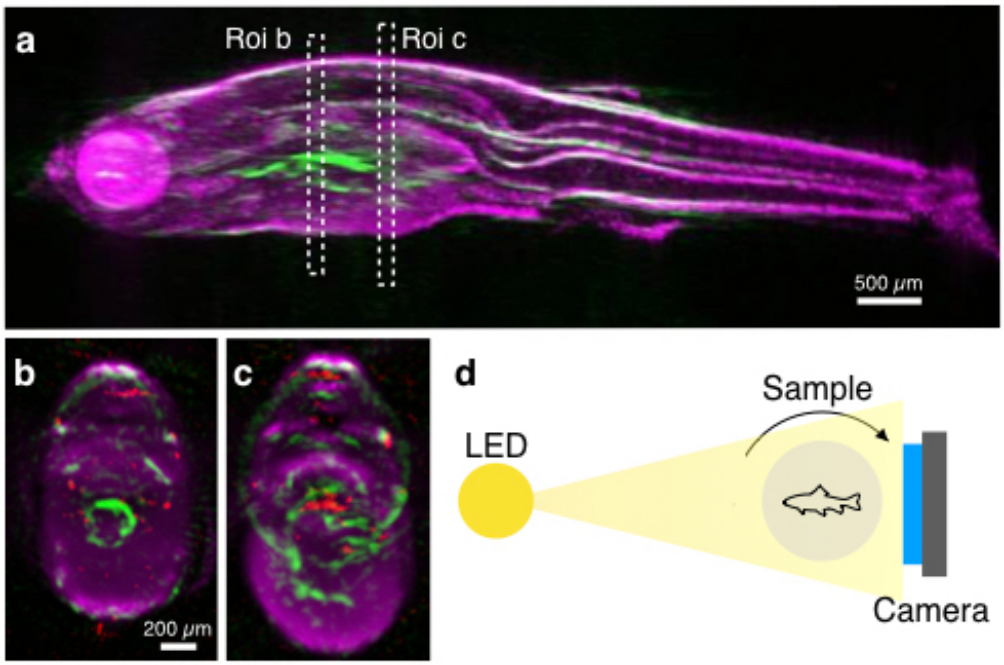

Figure 3.11: Hybrid OPT and multispectral OA tomography of a transgenic zebrafish (Brn3c:GFP) at 25 days. a) Side view MIP of a hybrid image combining OPT (magenta) and OA tomography after illumination at 488 nm (green). b-c) Cross-sectional slides of the respective ROIs marked in a). An additional OA illumination wavelength at 930 nm (red) is added to the image. d) Scheme of the OPT implementation in the sample chamber.

Further applications

Apart from imaging of model organisms such as zebrafish, the system can also be used for imaging of whole excised organs. This works particularly well when the reporter gene LacZ is used, which is a particularly strong absorber and allows to label the structures of interest in the blue regime. Thus, the labeled structures strongly absorb at wavelengths greater than 550 nm and can provide a strong source of contrast for OA tomography. As an example, excised mice organs such as the lung and the pancreas have been imaged. Figure 3.12 a) depicts a mouse lung labeled with the reporter LacZ, whereas Panel 3.12b) shows a hybrid OPT and OA tomography image of labeled mouse pancreas. Here, OPT is a suitable modality for visualizing the surface of the of the pancreas (grey), whereas OA tomography reveals the labeled beta cells (blue) even in deeper tissue layers. This may lead to interesting applications, since the volume of the beta cells is known to be a marker of diabetes [152]. With the strong contrast and high resolution provided by OA tomography, the absolute volume for the cells and the volume of individual cells

can be calculated. As described previously, the image intensity threshold strongly affects the estimation. Panel 3.12c) illustrates the absolute volume of beta cells in the measured volume as a function of the OA intensity threshold. The estimate is based on a voxel resolution of $12 \times 12 \times 35$ μm. For a reasonable intensity threshold of $4 \cdot 10^{12}$ (a.u.), an absolute volume of 0.15 mm^3 can be estimated.

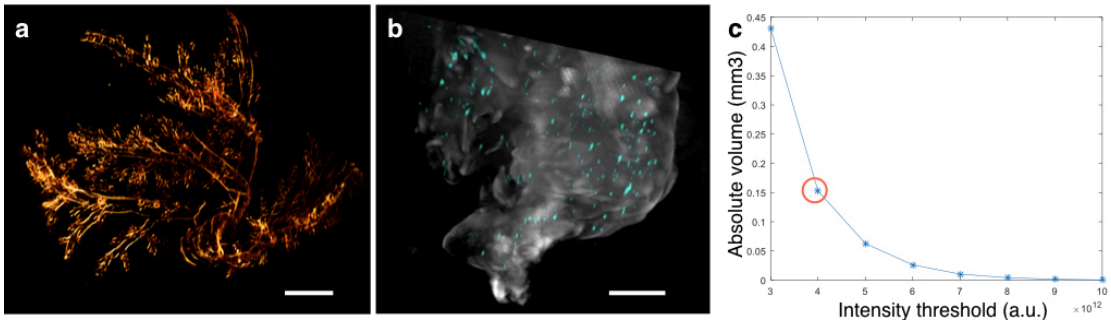

Figure 3.12: Imaging of excised mice organs labeled with blue product LacZ. a) A mouse lung measured at 650 nm after chemical clearing. b) Hybrid OPT (grey) and optoacoustic image (blue) of a mouse pancreas, revealing the labeled beta cells deep in the pancreas. c) Quantification of the absolute volume of beta cells deep in the organ as a function of the OA intensity threshold applied. The scale bars in a) and b) indicate 1 mm.

3.8 Conclusion

In this chapter, the hybrid MSOT - SPIM system was introduced. This hybrid microscopy platform allows imaging of development of organisms such as zebrafish over longer timescales that are not accessible to purely optical methods. Both light sheet illumination for SPIM and broad homogenous sample illumination for OA tomography are provided. SPIM can be operated at multiple orientation angles, enabling subsequent image fusion and deconvolution based on reconstruction algorithms [74, 75]. In this way, multi-orientation SPIM datasets can be acquired. The OA tomography modality is based on a translating linear transducer array while the sample is rotated over 360° in discrete motion. The broad wavelength illumination range provided by an OPO laser allows to spectrally differentiate between endogenous absorbers.

The potential of array-based multispectral optoacoustic tomography was firstly demonstrated in the visible illumination range, allowing to image anatomical features deep within 2-month-old, opaque zebrafish. By applying linear unmixing algorithms,

strong endogenous absorbers such as melanin and oxy- and deoxy hemoglobin could be revealed. Extending the illumination range to the near-infrared region allowed to visualize endogenous contrast of water / lipid due to the increasing absorbance of these tissue components at higher wavelengths. However, due to the limited sensitivity of the array detector, hybrid optical and optoacoustic imaging of contrast generated by fluorescent proteins has not been possible yet with the existing modality. Thus, a next-generation OA tomography scanning approach based on highly sensitive single-element detectors is implemented into the system in the next chapter.

4 Implementation of spiral multispectral optoacoustic tomography

4.1 Introduction

The hybrid SPIM - OA tomography system based on linear transducer arrays has successfully demonstrated its abilities in the visualization biological development of zebrafish over long times scales. Moreover, the system has proven strength in high-resolution anatomical imaging of zebrafish and allows to visualize water/lipid contrast in zebrafish at unprecedented penetration depths. However, one of the initial goals of the system has not been achieved yet: Imaging of genetically labeled anatomical structures using fluorescent proteins like GFP deep inside the samples with the optoacoustic tomography modality.

In optical microscopy, fluorescent proteins had a revolutionizing effect on biological discovery due their ability be genetically encoded by a single portable DNA sequence [53, 153]. Thus, arbitrary structures can be labeled with GFP which enables microscopic observation of the specifically labeled structures of interest in developing organisms. Even though GFP exhibits a high QY and thus a low PGE, OA tomography has been able to detect fluorescent proteines such as GFP and mCherry at penetration depths which are not accessible to purely optical techniques [17]. However, the OA modality described by Razansky et al. [17] was limited to two dimensional image slices, thus it is not suitable for long term observation of biological development. The OA tomography modality based on the linear array transducer array, was however not able to detect fluorescent proteins at all, even in experiments with highly concentrated cells labeled with GFP.

Several considerations were hinting that the sensitivity of the transducer array is not strong enough to detect the relatively weak OA signals generated from fluorescent proteins compared to the strong OA signals from endogenous absorbers such as

melanin and hemoglobin:

- First, the sensitivity of a transducer scales with the size of the detector element surface [84]. Each transducer element of the array only has a surface size of pitch * elevation = 0.07 mm * 3 mm = 0.21 mm^2. However, typical single-element transducers such as the one applied in [17] exhibit diameters of ∼12.7 mm (0.5 inch). Thus, the total detector surface size corresponds to approximately 125 mm^2, which is about 600 times more.

- Second, the voltage signals from the transducer to the data acquisition (DAQ) unit are transmitted via a 2 m long cable without any pre-amplification. Hence, a lot of electrical noise is introduced. In contrast, for single-element detectors short cables of a length of about 10 cm can be used and then connected to an amplifier.

- The custom-built 128 channel DAQ unit is only able to amplify the signals by a factor of 10. No other hardware amplification can easily be implemented. In contrast, single-element detectors can easily be amplified by up to 63 dB right after a short cable. Thus, the electromagnetic noise introduced during the 2 m transmission to the DAQ card is much weaker in comparison with the transmitted signal.

4.2 Optoacoustic tomography with single-element detectors

4.2.1 Sensitivity considerations and comparison

To compare the sensitivity of the transducer array with single-element transducers at a similar frequency range, OA signal amplitudes generated by a 20 μm polysterene bead were measured.
Table 4.1 shows the specifications of the detectors used for the initial comparison.

Transducer	**Central Freq.**	**Bandwidth**	**Focal length**	**Diameter**
Olympus	25 MHz	51.78 %	12.5 mm	6.25 mm
Precision Acoustics	50 MHz	140 %	3.75 mm	5 mm
Vermon	24 MHz	51 %	5.8 mm	5 mm

Table 4.1: Transducers used for the initial SNR evaluation.

The sample was put in an agar cylinder in the sample chamber of the hybrid SPIM-OA system. The homogenous illumination field was used at ∼ 4 mJ and measurements were conducted in the focus of each detector. Data acquisition for

the array was performed with the 128 channel DAQ system (Falkenstein, Germany), digitization for the single-element transducers was performed with a DAQ card (RZE-002-400, Gage, USA) at a sampling rate of 200 MS/s. Figure 4.1 depicts the detected SNR as a function of averages.

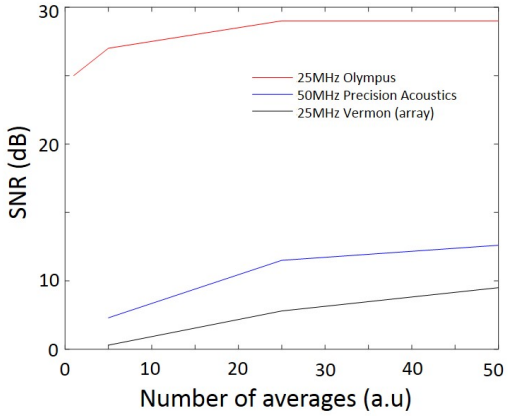

Figure 4.1: SNR of various available transducers at covering similar frequency bandwidths.

As can be clearly seen, the SNR of the of array (element with the highest signal intensity) is poor compared to the other evaluated single-element transducers. Especially without a sufficient number of averages, the signal can hardly be distinguished from the noise level with the transducer array. For this reason, multiple new single-element transducers were tested for the hybrid system. The following aspects were taken into account for the detectors of interest:

- First, a similar central frequency and bandwidth as compared to the transducer array were envisioned in order to keep a similar resolution with the SPIM modality.
- A large detector surface was required since detection sensitivity of piezoelectric transducers is proportional to detector surface [84].
- A spherically focused detector with a high NA. The spherical focus is necessary to maintain a strong lateral resolution, whereas the high NA is necessary to tighten the focus and to cover a broad angle behind the focus. Analogously to the focal spot size in optics, the focal spot size for ultrasound transducers scales with [116]:

$$f_D = 1.4 \cdot \lambda \frac{f}{d} \tag{4.1}$$

where λ corresponds to the acoustic wavelength and f and d correspond to the focal length and the diameter of the transducer respectively. Hence, a high NA reduces the focal spot size and consequently increases the lateral resolution. Furthermore, the ultrasound signals from all over the sample behind the focus can be detected simultaneously using a high NA. The high angular signal coverage of the detectors thus allows to neglect the lateral detector translation during an OA tomography scan, which strongly reduces the scanning time. Figure 4.2 illustrates the detection principle of spiral optoacoustic tomography based on high-NA transducers.

- Various piezo-electric elements should be tested (Piezo-ceramic, piezo-composite, PVDF, LiNb03)

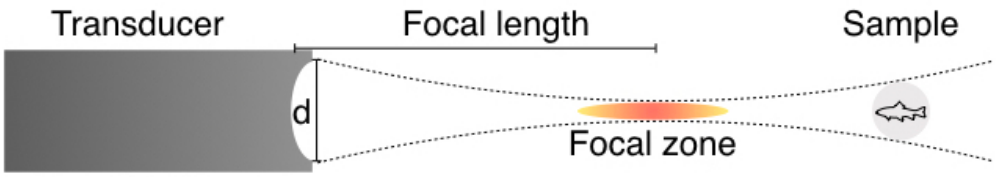

Figure 4.2: Detection principle of spiral optoacoustic tomography based on high angular signal coverage using high-NA transducers.

Table 4.2 summarizes the following configuration for the focal length and diameter of the detector were taken into account after consulting the manufactures on availability. For high-frequency transducers with the specified requirements of a high NA and a large surface, only custom-made detectors can be taken into account. The strong restrictions on the focal lengths and the surface diameter are due to the curvature of the transducer crystal, which is produced in a critical manufacturing process.

Focal length (mm)	Diameter (mm)	NA (a.u.)
6	6	0.84
10	10	0.84

Table 4.2: Configurations of the available high-frequency single-element detectors.

Several transducers could meet the specified requirements. Table 4.3 summarizes the properties of the single-element transducers as specified by the manufacturers:

These detectors were again tested for their SNR using a 50 μm microsphere in an agar sample. Figure 4.3 shows the SNR as a function of distance to the focus. Table 4.4 shows the maximum SNR in the focus of the transducer. As can be seen,

Manufacturer	Central Freq.	Bandwidth	Focal length	Material
Imasonic	20 MHz	78 %	10 mm	Piezo-composite
Precision Acoustics	25 MHz	71 %	10 mm	PVDF
Sonaxis	25 MHz	91 %	10 mm	Piezo-composite
Sonaxis	30 MHz	99 %	6 mm	LiNb03

Table 4.3: Properties of the single-element transducers used in the hybrid SPIM-OA system. The diameter for the elements corresponds to the respective focal length.

the Imasonic 20 Mhz transducer clearly exhibits the strongest SNR of $\sim$ 32 dB whereas the transducer array only achieves a SNR of $\sim$ 12 dB.

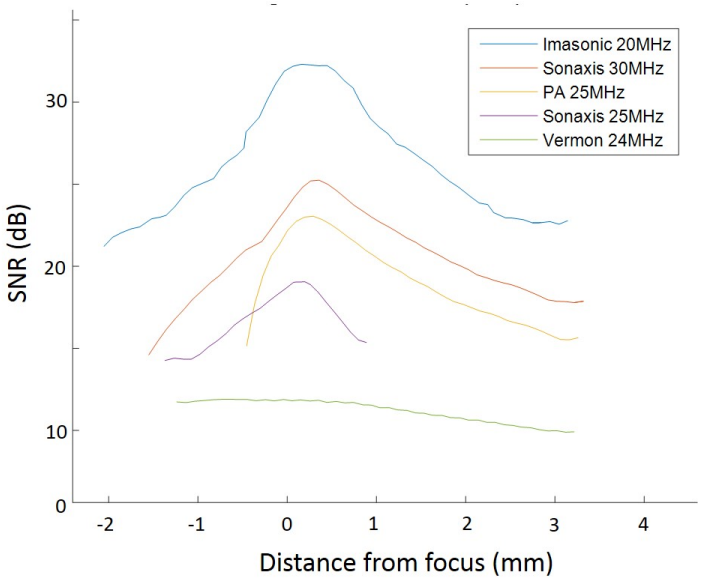

Figure 4.3: SNR comparison of single-element transducers suitable for the hybrid system. All detectors cover similar frequency bandwidths.

Transducer	SNR* (dB)
Imasonic 20 MHz	32
Sonaxis 30 MHz	25
Precision Acoustics 25 MHz	23
Sonaxis 25 MHz	19
Vermon array 24 MHz	12

*Measured in the focus of each transducer

Table 4.4: SNR measured in the focus for the new single-element transducers and the transducer array.

4.2.2 Characterization of single-element detectors

Since the Imasonic 20 Mhz detector's sensitivity clearly outperformed all other available transducers, research activities are conducted with this detector unless stated differently. In a first step, the sensitivity field of the detector was measured by translating a 20 μm polystyrene bead axially and laterally across the focal plane of the detector. The measurement was performed in the sample chamber of the hybrid system. For the scan, z-stage of the sample and the translations stage of the detector were used for axial and lateral scanning, respectively. The horizontal focal plane was found by lateral scanning of the sample using the y-stage and maximizing the OA signal before the actual scan was performed.

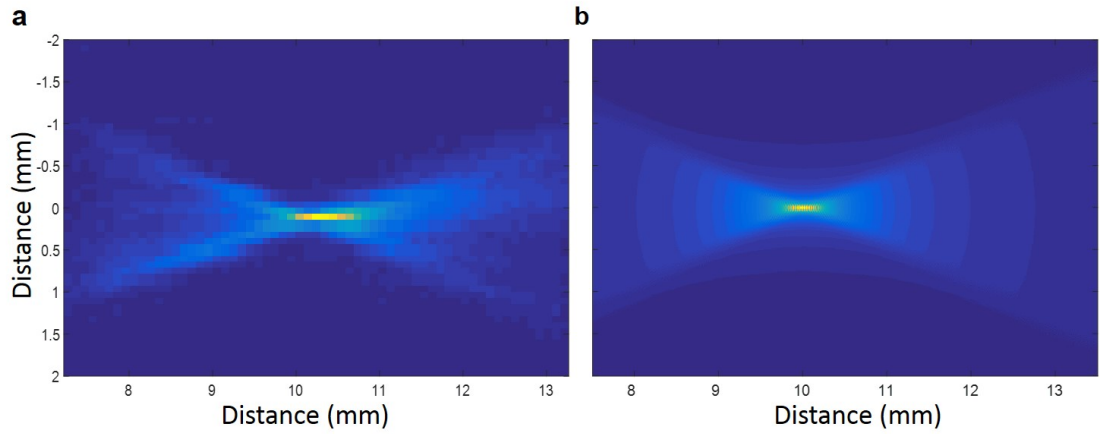

Figure 4.4: Sensitivity field of the 20 MHz Imasonic transducer. a) shows the measured sensitivity field, b) depicts the respective simulation based on the Matlab simulation package Field II [154]. The simulation in panel b) is a courtesy of Shyam Sri, Helmholtz Zentrum München.

In general, the measured and the simulated sensitivity fields based on the Matlab simulation package Field II match well (Figure 4.4). It can be observed that the measured focus is slightly further away (10.2 mm) from the transducer than the theoretical focus given by the manufacturer (10 mm). This may be due to the approximation for the speed of sound (1480 m/s) and inaccuracies for the scanning positions. Furthermore, deviations might be introduced during the manufacturing process.

The shape of the field and the high NA are a promising result since the sensitivity fields of other transducers do not necessarily exhibit such a good shape. For example, the sensitivity field of the Sonaxis 30 MHz detector (which exhibits the second best SNR in the sensitivity comparison measurements) is slightly cut off and

consequently not symmetric anymore. The cut field would cause reduced acoustic signal detection and thus inhomogeneous 3D images for any OA application. Hence, the detector is not usable for OA imaging.

However, as can be extracted from the OA signals shaping the sensitivity field, the spatial impulse response of the Imasonic 20 Mhz detector is problematic. As can be seen in figure 4.5, the strong side lobes of the OA signal of a microsphere will cause ringing artifacts when used for tomographic imaging approaches.

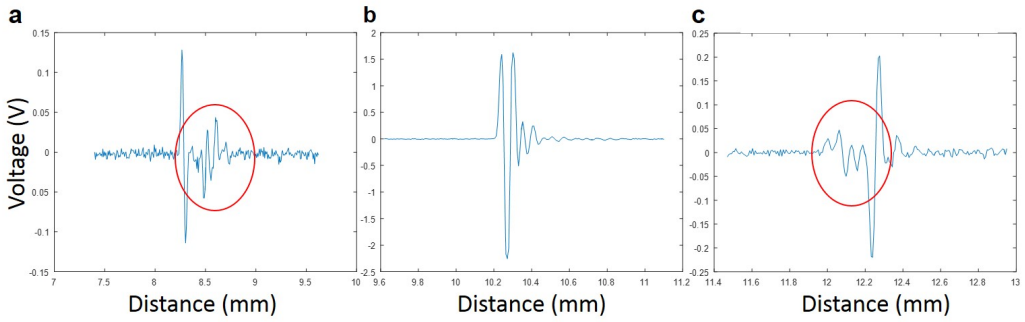

Figure 4.5: Signals of the highly sensitive 20 MHz Imasonic transducer. a) 2 mm in front of the focus, b) in focus, c) 2 mm behind the focus.

Hence a new detector (Imasonic, France) with the same characteristics but with an apodization of the outer part of the detector was implemented. Its sensitivity was compared with the non-apodized Imasonic transducer in a mid-infraread optoacoustic microscope [155], where a focused mid-infrared beam optically excites the strongly absorbing surface of water. This has the advantage that lateral and axial offsets of the detectors can be avoided and the comparison becomes more accurate. Results of the measurements performed with an oscilloscope show that the sensitivity of the apodized detector outperforms the non-apodized by ~100 mV (figure 4.6 c),f)). Furthermore, the signal artifacts 2 mm behind the focus for the apodized detector disappeared (see figure 4.6 e)).

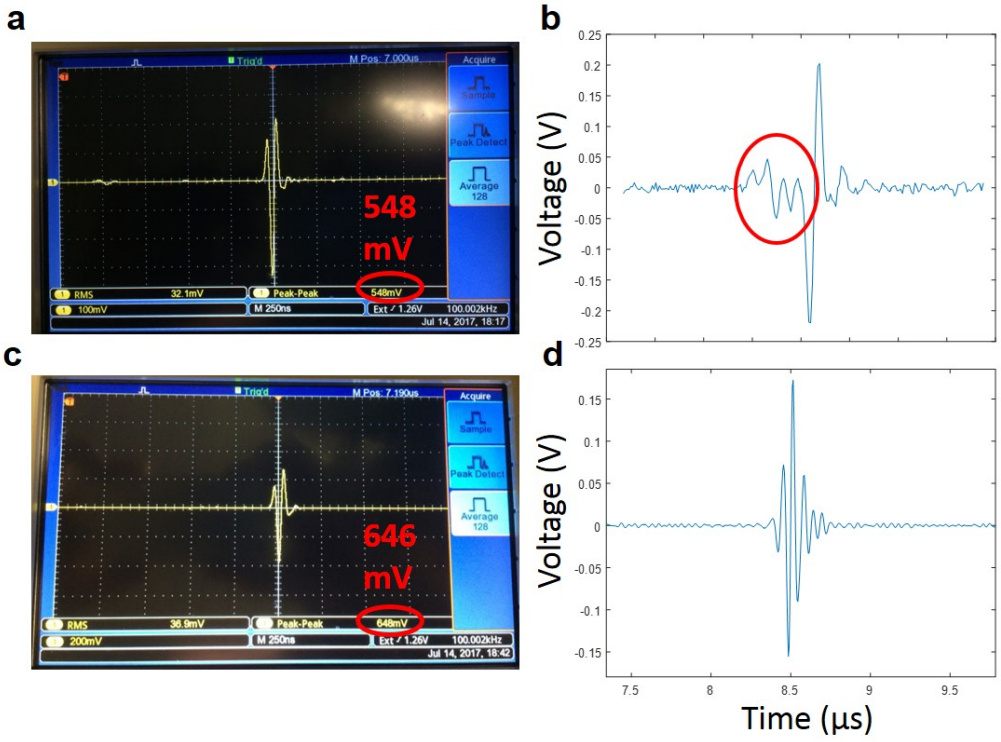

Figure 4.6: Signals of the non-apodized (top row) and the apodized (bottom row) 20 MHz Imasonic transducer in focus and 2 mm behind the focus. a) non-apodized, in focus, c) non-apodized 2 mm behind the focus c) non-apodized, signal amplitude, d) apodized, in focus. The figures in panel a) and c) are a courtesy of Dr. Miguel Pleitez, Helmholtz Zentrum München.

Furthermore, side lobes behind and in front of the focus in the sensitivity field of the apodized detector are much weaker, hence the detector can be used for imaging applications.

Consequently, the OA impulse response of the detector needed to be evaluated in order to determine the bandwidth and to possibly include the transducer's impulse response in the image reconstruction. For this reason, the impulse response was measured in an OA microscope [156] using a 200 nm thick gold plate as a point source for the OA signal generation. Figure 4.7 shows the measured impulse response for the 20 MHz Imasonic detector in time and frequency-domain. As can be seen, the bandwidth at the -6 dB drop covers a frequency range from $\sim 13 - 27$ MHz, which results in a relative bandwidth of ~ 70 %. The high sensitivity and the clean OA signals without side lobes behind the focus are promising results for the implementation of the detector in the hybrid system for OA imaging

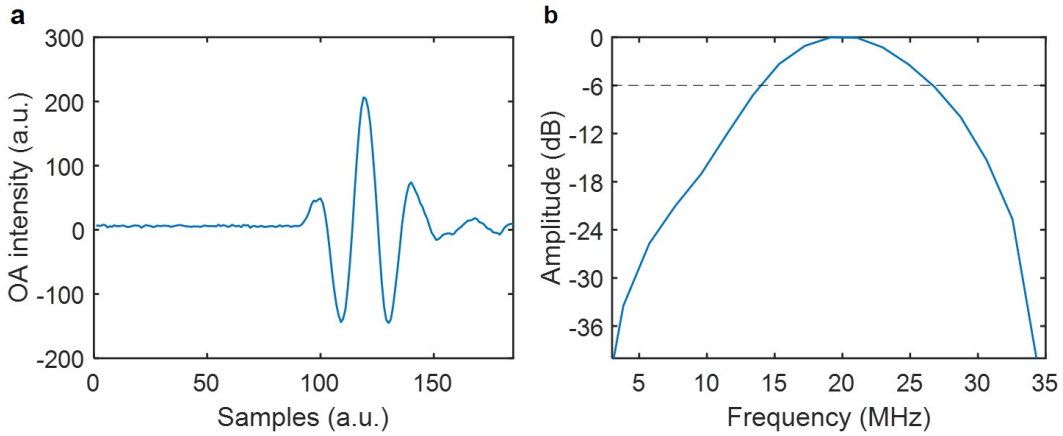

Figure 4.7: Demonstration of the impulse response of the Imasonic 20 MHz transducer in a) time-domain and b) frequency-domain. The dashed line denotes the OA signal intensity drop at -6 dB. The signal was recorded with a high NA focused beam on a 200 nm thin gold plate in a multimodal optoacoustic microscope (see reference [156]). The measurement in the focus of the detector was averaged over N=1000 acquisitions at a sampling frequency. More details of the system can be found in [156]. The data is a courtesy of Markus Seeger, Helmholtz Zentrum München.

4.3 System implementation and characterization

The single-element detectors are implemented in the hybrid system with a newly designed Aluminium holder in the sample chamber, which can be easily integrated in the rail for the transducer array holder. Furthermore, a 63 dB amplifier (AU-1291, Miteq, USA) was installed next to the sample chamber in order to connect the short 10 cm cable from the transducer to the amplifier. The data acquisition is performed with the 200 MS/s DAQ card (RZE-002-400, GaGe, USA) used in previous experiments. The implementation of the single-element detectors into the hybrid platform for spiral optoacoustic tomography requires proper calibration both mechanically within the system and in software for scanning and reconstruction. Figure 4.8 shows the schematic of the spiral scanning geometry and the implementation of the single-element detector in the sample chamber. Spiral optoacoustic tomography is performed by sample rotation over 360° and simultaneous translation of the sample at slow speeds in the negative y-direction. This scanning approach can be either performed at predefined discrete scanning positions and detecting the OA signals at these positions or continuous sample rotation and translation and detection of OA signals at every trigger signal indicating the emission of a laser pulse. Details on both discrete and continuous scanning approaches for OA tomography in the

hybrid system will be described in the following sections.

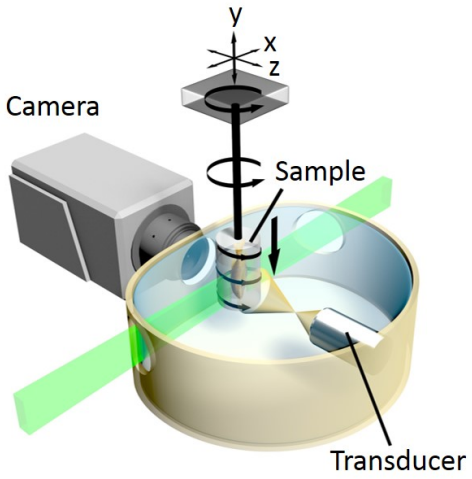

Figure 4.8: Sample chamber of the hybrid MSOT-SPIM system with the implemented single element detector. Scanning of the sample is performed by rotating the sample over 360° and simultaneous vertical translation of the sample in the negative y-direction. Adapted from [139].

Proper alignment of the detector in three dimensions requires a fixed and central position in respect to the sCMOS camera in the lateral x-direction, so that the transducer detects OA signals generated in the collimated focused beam. The lateral position of the detector in the y-direction is centrally predefined by the holder. The axial detector position in the z-direction however needs to be aligned within the detector holder rail, so that the sensitivity field covers the complete lateral width of the sample. By applying basic geometric considerations, it can be deduced that the radius R from the center of the sample to the detector is given by:

$$R = f_c + \frac{w}{2tan(\gamma)} \tag{4.2}$$

where w corresponds to the sample width and $tan(\gamma)$ to the f-number of the detector defined by its diameter d and its focal length f_c following $tan(\gamma) = \frac{d}{f_c}$. Thus, for a typical juvenile zebrafish with a diameter of $\sim$ 4 mm, and the f-number=1 ($tan(\gamma) = 1$) of our detectors, a radius slightly greater than $R \geq 12$ mm is suitable. Since the sensitivity of the detector decreases as a function of distance to the focus (see figure 4.3), smaller samples can be imaged at higher sensitivity allowing to image structures that generate weaker OA signals. In a next step, the sample needs

to be positioned in the center of the transducer in x-direction with the motor stage, and slightly above the detection-surface of the detector in y-direction in order to enable scanning of the full sample.

For image reconstruction, a back-projection algorithm is applied by considering the focal spot of the transducer as a virtual point detector. Thus, the reconstruction radius R-tomo does not include the focal length f_c anymore. The recorded time transients can consequently be cut off with a delay time corresponding to $t_{del} = f_c/v_s$ at a speed of sound $v_s \approx 1480$ m/s in water at room temperature. The scanning positions are precisely provided by the motor stages during the acquisition for both discrete and continuous scanning and can be directly used for the reconstruction. However, the back-projection algorithm for the hybrid system introduced in [147] needs to be adapted. The new scanning positions for spiral tomography need to be included, and the new reconstruction parameters need to be considered. For spiral OA tomography, besides the tomography radius R-tomo, the focal length f_c from the detector to the virtual focal spot and the angular tilt α between the rotation axis of the sample and the transducer need to be considered. Figure 4.9 illustrates the relevant reconstruction parameter for spiral OA tomography.

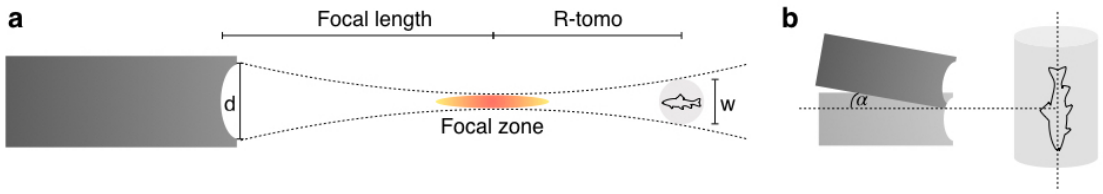

Figure 4.9: Reconstruction parameters used in the back-projection algorithm for spiral OA tomography. a) Top view of the reconstruction geometry, highlighting the reconstruction radius R-tomo. The diameter of the active element of the transducer is labeled d, the sample is labeled as w. b) Side view of the reconstruction geometry defining the angular correction parameter α between the sample rotation axis and the transducer. The transducer above corresponds to a real case alignment introducing the angular tilt α, the lower transducer corresponds to an ideal calibration yielding in $\alpha = 0$.

Theoretically, the angle between the rotation axis and the transducer is precisely 90°, however there is typically an angular deviation $\alpha \leq 1°$. Finding of the reconstruction parameters R-tomo and α is performed by a calibration scan with a known phantom sample and subsequent reconstruction iterating through a reasonable value range of the relevant reconstruction parameters. The method has been introduced in [157], however only for linear transducer arrays in a limited view translation-rotation

tomography over max. 180°. The calibration phantom of choice is an agar cylinder with two parallel surgical sutures of 50 μm diameter, which generate extremely strong OA signals within the frequency detection bandwidth of the transducer. Furthermore, the length of the approximately straight surgical sutures allows precise assessment of the angular tilt parameter α. Figure 4.9 illustrates the geometry of the reconstruction parameters. As an example, figure 4.10 shows the calibration of the reconstruction parameter R-tomo by illustrating the effect of deviating parameter in a range from -200 μm to + 200 μm.

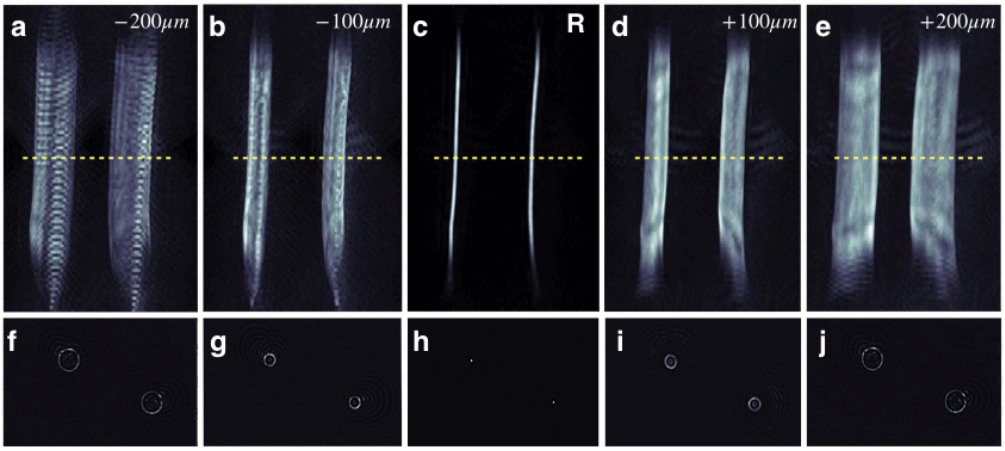

Figure 4.10: Calibration of spiral optoacoustic tomography. a-e) Side view MIP (y-z plane) of two reconstructed parallel sutures at multiple reconstruction parameters R-tomo ranging from the radius R-tomo - 200 μm to R-tomo + 200 μm. The image size corresponds to 2 x 5 mm in width and height respectively. The yellow dotted line denotes the central cross-sectional slides (x-z plane) of the reconstructions shown in f-j) at the respective reconstruction parameter R-tomo shown in the top row a-e).

4.3.1 Discrete spiral optoacoustic tomography

First imaging approaches were conducted with a spiral scanning approach, where the sample is vertically translated along the y-axis in front of the transducer and simultaneously fully rotated over 360° multiple times. To facilitate the spiral scanning geometry, the first spiral OA tomography implementation was executed in discrete motion, meaning that all scanning positions of the motor stages were initially defined and the OA acquisition was only performed when both stages were fixed at their respective position. Table 4.5 summarizes typical scanning parameters of a discrete spiral OA tomography scan in the hybrid system.

Figure 4.11 a) illustrates the discrete scanning positions of the discrete scan, whereas figure 4.11 b) and c) show phantom imaging results of 50 μm beads which allow to

Angular stepsize	2.4°
Vertical stepsize	1.83 μm
Image height	6 mm
Number of wavelengths	1
Number of projections	$\sim$ 3300
Scan duration	$\sim$ 40 min

Table 4.5: Overview of the scanning parameters for a typical discrete spiral OA tomography scan.

approximate the resolution. Using the 25 MHz transducer from Precision Acoustics, the in-plane resolution in x- and z-direction can be approximated on full width at half maximum (FWHM) profiles of the beads with $\sim$ 50 μm whereas the transversal resolution along the scanning direction (y-axis) is $\sim$ 100 μm.

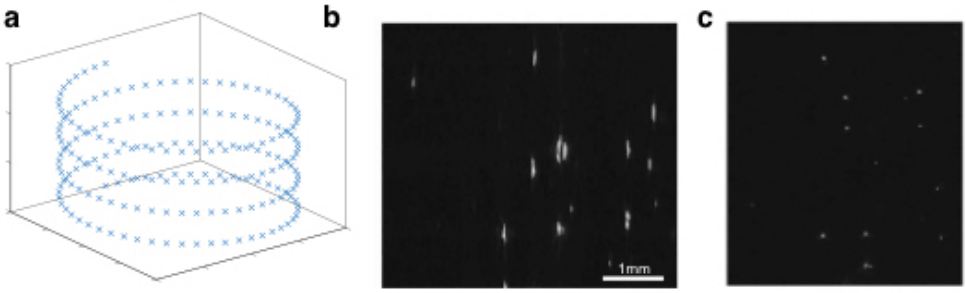

Figure 4.11: Discrete scanning with single-element detectors. a) Discrete scanning positions of the single-element detector in respect to the sample during a spiral OA tomography scan. b) Side view MIP of a 50 μm bead phantom. b) Top view MIP of the same 50 μm beads phantom. The in-plane resolution in x- and z-direction (panel c)) was determined to be $\sim$ 50 μm whereas the transversal resolution along the scanning direction (y-axis) was calculated with $\sim$ 100 μm based on the FWHM of the beads. Measurements were performed using the 25 MHz detector from Precision Acoustics.

However, this imaging approach has several drawbacks:

- It is slow since the motor stages are started and stopped at every scanning position.
- The number of projections is limited due to the slow scanning speed. In theory, the number of projections can be increased but at the cost of even further increasing the total scanning time. Due to the relatively low number of projections, the image quality suffers especially in case of larger specimen with more complex structures.

- Photobleaching of labeled structures using fluorescent proteins within the biological samples is high, due to the high number of laser pulses that illuminate the sample during the sample movement when no data is acquired.
- Discrete scanning cannot easily take advantage of the sweep mode of the laser enabling a wavelength change on a pulse to pulse basis. This limitation is due to the unknown point of time when an OA acquisition is performed after the movement of the sample. Thus, manual wavelength tuning is required for an OA scan at each scanning position, which is again a slow process that takes ~ 0.7 s. For several thousand scanning positions, this will further dramatically increase the scanning time and thus increase the photobleaching.

Figure 4.12 shows typical imaging results using the discrete scanning mode of the system using the 25 MHz detector from Precision Acoustics.

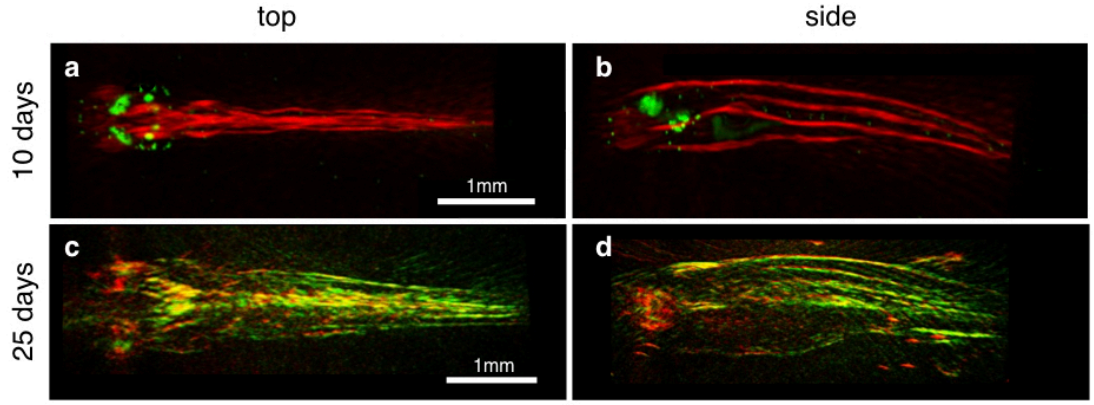

Figure 4.12: Discrete spiral OA tomography imaging of 10 and 25 days old zebrafish. a) Top view MIP of a hybrid image combining SPIM (green) and spiral OA tomography (red) of a 10-day-old zebrafish (Brn3c:GFP) expressing GFP in hair cells. b) Side view MIP of the same zebrafish. c) Top view MIP of a multispectral spiral OA tomography reconstruction of a 25-day-old zebrafish (Brn3c:GFP) imaged at 488 (green) and 550 nm (red). d) Side view MIP of the same zebrafish.

It can be clearly seen that this approach yields good results for small model organisms such as 10-day-old zebrafish imaged with the SPIM (green) and the spiral OA tomography (red) modality respectively (figure 4.12a) andb)). However, due to the low number of projections the image quality deteriorates for older and thicker samples. Panel 4.12c) and 4.12d) show the top and side view of a 25-day-old transgenic zebrafish (Brn3c:GFP), demonstrating the high noise level of the reconstruction. Due to these limitations, the system was further pushed toward continuous OA tomography scanning by using the highly sensitive 20 MHz Imasonic single-element detector.

4.3.2 Continuous spiral optoacoustic tomography

First trials to implement continuous scanning with the single-element detector did not result in any meaningful reconstructed OA images. It was expected that the assignment of the scanning positions was wrong so that the reconstruction was disarranged. However, thorough data analysis revealed that the spatial sampling was insufficient. This means that the ratio of the scanning speeds of the rotation and the vertical translation stages during the scan did not match. While the rotation stage was set to the maximum speed of 7 °/s the vertical translation was too fast so that the number of projections per full rotation cycle was insufficient. Only by decreasing the scanning speed of the translation stage to ≤ 5 μm/s, a reasonable image quality for phantoms could be achieved.

Figure 4.13 demonstrates the effect of spatial sampling with the vertical translation stage and the rotation stage by showing the OA projections of a scan over 1 cm in y-direction and a respective reconstruction. A vertical translation at 10 μm/s and a rotation speed of 5 °/s (see figure 4.13 a)) results in strong reconstruction artifacts in the reconstruction (figure 4.13 b)). On the other hand, by increasing the spatial sampling, i.e. decreasing the vertical translation speed by a factor of 2 (5 μm/s) and equally increasing the rotation speed to the maximum speed provided by the stage (7 °/s), the number of sinusoidal projection helices in the vertical scanning area of 1 cm strongly increase (figure 4.13 c)). Figure 4.13 d) shows a respective reconstruction for the scanning parameters, which demonstrates a clean OA image for two parallel surgical sutures. The weak background noise can further be reduced by decreasing the vertical scanning speed which however comes at a trade-off between background noise and acquisition time.

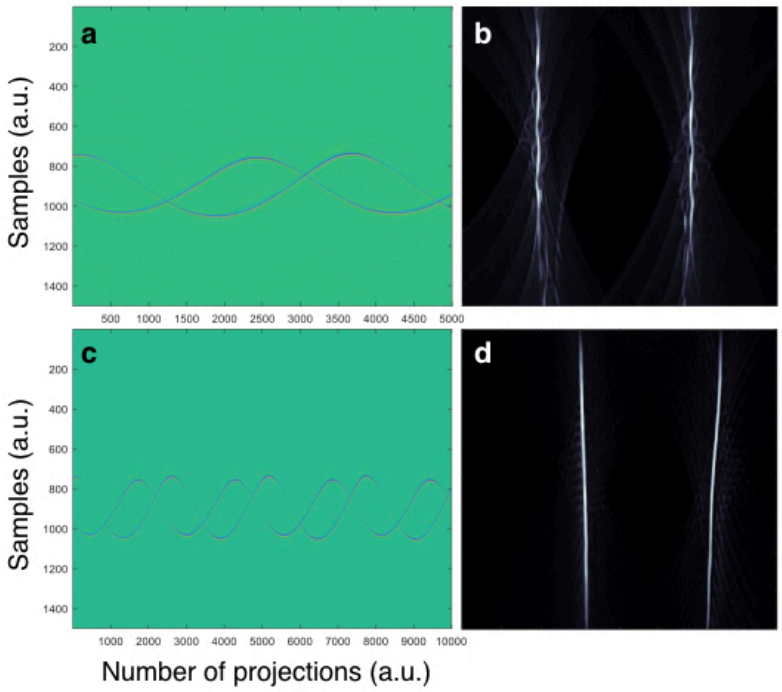

Figure 4.13: Effect of spatial sampling in continuous spiral optoacoustic tomography. a) OA time transients of two parallel surgical sutures illustrated over the number of projections. The imaging height of the acquired signals corresponds to 1 cm, the rotation speed was 5 °/s and the vertical translation speed at 10 μm/s. b) Reconstruction at a corresponding spatial sampling rate. c) OA signals of two parallel sutures over 1 cm of imaging height acquired at a rotation speed of 7 °/s and a vertical translation at 5 μm/s. d) Reconstruction at a corresponding spatial sampling rate. The images are sized 4 ×4 mm.

Thanks to the strong SNR of the Imasonic 20 MHz detector, continuous scanning does not need any averaging and thus every laser pulse during the scan generates an OA projection that can be used for subsequent image reconstruction. At a laser repetition rate of 50 Hz and the rotation speed of $7°/s$, a projection at an angular stepsize of 0.14° is generated. In the vertical direction, the image quality can be defined by the translation speed at the cost of scanning time. For a high-resolution scan, 2.5 μm/s are selected, which yields in an OA acquisition stepsize of 50 nm. Due to this high angular resolution up to 8 wavelengths can be applied in one scan in the sweep mode of the laser without any significant loss in image quality. The assignment of the OA pulses to their respective wavelength is done with the simultaneously recorded data of a photodiode (DET36A, Thorlabs, Germany) which has a distinct response to different wavelengths. Table 4.6 summarizes typical scanning parameters of a continuous OA tomography scan in the hybrid system.

Repetition rate	50 Hz
Rotation speed	7 °/s
Translation speed	4 μm/s
Number of wavelengths	2
Image height	9 mm
Number of projections	$\sim$ 150000
Scan duration	$\sim$ 37.5 min

Table 4.6: Overview of the scanning parameters for a typical continuous spiral OA tomography scan.

4.3.3 System characterization

Noise characterization

A high SNR of the OA tomography modality does not only require a high detection sensitivity of the detector, but also a low electronic noise level. Thus proper shielding for the detector needs to be installed in order to remove any electronic noise introduced by surrounding devices. Even though the single-element transducers are delivered with a double-shielded cable, a strong shielding with a metallic hose is crucial to reduce the noise level by almost a factor of 10. It is particularly important that the shielding hose does not only cover the cable itself, but also connectors and the SMA connector on the amplifier side and the edge of the transducer.
Figure 4.14 shows the noise level with and without metallic shielding in both time and frequency domain. As can be clearly seen, proper shielding strongly reduces the noise level of the system so that the SNR increases from 29 to 41 dB. The electronic noise peaks at ~32 MHz are probably introduced by the motor stages and can be suppressed with proper shielding. For the 1.5 m cable from the amplifier to the transducer, a high-quality double shielded cable with SMA connectors on both sides is used. Here, additional shielding with a metallic hose does not further reduce the noise level.

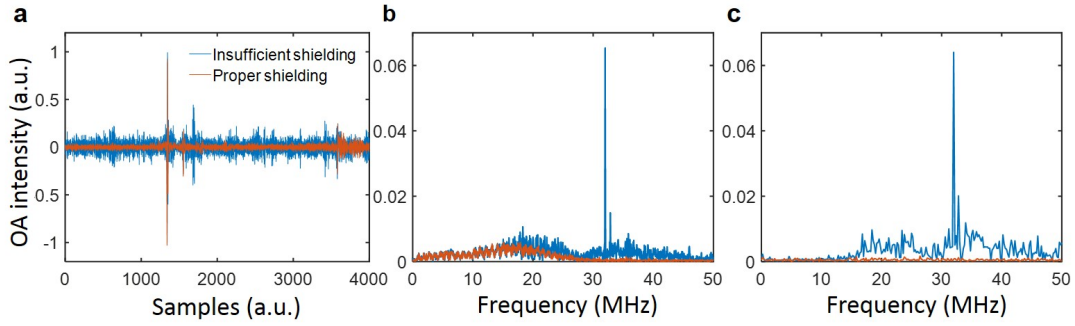

Figure 4.14: Noise characterization of the OA modality based on the Imasonic 20 MHz single-element detector. a) OA time transient of two parallel surgical sutures with proper and insufficient shielding. b) Fast Fourier transform (FFT) of the transient shown in a). c) Frequency-domain spectrum of the first 1000 samples shown in a) (excluding the signal generated by the sample).

Resolution and depth

While the sample illumination remains the same for the OA acquisition with the single-element as for the array (see chapter 3), the OA detection and the scanning geometry have evolved tremendously. This effects the general image quality and the resolution of the system, which requires a new characterization of the system. Figure 4.15 shows the OA reconstructions of 10-20 μm and crossed sutures of 20 μm diameter that can be used to characterize the resolution of the scan. Since the transducer bandwidth can detect frequencies up to $\sim$ 30 MHz at a attenuation of -6 dB, the expected resolution is $\sim$ 40 μm and samples of $\leq$ 20 μm diameter can be considered as suitable point sources for the frequency bandwidth of the detector. Figure 4.15 a) and b) show the MIPs of a single 10- 20 μm microsphere from top (x-z plane) and side view (y-z plane) respectively. The intensity profile in all dimensions is demonstrated in panel 4.15 c), which allows to determine the resolution by calculating the FWHM of the fitted Gaussian profiles. Thus, the resolution can be determined to be $\sim$ 35 μm for both the horizontal x and z dimension and $\sim$ 100 μm in the vertical y-direction. Furthermore, figure 4.15 d) demonstrates the spatially invariant lateral and axial resolution over a large FOV by showing the side view MIP of two crossed 20 μm surgical sutures.

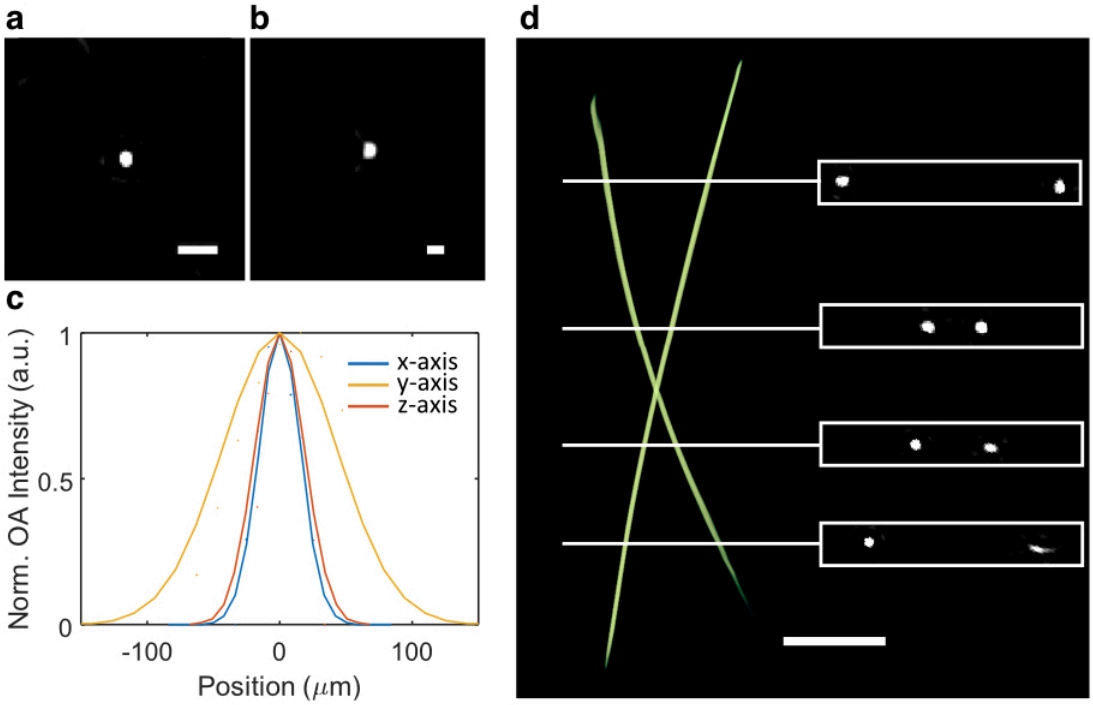

Figure 4.15: Characterization of the resolution of the spiral OA tomography modality based on the Imasonic 20 MHz single-element detector. a) Top view of a 10-20 μm m bead used for determining the lateral resolution in x and y-direction, b) Side view of the same bead. c) Profile and Gaussian fit of the bead in all spatial dimensions. d) Demonstration of the spatially invariant lateral and axial resolution in a large FOV image by two surgical crossed sutures of 20 μm diameter. The scale bars in a) and b) correspond to 100 μm, the scale bar in d) to 1 mm.

In phantoms such as microspheres, homogenous resolution over the whole FOV can be demonstrated. However, acoustic attenuation needs to be considered for biological tissue of several mm in thickness. According to equation 2.34, the acoustic attenuation increases linearly for higher frequencies with $\alpha_0 = 0.5\ dBMHz^{-1}cm^{-1}$. In general, the maximum frequency that is detected at a resolution of 35 μm resolution is $\sim$ 42 MHz. Thus, the acquired acoustic spectrum is still below the cut-off frequency at about 43 MHz, where the acoustic attenuation becomes stronger than the optical attenuation [82]. The sample holder of the system is designed for samples up to 10 mm in diameter. Since the system is based on tomography, only depths up to 5 mm need to be taken into account.

Based on equation 2.34, the maximum detectable penetration depth of a certain frequency attenuated by -6 dB can be simulated. At a given speed of sound of $v_s = 1480$ m/s, this allows to simulate the maximum achievable resolution based on $v_s = \lambda \cdot f$, where λ corresponds to the acoustic wavelength and thus the maximum

acoustic resolution at a given frequency. Figure 4.16 a) illustrates the maximum achievable penetration depth as a function of frequency in OA tomography. Figure 4.16 b) consequently shows the maximum achievable resolution in OA tomography as a function of penetration depth. The results of the simulations reveal that the measured resolution of ~ 35 μm can only be obtained up to depths of ~ 3 mm in tissue, while a resolution of 60 μm can be achieved in depths up to 5 mm in thick biological samples. With the tomographic approach in the hybrid system, samples of 10 mm in diameter can be imaged with resolutions lower than from 35-60 μm over the whole FOV.

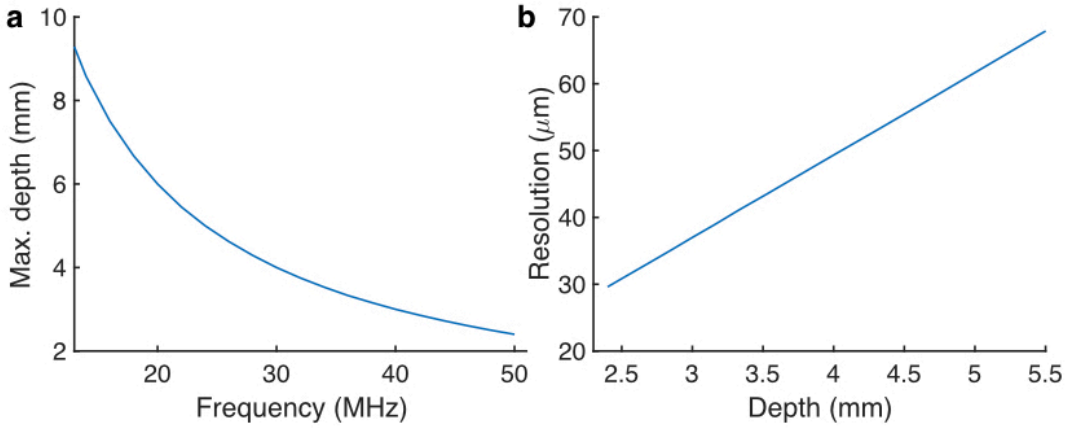

Figure 4.16: Simulations on the effect of acoustic attenuation on the image resolution as a function of depth. a) Maximum imaging penetration depth of acoustic frequencies at an attenuation of -6 dB. b) Resolution as a function of imaging depth based on the attenuation of acoustic frequencies.

Contrast

Another critical characteristics in biomedical imaging is the contrast, which can be characterized by the CNR. Likewise to the SNR, the CNR increases with the number of projections $\propto \sqrt{N_{pro}}$ and can be expressed with:

$$CNR = 20 \cdot log(\frac{contrast}{noise}) \tag{4.3}$$

Here, as a quantity for contrast, the standard deviation of a ROI with maximum contrast within the image is taken, the noise is calculated by the standard deviation of a larger image background ROI. Figure 4.17 shows the typical reconstructed MIPs of a cross-sectional view of a zebrafish reconstructed at multiple number of projections N_{pro} from 56250 down to 878.

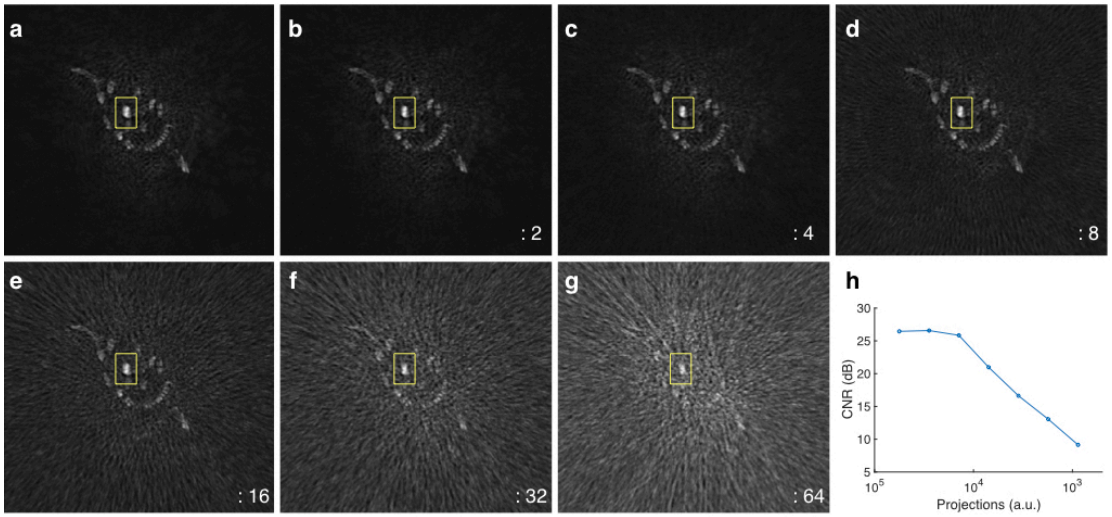

Figure 4.17: Effect of the number of projections on the CNR. a-g) MIP of slices of a reconstructed zebrafish (300 μm depth) starting at 56250 projections and iterative decrease of the number of projections by a factor of 2 down to 878 projections for the whole sample. The image size corresponds to 4 × 4 mm. h) The CNR as a function of projections extracted from the ROI marked in yellow in panels a-g).

In each panel, the illustrated MIP is based on a reconstruction with every second projection removed compared to the previous MIP. As can be seen, the CNR strongly decreases from a maximum of $\sim$ 26 dB after three iterations (panel 4.17h)). Interestingly, the CNR however is more or less constant at N_{pro}=56250, N_{pro}=28125 and N_{pro}=14562. Consequently, this allows to image at four our even eight different wavelengths during one scan without significant losses in CNR.

4.4 Multispectral spiral optoacoustic tomography

Imaging of transgenic zebrafish

To exploit the high sensitivity of the 20 MHz Imasonic transducer and the multispectral illumination of the OPO laser, a 45-day-old transgenic zebrafish (cldnb:GFP, sqET4:GFP) labeled with GFP was imaged with the SPIM and the spiral OA tomography modality of the hybrid system. The OA acquisition was performed in continuous mode at a vertical translation speed of 4 μm/s and a rotation speed of 7 °/s, which yields a sufficiently high spatial sampling rate to use the sweep mode of the OPO laser at two different wavelengths. Thus, the sample could be alternately illuminated at 488 and 550 nm. These two wavelengths correspond to the maximum absorption peak and almost no absorption in the absorption spectrum of GFP,

respectively (see figure 2.5). Simultaneously to the OA signal acquisition, fractions of the pulse illumination were measured with a photodiode (DET36A/M, Thorlabs, Germany) in order to assign the OA signals to their respective illumination wavelength.

Figure 4.18 illustrates the imaging results of a 45-day-old transgenic zebrafish (cldnb:GFP, sqET4:GFP) acquired with both modalities of the hybrid system. Panel 4.18 a) shows the MIP overlay of the OA reconstructions at 488 (green) and 550 nm (red) respectively. Panel 4.18 b) shows the MIP of the differential image (488 - 550 nm), indicating strong OA signal generated by an absorber only absorbing at 488 nm and not at 550 nm. Since all endogenous absorbers such as hemoglobin and melanin strongly absorb at both wavelengths respectively, the differential image can be attributed to the transgenic label GFP. This is in good correspondence with reference [17], where cross-sectional slides of the transgenic labeling along the lateral line of a zebrafish are presented. Panel 4.18 c) shows the cross-section at the respective ROI marked in panel 4.18 a). A MIP of the respective SPIM image is presented in panel 4.18 d), the fluorescence image is however affected by autofluorescence generated at the surface of the fish. A hybrid absorbance - optoacoustic extinction spectrum of superfolder-GFP (sfGFP) measured in a microfluidic chip (µ-Slide I 0.2 Luer, hydrophobic, uncoated, Ibidi, Germany) in the system described in chapter 5 and in [27] is shown in panel 4.18 e). The spectrum demonstrates the strong OA signal generation of GFP at 488 nm in contrast to 550 nm, where no OA signals can be generated. sfGFP is a GFP mutant that exhibits nearly the same absorption spectrum as eGFP at a slightly higher QY of 0.65 compared to 0.6 of eGFP [158–160].

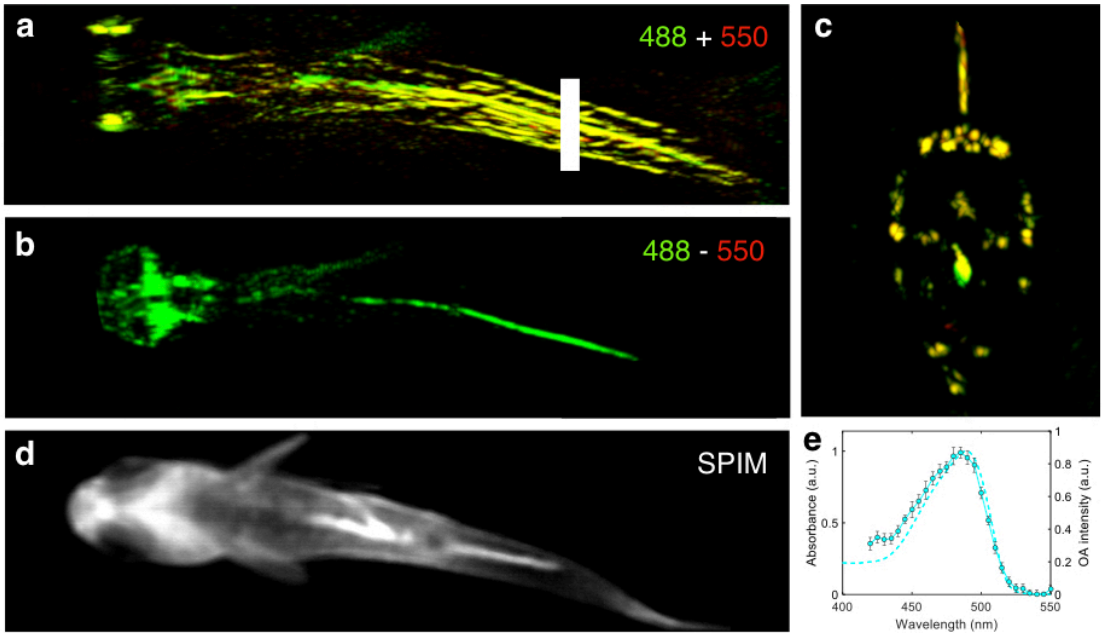

Figure 4.18: Spiral multispectral optoacoustic mesoscopy of a 45-day-old transgenic zebrafish (cldnb:GFP, sqET4:GFP). a) MIP of an OA reconstructions at 488 (green) and 550 nm (red) of the transgenic zebrafish. b) Difference image (488-550 nm) MIP of the same OA volumes in a). c) Cross-sectional MIP of a region below the fin. d) Average intensity projection of the volumetric SPIM images of the same fish acquired in the hybrid modality. e) Absorbance and OA spectrum of superfolder-GFP, measured with a hybrid absorption - OA spectrometer explained in chapter 5 and in [27].

Frequency decomposition

Furthermore, the contribution of the different frequency bands in the reconstruction of the 45-day-old transgenic zebrafish illustrated in 4.18 was investigated. Figure 4.19 a) shows the cumulative spectrum of all OA signals contributing to the reconstruction and the decomposed subspectra used for the bandpass-filtered reconstruction for all three frequency bands. Panels 4.19 b-d) show the reconstructions of the zebrafish at three frequency bands covering low (2-10 MHz), mid (10-18 MHz) and high (18-35 MHz) frequency bands, whereas panel e) illustrates the cross-section of the ROI marked in panels b-d) in red, green and blue. As can be seen, the strongest contrast can be attributed to the low frequency band, whereas high frequencies only weakly contribute to the overall contrast. However, finer structures can be only revealed within the higher frequency reconstruction.

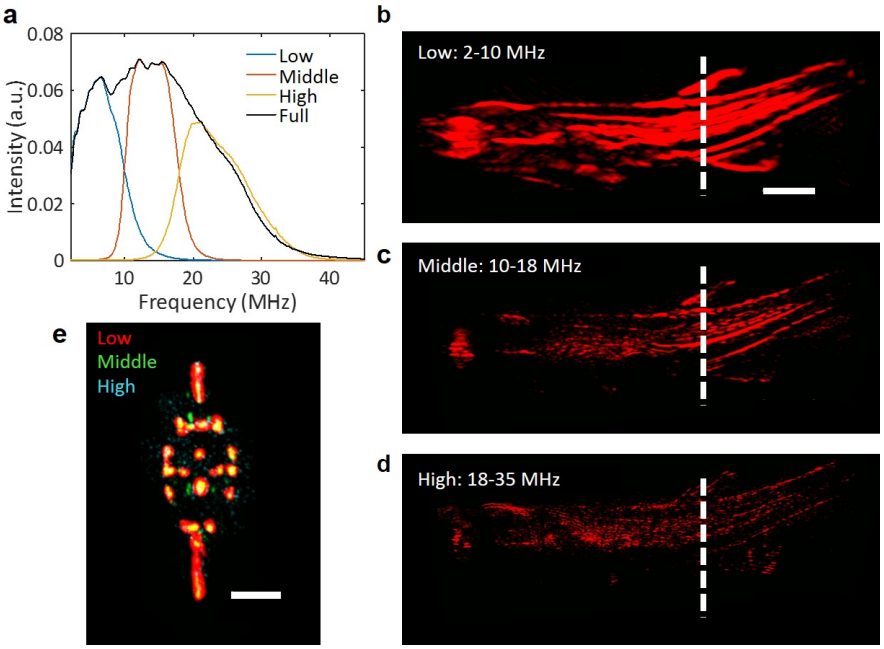

Figure 4.19: Frequency decomposition of the OA reconstructions of a 45-day-old transgenic zebrafish. a) Mean frequency spectrum of all OA projections of the fish after filtering with a butterworth-filter (third order) for low (2-10 MHz), middle (10-18 MHz) and high (18-35 MHz) frequencies as well as the full spectrum. b) Panels b)-d) show the respective reconstruction of the full fish, e) depicts the overlayed slice marked in b-d) for each reconstruction volume. The scale bar in b)-d) and e) correspond to 1 mm and 500 μm respectively.

4.5 Further system implementations

Another example for the versatile imaging capabilities of the hybrid platform is the implementation of raster-scanning optoacoustic mesoscopy (RSOM) as presented in [104, 105]. Based on the multiple motor stages available in the system, the sample can be vertically translated along the negative y-direction while the single-element transducer is laterally translated in x-direction. Thus, a complete raster-scanning grid over a large FOV can be established. In its first implementation in the hybrid platform, scanning was performed with discrete motion at a stepsize of 100 μm in both directions, which roughly corresponds to the focal spot size of the 20 MHz single-element detector and defines the lateral resolution. In contrast to the high-resolution modality based on detectors with central frequencies at 50 and 100 MHz presented in [104, 105], the axial resolution using the 20 MHz detector is much lower and in the range of the 35 μm as discussed previously. Again, the axial resolution depends on the depth of the biological samples due to acoustic

attenuation at higher frequencies. The image reconstruction is performed with a back-projection algorithm. Figure 4.20 a) shows the scanning pattern of the raster-scanning optoacoustic mesoscopy implementation in the hybrid system. The sample is vertically translated in y-direction in discrete motion, whereas the spherically-focused ultrasound detector is horizontally translated in the x-direction of the system. Figure 4.20 b) showcases typical phantom imaging results.

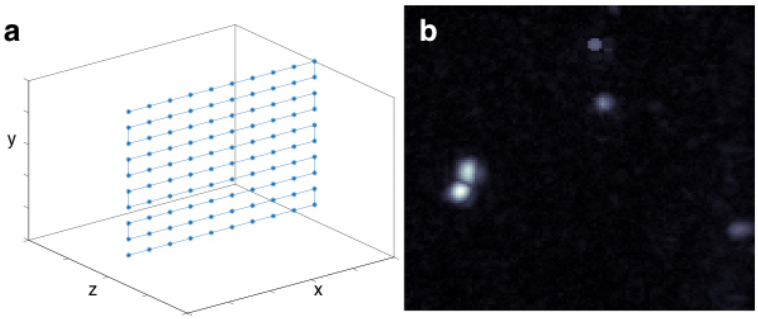

Figure 4.20: Implementation of raster scanning optoacoustic mesoscopy and ultrasound imaging in the hybrid system. a) 3D scanning pattern of the ultrasound transducer for both raster-scanning optoacoustic mesoscopy and ultrasound imaging. While the sample is vertically translated, the transducer is laterally translated in x-direction in discrete motion at each vertical sample position. b) Example phantom imaging of gelatine beads filled with GFP with raster-scanning optoacoustic mesoscopy in the hybrid system. The image size corresponds to 4 × 4 mm.

Future advances can however push the raster-scanning abilities of the hybrid system by implementing higher-frequency detectors. Furthermore, the sample can be rotated in all directions, thus allowing the implementation of multi orientation raster-scanning optoacoustic mesoscopy as has been demonstrated in [22]. The acquisition speed of the system can also be enhanced by pushing the scanning approach towards continuous motion. This can then be an interesting implementation for imaging of biological samples labeled with reversibly switchable fluorescent proteins, which allow to boost the CNR up to a factor of 50 [26, 27].

Likewise, this raster-scanning geometry can also be used for pure ultrasound imaging, based on the reflection of emitted ultrasound waves from the transducer. By using a pulser (5077PR, Olympus NDT, Germany), the transducer can emit ultrasonic waves in a predefined frequency range and detect the reflections as in any conventional ultrasound imaging system.

4.6 Conclusion

This chapter describes the implementation of single-element transducers into the hybrid MSOT - SPIM system. First, the sensitivity of multiple transducers is compared. These measurements reveal the poor sensitivity of the detector array and the need for implementing larger and more sensitive single-element detectors. Consequently, highly sensitive single-element detector were implemented into the system and a novel spiral scanning geometry was introduced. This spiral scanning geometry is based on the broad NA of the single-element transducers, which allows to detect OA signals from over the full sample width while the sample is rotated and vertically translated in front of the detector. Subsequently, technical aspects of the implementation of spherically focused single-element detectors are discussed and the system is thoroughly characterized in terms of noise, resolution, imaging depth and contrast. The abilities of the novel system implementation are demonstrated by imaging of transgenic zebrafish. Results show that the spiral optoacoustic tomography modality in the hybrid system is able to image genetically labeled fluorescent proteins such as GFP deep in developmental organisms, which may lead to promising biological applications in future.

5 Development of a hybrid absorption-optoacoustic spectrometer

5.1 Introduction

As described in detail in chapter 4, a strong SNR of the optoacoustic time transients is crucial to obtain a good CNR for optoacoustic imaging. The sensitivity of the detector plays a critical role for the ability of any OA imaging system to be able to measure exogenous contrast (especially labeled fluorescent proteins) in biological samples. However, another way of improving the CNR of exogenous contrast in OA imaging is the use of reversibly switchable fluorescent proteins for genetic labeling of the samples. As shown by Yao et al., final CNR improvements of up to 50 times can be achieved in depths of 10 mm using Bacterial Phytochrome (BphP1) [26]. Further studies could confirm the strong gain in CNR by using rsFPs for OA imaging [26, 161–164]. The basic switching concept of rsFPs is characterized by the change of either the absorbance spectrum or the QY when illuminated at specific wavelength close to the absorption maximum. This effect has strongly been exploited by super-resolution techniques (nanoscopy) in super-resolution techniques based on stochastic (photoactivation localization microscopy / stochastic optical reconstruction microscopy) and deterministic switching (stimulated emission depletion microscopy / reversible saturable/switchable optically linear fluorescence transition microscopy) [165].

The essential optical characteristics of rsFPs in fluorescence imaging have already been well described in [166]. This characterization includes absorbance spectroscopy, switching kinetics and photobleaching under CW illumination used in fluorescence imaging. However, the essential characteristics of rsFPs in optoacoustic imaging under typical OA imaging conditions using pulsed illumination are still unknown. This is basically due to the high pulse energies used in OA imaging and the relative long pauses in the millisecond range between illuminating pulses, so that

dark-relaxation cannot be neglected anymore. For this reason, a hybrid optical-optoacoustic spectrometer based on the nanosecond excitation pulses emitted from the OPO-laser described in chapter 3 was developed and its applicability was demonstrated by a profound characterization of the rsFPs in optoacoustics. This is particularly important to enable the use and to facilitate the choice of rsFPs for OA imaging applications. Findings presented in this chapter and the underlying technology were published by Vetschera et al. [27].

Optoacoustic spectroscopy

Optoacoustic (photoacoustic) spectroscopy goes back to 1930ies, when gases were firstly analyzed applying the method [167]. However, the insufficient technological facilitities at the time in terms of pulsed illumination and ultrasound detection have hindered progress for decades [116]. Only in the 1970ies, Allan Rosencwaig firstly published an experimental setup for a photoacoustic spectrometer demonstrating the OA spectrum on the proteins cytochrome c and hemoglobin, which exhibit strong absorption peaks in the visible range [168]. The following years shed more light on the possible applications of optoacoustic spectroscopy in various scientific areas including bulk studies (including biological applications), surface studies and de-excitation studies [169] and the theoretical background [170] of the spectroscopic measurements. Due to the technological standards at the time, the illumination of first OA spectroscopy measurements was based on a high-pressure Xe lamp, a monochromator and a chopper [168], which limits the pulse length and consequently the acoustic frequency spectrum of the emitted sound waves as well as the repetition rate of the data acquisition. More recently, published OA spectroscopy systems in the visible range are based on OPO lasers emitting nanosecond pulses and providing repetition rates up to 100 Hz. The application and use of such systems has thoroughly been demonstrated by characterizing chromoproteins and fluorescent proteins [171] for OA imaging. Standard fluorescent proteins have great potential as genetic labels for deep in-vivo OA imaging, however they usually exhibit a low PGE, thus the imaging contrast of these OA labels is relatively weak compared to strong endogenous absorbers like hemoglobin and melanin. RsFPs have the potential to overcome this limitation by using temporal unmixing schemes which allows to distinguish between the time-dependent labeled contrast and the constant background signals of non-switching absorbers.

The fundamental principle of rsFPs is based on reversible switching between

metastable electron states in the proteins by illumination at specific wavelengths. The electron states can be distinguished between chromophore planarity, stability and protonation [27]. These parameters define the absorption and emission spectra of the proteins. RsFPs can be classified in two groups: Photochromic rsFPs which change in absorption spectra and rsFPs with a change in quantum yield.
The use of rsFPs for optoacoustic imaging is challenging, due to the protein's varying kinetics which is characterized by the switching half life time. This half life time strongly depends on the light fluence, the illumination power and the repetition rate of the illuminating laser pulses - thus any optoacoustic imaging system measuring rsFPs needs to be adapted in these terms for the optimal usage of the proteins.

5.2 Methods

In order to study the characteristics of the most common rsFPs, a custom made hybrid absorption - OA spectrometer has been developed to investigate the characteristics of rsFPs for optoacoustic imaging. The OA modality of the apparatus is based on the nanosecond laser pulses emitted from an OPO laser, sample excitation of the protein in a microfluidic chip and acoustic detection by an ultrasonic transducer. The absorption measurements by this system are based on a fiber-coupled broadband white light illumination and subsequent detection of the transmitted signal by a commercial spectrometer. Figure 5.1 illustrates the scheme of the setup.

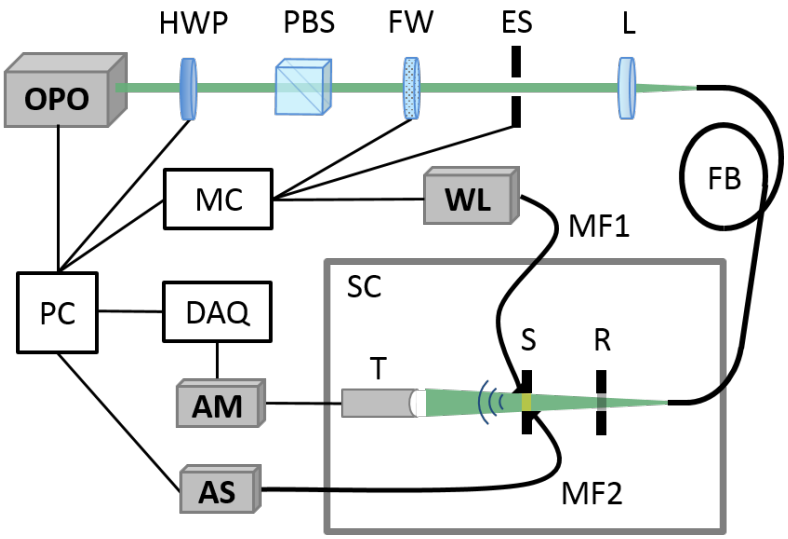

Figure 5.1: Scheme of the hybrid absorption-optoacoustic spectrometer setup: OPO: Optical Parametric Oscillator, HWP, Half-wave plate, PBS: Polarizing beam splitter, FW: Filter wheel, ES: Electronic shutter, L: Lens, FB: Fiber bundle, WL: Whitelight lamp, MF: Multimode fiber, AS: Absorption spectrometer, SC: Sample chamber, R: Reference chip, S: Sample chip, T: Transducer, AM: Amplifier, DAQ: Data acquisition card, MC: Microcontroller, PC: Personal Computer.

5.2.1 Optoacoustic spectroscopy methods

Nanosecond laser pulses at a repetition rate of 50 Hz are generated by the same OPO laser (Spitlight-DPSS 250 ZHG-OPO, Innolas, Germany) as for the hybrid SPIM-OA system described in chapter 3, which covers a wavelength range from 420-2100 nm. In this setup, due to optical attenuation of the available components (half-wave plate, polarizing beam splitter) and the choice of the proteins in this study, only the wavelength range from 420 to 800 nm is covered. However, the energy per pulse spectrum of the OPO laser is not constant over the whole wavelength range which is critical for accurate OA spectroscopy. Thus, a HWP in a motorized rotation stage (PRM1Z8, Thorlabs, Germany), a PBS and a lookup table are used to ensure the constant laser pulse energies over the whole illumination spectrum. The lookup table was created before any OA spectroscopy measurement by measuring the laser pulse energy for the whole wavelength range and at each relevant rotation angle of the half-wave plate with a powermeter (Vega, Ophir, Israel) at the output of the fiber. Figure 5.2 shows the measured pulse energies for wavelengths from 420 to 800 nm as a function of the rotation angle of the motorized half-wave plate.

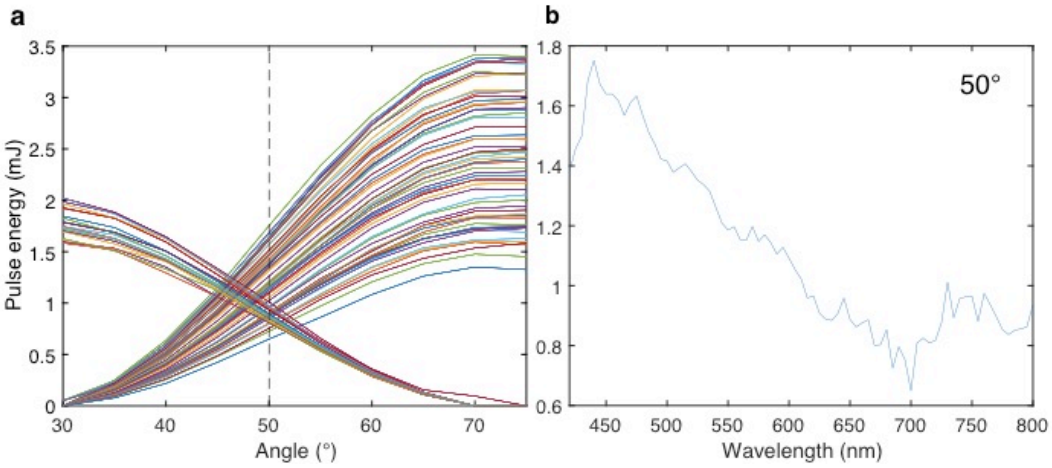

Figure 5.2: Laser pulse energy modulation based on the lookup table. a) Pulse energy at the output of the fiber as a function of the rotation angle of the motorized half-wave plate. Each sinusoidal function corresponds to a certain wavelength, wavelengths < 710 nm reveal an increasing power with increasing rotation angle, wavelengths $\geqslant 710$ nm show decreasing power with increasing angle of the half-wave plate due to the 45° rotation of the polarizing beam splitter at the output of the laser. The dashed line indicates the pulse energies at an angular position of 50° used in panel b), which shows the the pulse energies as function of wavelength.

The resolution for wavelengths and rotation angles was 5 nm and 5° respectively. As can be seen in figure 5.2 b), the laser pulse energy increases up to ~ 450 nm and then decreases linearly up to 710 nm at a fixed polarization of the half-wave plate. At 710 nm, the polarizing cube at the output of the laser is rotated by 45° and consequently allows near-infrared photons to be emitted from the OPO. The automatic switching of the polarizing cube at the laser output is controlled by a stepper-motor and a microcontroller (Arduino Uno, USA). Furthermore, the micro-controller also switches the filter wheel from a visible to a near-infrared bandpass filter, so that the visible fraction of the laser pulses at wavelengths $>$ 710 nm are blocked. This is equally applied to wavelengths below 710 nm, where the near-infrared share of the pulses is blocked by the electronic filter wheel. At wavelengths > 710 nm, the output pulse energies slightly increase up to 750 nm and remain approximately constant at wavelengths over 750 nm. Based on the recorded laser pulse energy data, the lookup table is calculated by fitting sinusoids to the recorded values. The fitted lookup table consequently enables to find the respective rotation angle of the rotation stage for a chosen pulse energy at each wavelength. In this work, pulse energies of ~ 1.3 mJ are used at the output of the fiber for sample illumination. Figure 5.3 shows the resulting pulse energy spectrum using the lookup table at the output of the fiber and the initial pulse energy spectrum at

the output of the OPO.

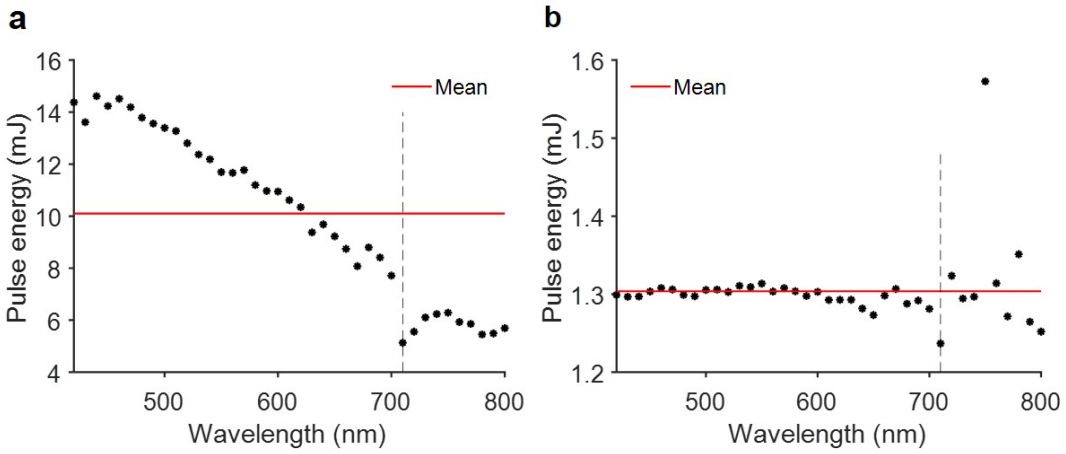

Figure 5.3: Pulse energy spectrum of the OPO laser. a) Uncorrected spectrum of the laser output pulse energy. The red line denotes the mean over the whole spectrum, the dashed line corresponds to the switching of the polarizer cube for signal and idler photons. b) Flat power spectrum measured at the fiber output using the power control based on the HWP, the PBS and a lookup table. The red line in both panels denotes the mean pulse energy over the whole spectrum. The dashed line corresponds to the transition wavelength from the visible to the NIR range, when the polarizing cube at the output of the laser is rotated by 45° for emitting signal or idler photons.

An electronic shutter (SHB1, Thorlabs, Germany) controls the beam propagation, so that the laser illumination can be blocked when absorption measurements with the broadband whitelight lamp and the optical spectrometer are performed. Consequently, pulses are coupled into a multimode fiber bundle (CeramOptec, Germany) consisting of 430 fused multimode fibers of 200 μm diameter via a broadband spherical lens (focal length of 125 mm).

Samples for the OA spectroscopy measurements are diluted and injected into a microfluidic chip (µ-Slide I 0.2 Luer, hydrophobic, uncoated, Ibidi, Germany) with a diameter of 200 μm. Thus, the generated optoacoustic frequencies are within a suitable frequency range for the low-frequency single-element detector (V382-SU, 3.5 MHz, Olympus, Germany) with a central frequency of 3.5 MHz. Reference OA signals are generated by the illumination of a second microfluidic chip filled with Indian ink which is placed in between the fiber output and the sample itself (figure 5.1). The optoacoustic signals measured by the transducer are amplified by 60 dB using a wideband voltage amplifier (DHPVA-100, Femto, Germany) and digitized with a 12 bit data acquisition card (RZE-002-400, Gage, USA) at 100 MS/s. Figure

5.4 a shows a typical time transient of the fluorescent protein hcRed and Indian ink as reference. Figure 5.4 b) shows the respective frequency spectrum of the sample and the reference.

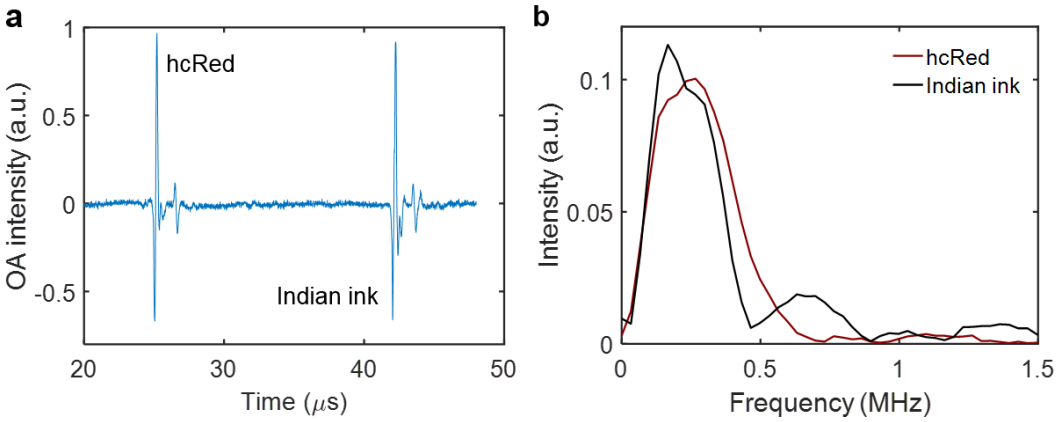

Figure 5.4: Typical OA signals (10 averages) of hcRed and Indian ink acquired with the spectrometer in time and frequency domain: a) Time transient of the OA signals generated by hcRed at 575 nm illumination and the corresponding OA reference signal generated by Indian ink. b) Frequency domain spectrum of the OA signals generated by hcRed (red) and Indian ink (black).

Optoacoustic signals were measured over 10 pulses at each wavelength and subsequently the signals of the sample and the reference were separated in time (see Figure 5.4). The peak-to-peak values for sample signals were subsequently divided by the normalized corresponding reference signal to correct for laser pulse deviations. In order to remove the residual noise, the minimum of the uncorrected optoacoustic spectrum was subtracted.

To demonstrate the importance of the power control based on the half-wave plate and the polarizing beam splitter and the pulse-to-pulse correction using Indian ink as a reference compound, OA spectra of the fluorescent protein hcRed were measured with and without corrections. The absorption peak of hcRed is at around 600 nm, a wavelength range where the laser pulse energy has a steep slope in contrast to wavelengths below 500 nm (see figure 5.3). Absorption spectra for the protein were measured beforehand using a commercial spectrometer (UV-1800 spectrophotometer, Shimadzu, Japan) with a better resolution than the fiber-coupled spectrometer used in the hybrid system. As can be seen in Figure 5.5, both correction methods strongly improve the spectra quality toward the shape of the absorption spectrum. This can be quantified by the correlation coefficient (r^2) between the OA and the absorption spectrum, resulting in a gain in correlation r^2

of $\sim$ 3 % for each correction alone and $\sim$ 3.5 % for both methods combined.

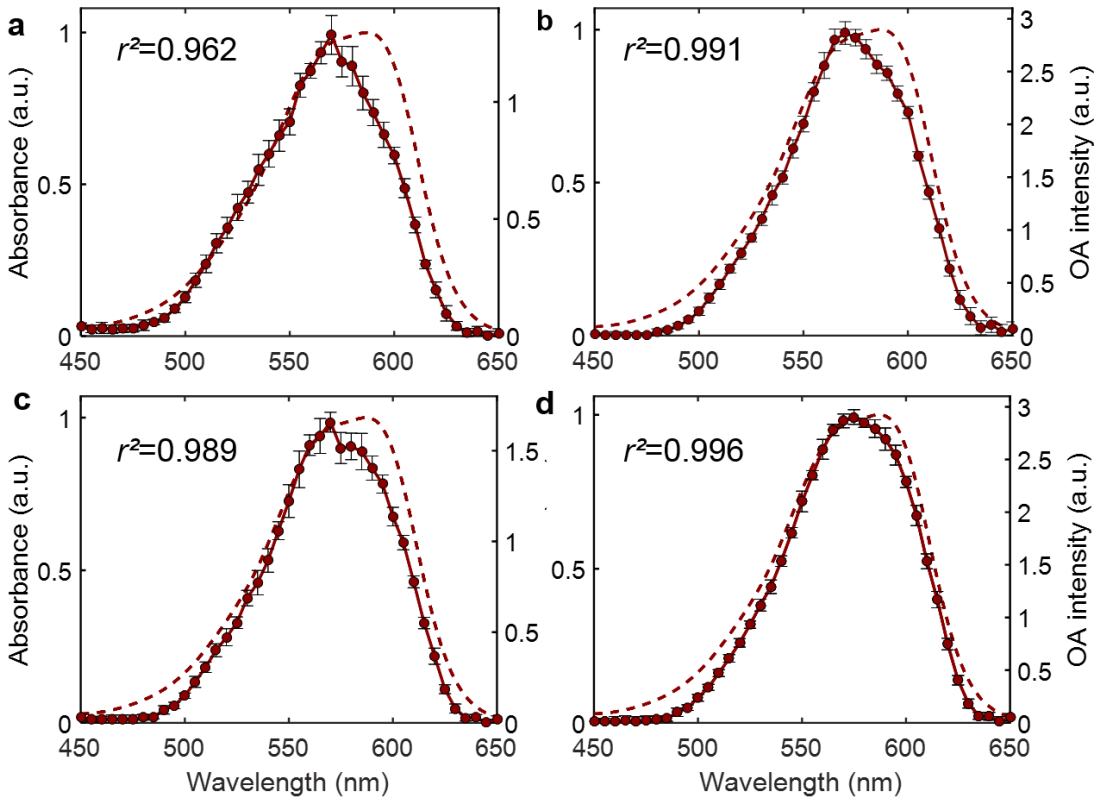

Figure 5.5: Effects of spectral pulse energy correction and pulse-to-pulse energy correction on the optoacoustic spectra (solid) of hcRed. The spectral energy correction is performed by keeping the pulse energy stable at $\sim$ 1.3mJ using the motorized HWP, the PBS and the lookup table. The pulse-to-pulse energy correction is based on the OA reference signals generated by Indian ink. The dashed line shows the respective absorbance spectrum of hcRed. a) No spectral energy correction, no pulse-to-pulse correction, b) no spectral energy correction, pulse-to-pulse correction, c) spectral energy correction, no pulse-to-pulse correction, d) spectral pulse energy correction, pulse-to-pulse correction. r^2 denotes the correlation coefficient of the optoacoustic and the absorbance spectra.

Another critical aspect of OA spectroscopy experiments is thermal stability over time, since a temperature increase due to the energy deposition by the laser would lead to an increased speed of sound and consequently to increased OA signal generation. However, profound analysis of the peak pulse distance from the transducer to the sample does not reveal any drift during experiment with our system (figure 5.6 b). Furthermore, monitoring the measurement with a highly sensitive NIR camera (FLIR E60, FLIR Systems GmbH, Germany) with a sensitivity of < 0.05°C) did not show any temperature increase during the experiment (see figure 5.6 c).

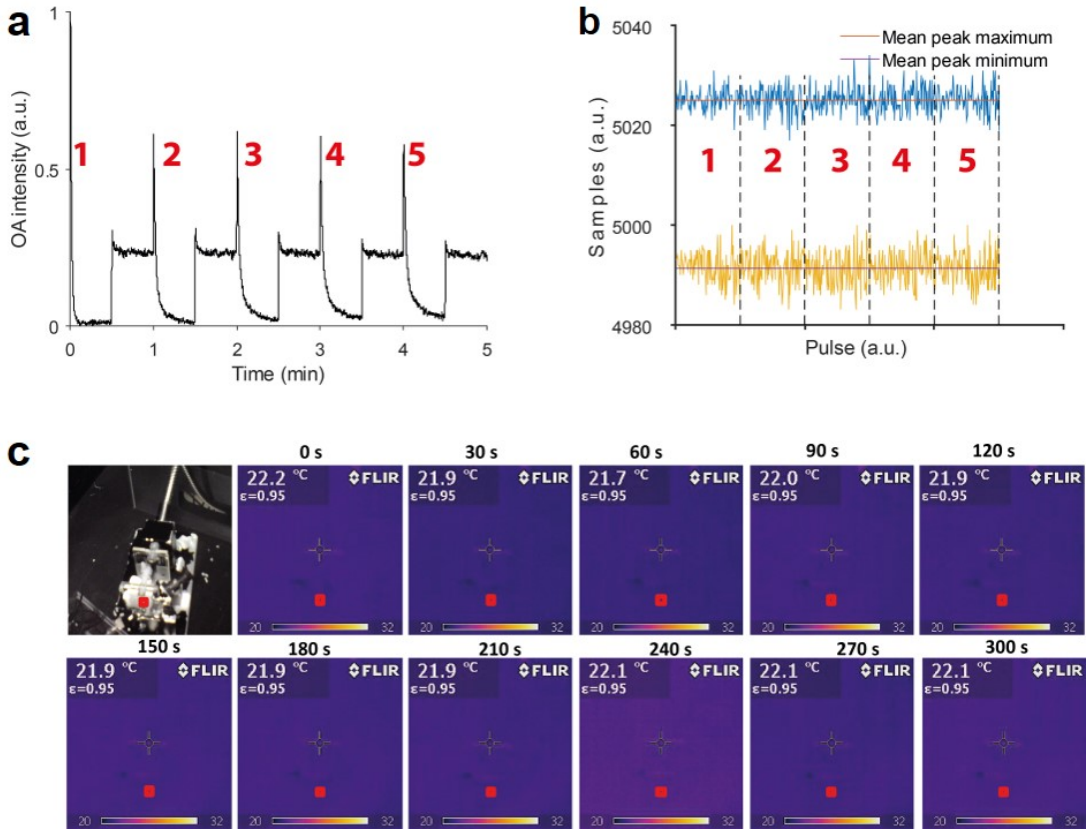

Figure 5.6: Temperature monitoring during a 5 min OA kinetics measurement of Dronpa-M159T. a) OA signal during cycled illumination with illumination 488 and 420 nm. b) Respective sampling position of the maximum and minimum of the OA signals for the first 100 pulses of each of the 5 cycles recorded in the experiment shown in a). The sampling rate for this measurement was increased to 200 MS/s, which corresponds to the maximum sampling rate of the DAQ card. c) Temperature of the sample chip during the experiments shown in a), the red square indicates the ROI where the temperature was precisely measured with the near-infrared camera.

Reference compounds

The use of Indian ink as source of reference signals is justified by its broad absorption spectrum, the high absorption coefficient, low photobleaching and OA linearity for the laser energies used in the project. Figure 5.7 shows the linearity and bleaching of Indian ink compared to other linear reference compounds known from literature [172].

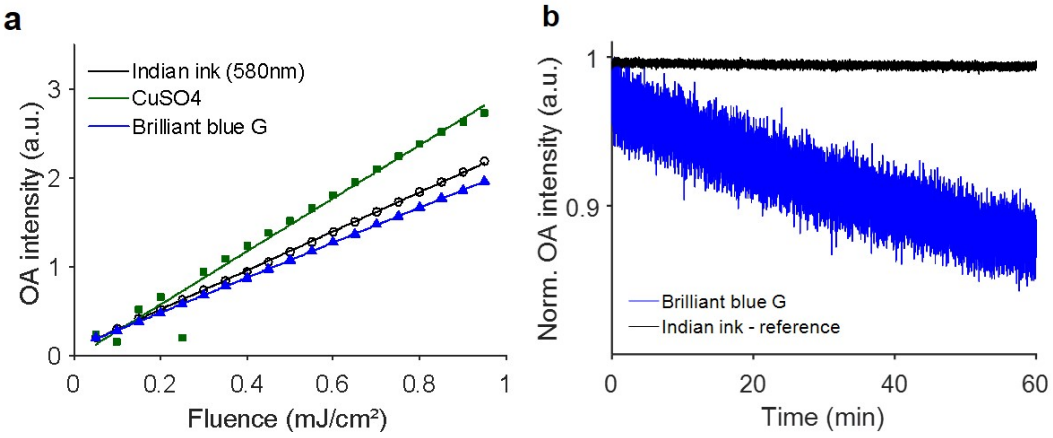

Figure 5.7: Linearity and bleaching of Indian ink compared to other reference compounds. a) Linearity of Copper sulfate ($CuSO_4$, Indian ink and Brilliant Blue G. b) Bleaching of Indian ink and Brilliant Blue G illuminated at 580 nm and pulse energies of 1.3 mJ.

However, the OA signals generated by Indian ink at high pulse energies ($\geq$ 100 mJ /pulse) are prone to create anomalous photoacoustic effects based on chemical reactions involving heat in the sample chamber [173]. To make sure that this effect based on particle size and deposited heat does not affect the linearity of the reference Indian ink in the hybrid OA-absorption system, the linearity of various ink particles was tested (see figure 5.8). The data shows that linearity can be assumed for all concentrations, particles sizes and over the whole fluence range used for measurements in the hybrid spectrometer. Nevertheless, the size of the particles has an influence on the OA signal strength and thus needs to be constant over the whole timeframe of the measurements.

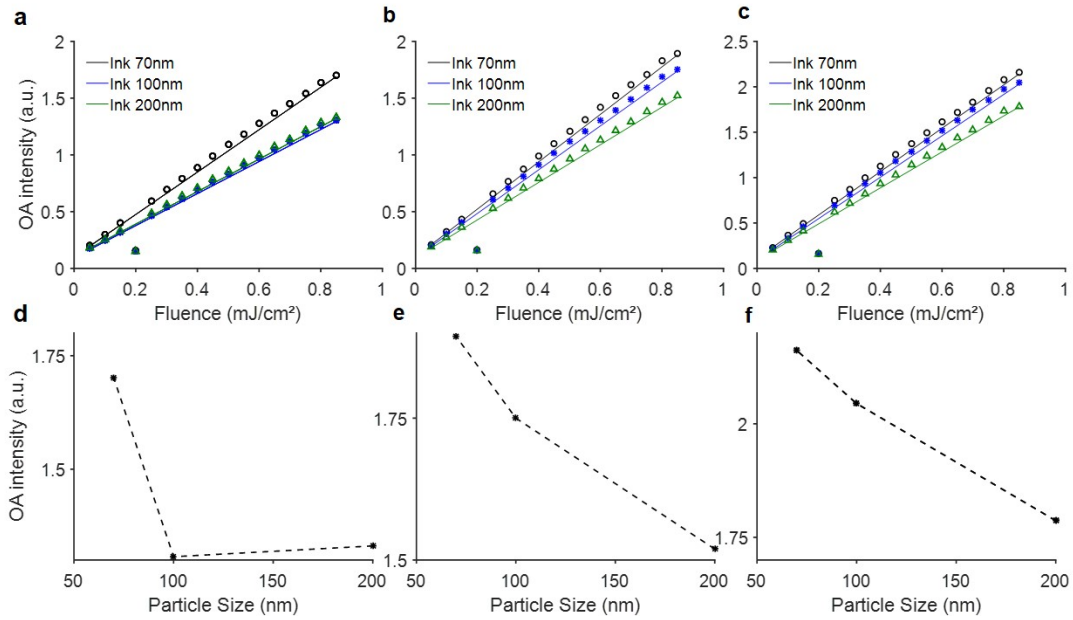

Figure 5.8: Linearity of Indian ink at three different concentrations and particle sizes.

5.2.2 Absorption spectroscopy methods

The absorption spectra were acquired after each excitation wavelength by interrupting the laser illumination with the electronic shutter, which is controlled by receiving TTL signals from the micro-controller (Arduino Uno, USA). The same micro-controller opens the shutter of the fiber-coupled broadband white light illumination source (DH-2000, Ocean Optics, Germany) which combines the light of a halogen and a deuterium lamp. Each recording is averaged over 20 acquisitions at an exposure time of $\sim$ 10 ms. The measured transmission spectrum is consequently divided by a reference spectrum and subsequently subtracted from a vector of ones. This reference spectrum was recorded in exactly the same microfluidic chip filled with phosphate buffered saline. This procedure is necessary since every chip has a slightly different intrinsic absorbance and thus different chips would alter the absorption spectrum of the sample. Absorbance spectra were averaged over 5 nm for representing the same spectral resolution as the OA spectra. Furthermore, shifts of the baseline introduced by fluctuations of the whitelight lamp are corrected by shifting the spectrum to zero.

5.3 Characterization of reversibly switchable fluorescent proteins (rsFPs)

The large application range of the hybrid spectrometer is firstly demonstrated by the characterization of a representative selection of rsFPs in optoacoustics. The rsFPs in this study are widely used in nanoscopy, table 5.1 shows the rsFPs taken into account for this study and their respective optical properties for nanoscopic applications.

rsFP	**Absorption maximum (nm)**	**Emission maximum (nm)**	**Quantum yield**	**M. absorption coefficient. ($M^{-1} \cdot cm^{-1}$)**
Dronpa[a]	503 / 390[a]	518[a]	0 .85[a], 0.67[k]	95,000[a]
rsFastLime[b]	496[b] / ∼ 390	518[b]	0.77[b], 0.60[d]	39,094[b], 46,000[d]
Dronpa-M159T[b]	489[b] / ∼ 390	515[b]	0.23[b], 0.33[c], 0.28[k]	61,732[b], 56,000[k]
Padron[d]	503 / 396[d]	522[a]	0.64[d]	43,000[d]
rsEGFP2[e]	478 / 408[e]	503[e]	0.3[e]	61,300[e]
rsCherry[f]	572[f] / ∼ 405	610[f]	0.02[j]	80,000[j]
rsCherryRev[f]	572[f] / ∼ 405	608[f]	0.0051[j]	42,300[j], 84,000[k]
rsCherryRev1.4[g]	572 / 450[g]	609[g]		
rsTagRFP[h]	565 / 440[h]	585[h]	0.11[h]	36,800[h]
BphP1[i]	756 / 678[i]	n.a.[i]	n.a.[i]	78,300[i]

a) Ando R., Science, 2004 [174]
b) Stiel A.C., Biochem. J., 2007 [175]
c) Ando R., Biophys. J., 2007 [176]
d) Andresen M., Nat. Biotechnol., 2008 [166]
e) Grotjohann T., eLIFE, 2012 [177]
f) Stiel A.C., Biophys. J., 2008 [178]
g) Lavoie-Cardinal F., ChemPhysChem, 2014 [179]
h) Subach F.V., Chemistry & Biology, 2010 [180]
i) Yao J., Nat. Methods., 2015 [26]
j) Shcherbakova D.M., Annu. Rev. Biophys., 2014 [181]
k) Zhou, X.X., Curr. Opin. in Chem. Biol., 2013 [182]

Table 5.1: Optical absorption properties of the rsFPs investigated in this study.

This study focuses on the green GFP derivatives (Dronpa, Dronpa-M1559T, Padron, rsEGFP2, rsFastLime) because of their different switching kinetics while exhibiting a similar absorption spectrum. The switching characteristics of these rsFPs under continuous illumination for fluorescence application have already been studied extensively [166, 174, 178], details can be found in table 5.2.

5.3.1 Spectroscopic characterization of rsFPs

Generally, rsFPs with a low QY are more suitable for OA applications since they exhibit a higher level of non-radiative de-excitiation that leads to stronger OA signals. This can be quantified by the PGE. Figure 5.9 illustrates the switching schemes with pulsed illumination used in this study:

rsFP	switching mode	equilibrium state fluorescence	switch-on $t_{1/2on}$ (s)	switch-off $t_{1/2off}$ (s)	dark relaxation $t_{1/2}$ (s)
Dronpa[b,d]	negative	100 %[d]	0.1[b], 0.12[d]	263[b], 115[d]	50,400[b]
rsFastLime[b,d]	negative	93 %[d]	0.11[b], 0.03[d]	5[b], 2.6[d]	480[b]
Dronpa-M159T[b]	negative	~100 %	0.05	0.23	30
Padron[d]	positive	5 %	5.6	0.06	9000
rsEGFP2[e]	negative	~100 %		0.0005	
rsCherry[f]	positive	32 %	3	0.05	40
rsCherryRev[f]	negative	8 %	0.05	0.7	13
rsCherryRev1.4[g]	negative	~8 %			
rsTagRFP[h]	negative	33 %	0.0028	0.18	~3300
BphP1[i]	negative	n.a.			

a) Ando R., Science, 2004 [174]
b) Stiel A.C., Biochem. J., 2007 [175]
c) Ando R., Biophys. J., 2007 [176]
d) Andresen M., Nat. Biotechnol., 2008 [166]
e) Grotjohann T., eLIFE, 2012 [177]
f) Stiel A.C., Biophys. J., 2008 [178]
g) Lavoie-Cardinal F., ChemPhysChem, 2014 [179]
h) Subach F.V., Chemistry & Biology, 2010 [180]
i) Yao J., Nat. Methods., 2015 [26]
j) Shcherbakova D.M., Annu. Rev. Biophys., 2014 [181]
k) Zhou, X.X., Curr. Opin. in Chem. Biol., 2013 [182]

Table 5.2: Switching properties of rsFPs under continuous illumination (i.e. for fluorescence excitation) illumination (only values from one source are comparable) of the rsFPs investigated in this study.

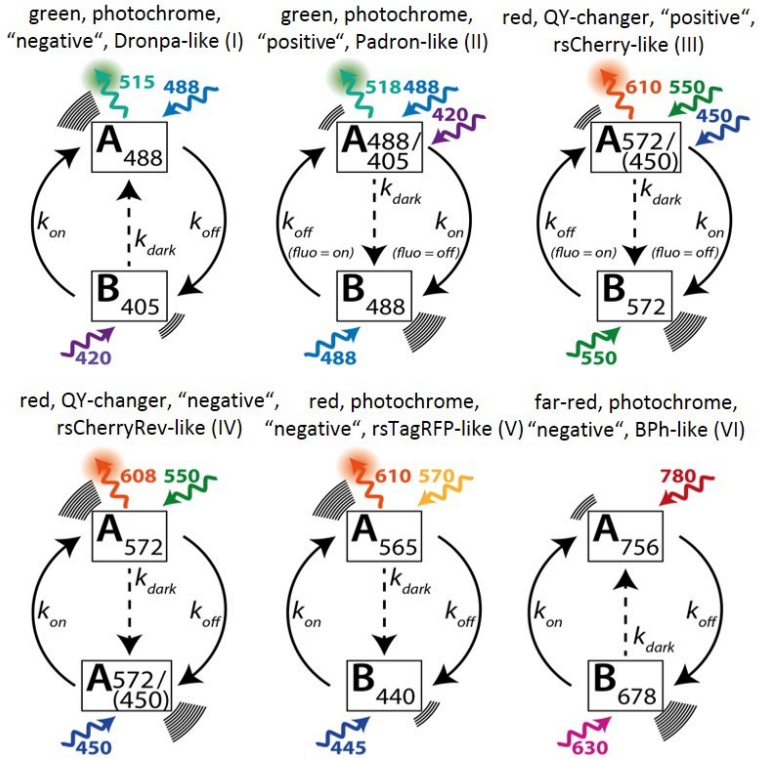

Figure 5.9: Illumination switching schemes used in this study on rsFPs. Curly arrows illustrate light excitation and fluorescence emission at the corresponding wavelengths. The fluorescence emission wavelength corresponds to the mean fluorescence emission wavelength of all proteins in the respective group. Curved lines represent the generated ultrasound waves, the number of lines indicates the relative emission amplitude. Switching states A and B are represented with their respective absorption maximum (the most prevalent absorption maximum is given for classes with several members). The large round arrows illustrate state transitions, dashed arrows denote dark state relaxation. For switching type II and III, the switching directions in are reversed in fluorescence and optoacoustic imaging.

To ensure maximum switching, illuminating wavelengths were selected to be as close as possible to the respective peak absorption of the protein. However, the wavelength range of the OPO laser (420-2100 nm) was a limiting factor for the ON-switching of the Dronpa-and Padron-like proteins, which exhibit the OFF-peak usually at around 400 nm.

As a first step for the spectroscopic characterization, hybrid OA-absorption spectra of the rsFPs were recorded (see figure 5.10). The correlation of the optoacoustic and the absorption spectra is above 94% for all rsFPs recorded, except for Dronpa which exhibts a very high QY and thus a low PGE. The PGE for the peak maxima of each protein can directly be extracted from the data. Table 5.3 shows the photoacoustic generation efficiency of the proteins relative to the OA standard CuSO4.

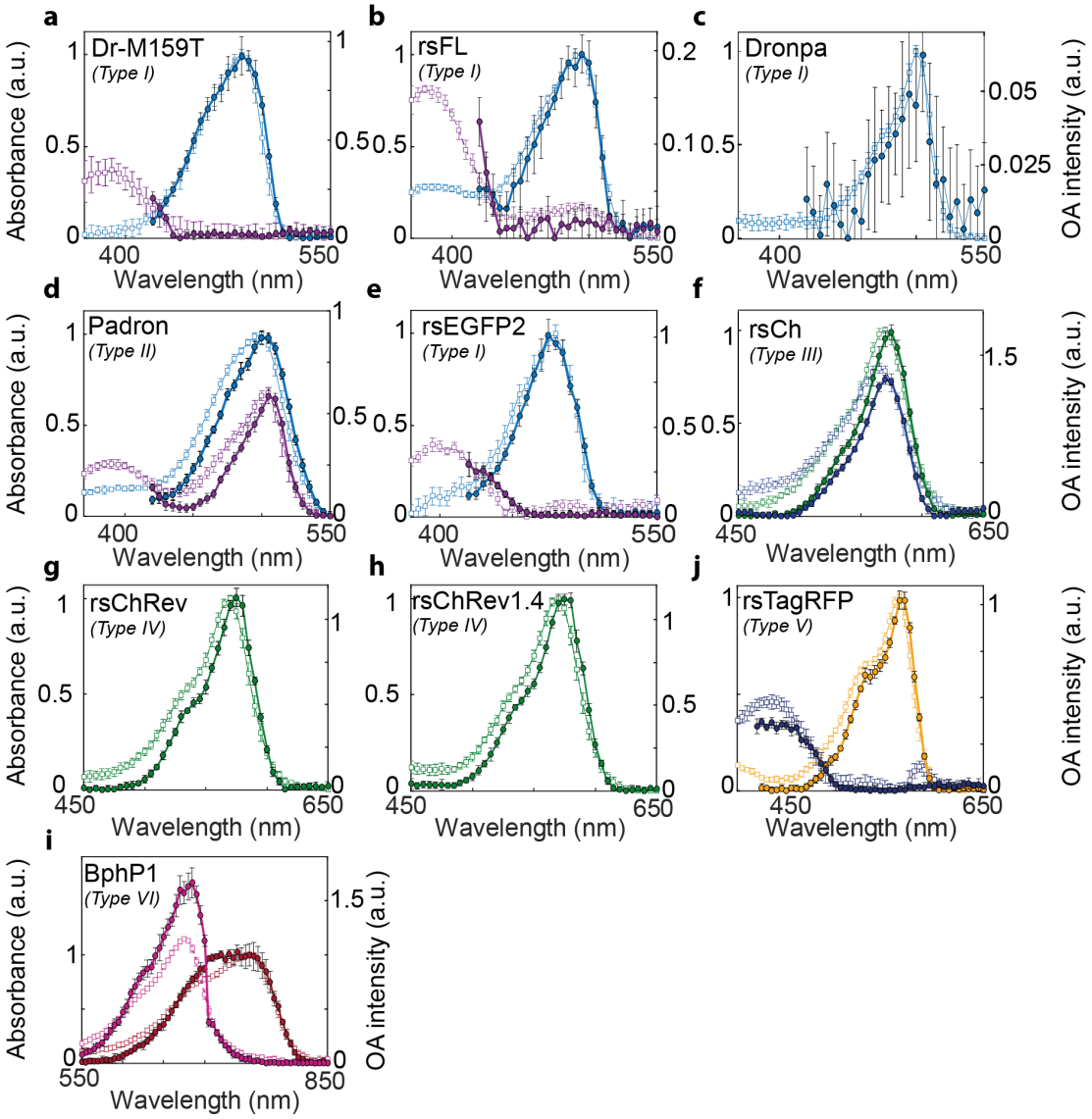

Figure 5.10: Optoacoustic (solid) and absorbance (thin / hollow) spectra of rsFPs in the ON and OFF states. Colors are chosen along the switching schemes in figure 5.9. Absorbance spectra are normalized to the OA equilibrium state. Type denotes the respective switching modes which are explained in figure 5.9. For Dronpa d), rsCherryRev g) and rsCherryRev1.4 h), switching was not detectable. Abbreviations: Dr = Dronpa, rsFL = rsFastlime, Ch = Cherry.

Generally, the PGE is inversely proportional to the QY, which results in a low PGE for Dronpa (<0.1) and high PGEs for rsCherry and Dronpa-M159T. Furthermore, photochromic rsFPs exhibit a high dynamic range that can be exploited for imaging applications [26, 163]. On the other hand, QY-changer rsFPs (especially those with a low QY) can only be exploited for infinitesimal OA signal changes. Moreover, the present switching state of the absorption and OA spectra can be better compared

when measured concomitantly. In figure 5.11, the absorption spectrum is obtained by concatenating of the averaged fractions of the absorption spectrum that has been illuminated by laser pulses at the respective wavelength directly before (e.g. 497.5-502.5 nm after illumination at 500 nm).

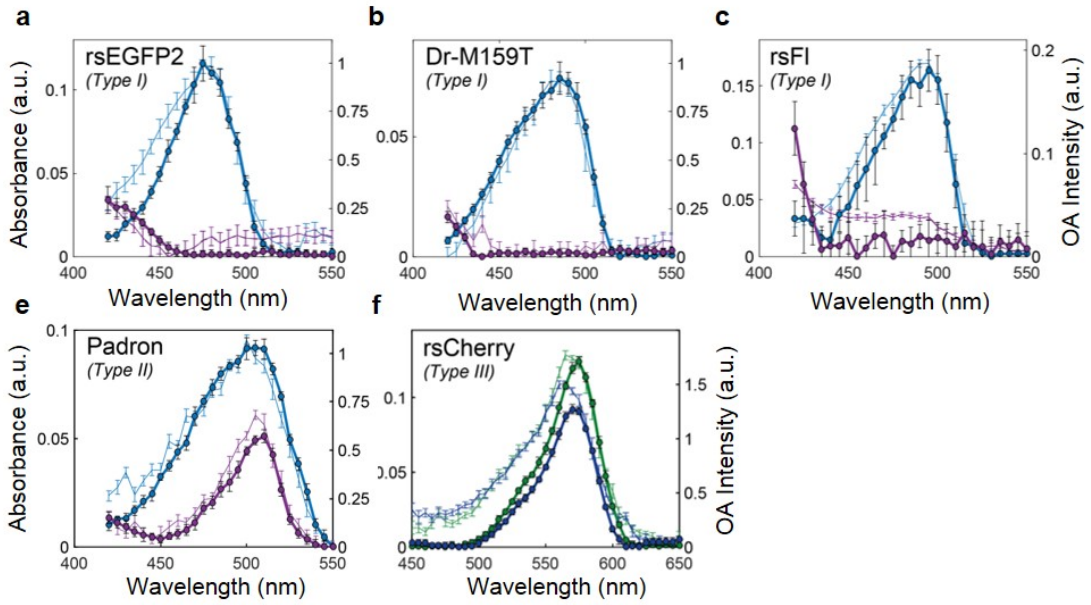

Figure 5.11: Concomitantly measured optoacoustic (solid) and absorbance (thin / hollow) spectra of selected rsFPs in the ON and OFF state. Colors are chosen along the switching schemes in Figure 5.9. Absorbance spectra are normalized to the OA equilibrium state. Type denotes the respective switching modes which are equally explained in figure 5.9.

5.3.2 Optoacoustic switching kinetics of rsFPs

In a next step, the switching behaviour of rsFPs under pulsed illumination conditions used in optoacoustics (7 ns pulse length, 1.3 mJ / per pulse, 50 Hz repetition rate) is investigated 5.12.

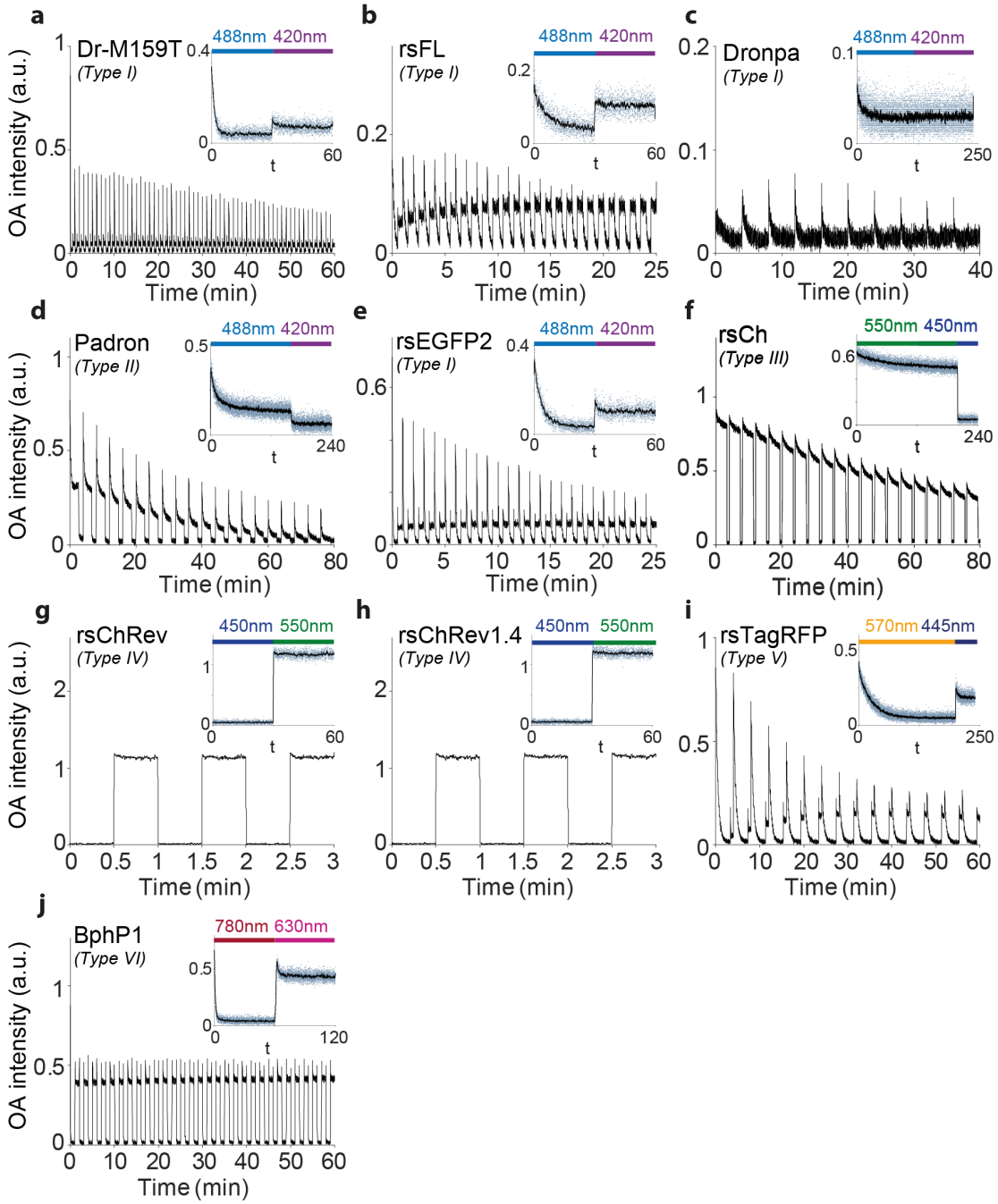

Figure 5.12: Optoacoutics switching kinetics of rsFPs in the ON and OFF state. Multiple cycles are presented to demonstrate photostability. Insets depict the central cycle of the respective switching trace, color bars denote the respective illumination wavelength. Abbreviations are defined as in figure 5.10.

A proper understanding of the switching kinetics is essential for any imaging application, since modulation and thus a gain in the image CNR can only be obtained with a reasonable illumination pattern. Figure 5.12 clearly shows the different switching speeds from slow (Dronpa) to fast (Dronpa-M159T) known

from fluorescence switching. In general, OA switching is much slower compared to fluorescence switching due to dark relaxation during two consecutive illumination pulses, which corresponds to ~ 20 ms at a repetition rate of 50 Hz. Measurements results on the OA switching speed, the dynamic range and OA photobleaching can be found in table 5.3, all data is extracted from the switching cycles shown in figure 5.12.

rsFP	$t_{1/2off}$ (s) switch-off	Dynamic range	PGE* in equilibrium state	PGE*	$t_{1/2}$ (min) photobleaching
Dronpa	19.78	0.57	0.03		
rsFastLime	5.81	0.68	0.06		29.18
Dronpa-M159T	0.64	0.89	0.68		55.35
Padron	4.99	0.61	0.62	0.49	36.27
rsEGFP2	1.78	0.88	0.46		16.54
rsCherry	16.49	0.28	0.74	0.69	63.68
rsCherryRev			0.47		
rsCherryRev1.4			0.46		
rsTagRFP	14.16	0.91	0.45		24.52
BphP1	0.65	0.90	0.31	0.53	

* relative to CuSO4

Table 5.3: Optoacoustic switching properties under pulsed illumination (1.3 mJ/pulse, 7 ns pulse length, 50 Hz repetition rate) of rsFPs measured with the hybrid spectrometer.

Figure 5.13 directly illustrates the photobleaching of the rsFPs, the data is directly taken from the peaks of each ON cycle presented in figure 5.12

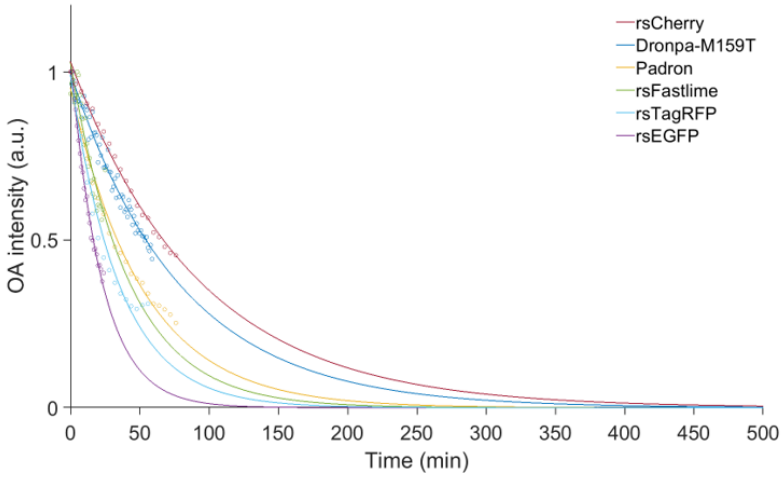

Figure 5.13: Photobleaching as a function of time for rsFPs. Dronpa is excluded due to low data quality, Bacterial Phytochrome does not reveal significant bleaching over one hour of illumination as shown in figure 5.12.

To investigate more on the effect of dark relaxation during two consecutive pulses,

measurements on switching cycles for Dronpa-M159T and rsEGFP2 were performed at multiple laser repetition rates from 10 to 50 Hz (see figure 5.14). Higher repetition rates result in decreasing switching half-life times $\mathbf{t_{1/2off}}$. For example, for Dronpa-M159T, the switching half-life time $\mathbf{t_{1/2off}}$ decreases from ~ 5 s to ~ 1 s by increasing the laser repetition rate from 10 to 50 Hz. Consequently, dark relaxation can be neglected for very high repetition lasers in the Megahertz regime.

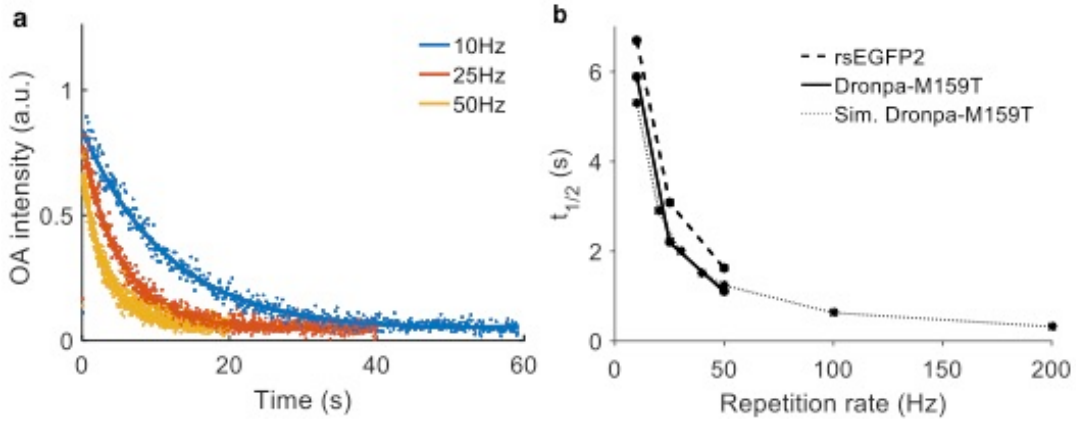

Figure 5.14: Dependence of the switching time of Dronpa-M159T and rsEGFP on the laser repetition rate. a) Switching cycles of Dronpa-M159T at repetition rates of 10, 25 and 50 Hz. b) Switching half-life times $\mathbf{t_{1/2off}}$ (s) of Dronpa-M159T, rsEGFP and simulated data for Dronpa-M159T at multiple repetition rates, the data for Dronpa-M159T and rsEGFP is extracted from a).

Additionally, the dependence of the OA switching half-life time on the illuminating pulse energy was validated. Figure 5.15 a) shows the switching cycles of Dronpa-M159T at multiple pulse energies, figure 5.15 b) illustrates the decreasing half-life times $\mathbf{t_{1/2off}}$ as a function of the pulse energy. As known from results in fluorescence imaging with CW illumination, $\mathbf{t_{1/2off}}$ decreases exponentially with increasing illumination pulse energy.

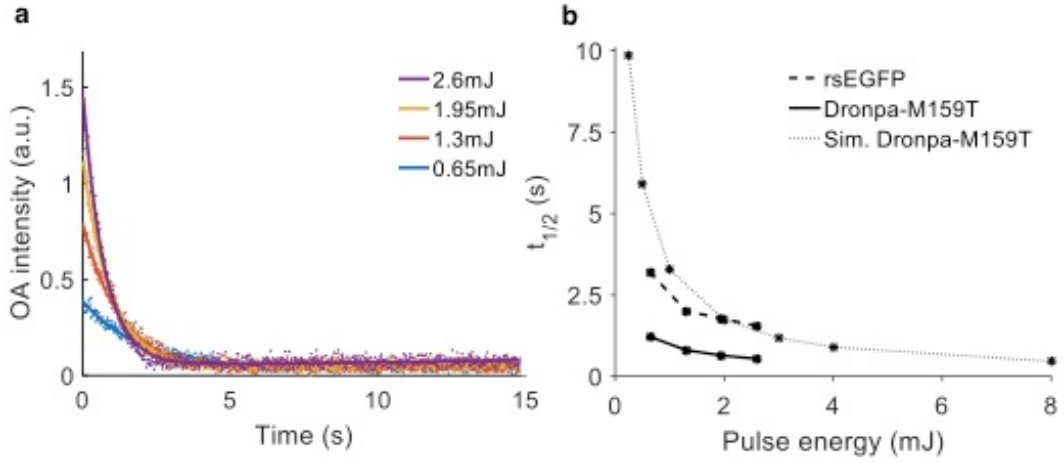

Figure 5.15: Dependence of the switching time of Dronpa-M159T and rsEGFP on the pulse energy. a) Switching cycles of Dronpa-M159T at four different pulse energies at 0.6, 1.3 1.95 and 2.6 mJ. b) Switching half-life times $\mathbf{t_{1/2off}}$ (s) of Dronpa-M159T, rsEGFP and simulated data for Dronpa-M159T at multiple pulse energies. The data for Dronpa-M159T and rsEGFP is extracted from a).

Furthermore, the pulse illumination repetition rate and the pulse length have an effect on the protein's photobleaching. For quantitative assessment, a custom-built, overdriven laser diode at 450 nm [183] was used to illuminate a cover slip with superfolder-GFP. The diode was triggered by a function generator (Rigol, Germany) allowing repetition rates of up to 50 MHz and consequently pulse lengths of 10 ns at a duty cycle of 50 %. For the experiments, repetition rates and pulse durations of 50 MHz / 10 ns, 5 MHz / 100 ns, 500 kHz / 1000 ns and CW illumination (using a duty cycle of 99.9 %) were chosen as well as a constant power of 500 μW. Constant power was ensured by measuring the power before the bleaching experiments for each repetition rate using a powermeter (PM100D, Thorlabs, Germany). The fluorescence signals were bandpass filtered and consequently measurerd with a photodiode (SPCM-AQRH-13, Excelitas, Canada). Digitization was performed over 300 s at an aquisition rate of 100 samples/s with a data acquisition card (PCIe-6353, National Instruments, USA). Overall, higher repetition rates result in faster bleaching compared to slower repetition rates in CW illumination (Figure 5.16). This can be explained by the multiphoton absorption of the protein which results in transitions to long-lived or higher-order singlet and triplet states [160].

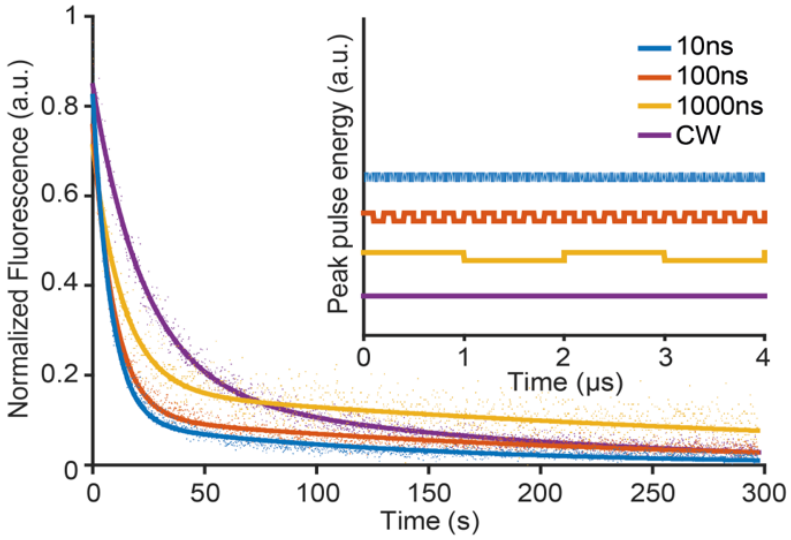

Figure 5.16: Photobleaching of superfolder-GFP (sfGFP) measured with a photodiode as a function of time for multiple illumination pulse lengths and illumination pulse repetition rates.

5.4 Further applications

5.4.1 Optoacoustic characterization of a calcium sensor

The developed optoacoustic spectrometer is an important tool that allows to characterize many other absorbers that are useful for optoacoustic imaging. For example, a Ca^{2+} sensor for photoacoustics (CaSPA), has been developed at our Institute, which allows to determine optoacoustic intensity changes that depend on the Ca^{2+} concentration [184]. Calcium is an important messenger in biological organism that controls processes e.g. in immune and neuronal cells as well as muscles. Thus, deep tissue, high-resolution *in vivo* imaging of these process can enable new insights in the understanding of the underlying physiological mechanisms. In contrast to optical imaging modalities, OA imaging provides the necessary imaging depth for sensing Ca^{2+} fluxes in deeper tissues layers. This section is based on a publication by Roberts et al. [184].

The optoacoustic spectrometer allows to quantify the OA signal intensity of the full extinction spectrum of CaSPA when unbound and bound to Ca^{2+} ions. At the absorption peak of 550 nm, the OA intensity decreases by a factor of ~ 2 when 39 μM of Ca^{2+} are added to the sensor. This strongly correlates ($r^2 = 0.99$) with both changes in the absorbance peak and the fluorescence emission peak at 634

nm respectively, when Ca^{2+} is added. With its low QY of 0.01, CaSPA is well designed for OA applications. Furthermore, CaSPA exhibits strong photostability at the peak absorbance (550 nm) over 5000 pulses revealing almost no loss in signal intensity during the time frame.
The promising photophysical characteristics of CaSPA in optoacoustics acquired with the optoacoustic spectrometer were the base for OA imaging experiments at the institute. Consequently, calcium fluxes in cells and heart organoids as well as in zebrafish brains could be measured with an OR-resolution OA microscope [156, 184]. These results demonstrate the potential of CaSPA for further discoveries of biological processes in deeper tissue layers.

5.4.2 Optoacoustic characterization of the site-directed mutagenesis of the phycobiliprotein smURFP

Another example of the broad application range of the OA spectrometer is the characterization of mutants of the phycobiliprotein smURFP. smURFP was the first protein engineered for fluorescence imaging [185]. It exhibits strong absorptivity, low photobleaching and a high quantum yield, thus it is also an interesting label for optical microscopy [186]. With its peak absorbance at 640 or 680 nm [187], its absorption spectrum is also in a wavelength range that is interesting for OA imaging. However, smURFP has so far only been optimized for fluorescence imaging, thus its PGE is relatively weak. Consequently, the cell engineering group our institute introduced mutations to the protein in order to decrease its QY and hence increase its PGE. The OA spectrometer was subsequently used to profoundly characterize the OA characteristics of wild-type smURFP and its mutants. Findings in this section are in the process of being published by Fuenzalida-Werner et al. [186], which also describes more details on the smURFP characterization.

Results show that the PGE of smURFP mutants that have been characterized so far can increase up to ~ 50 % compared to wild-type smURFP (for the mutant Y56L). Likewise, the mutated Y56L exhibits a red-shifted absorption peak from 645 to 675 nm. However, energy dissipates into other channels than fluorescence and non-radiative relaxation due to the decreased stabilization of the mutants. Thus, the PGE of Y56L is still lower than the one of the widespread and more red-shifted iRFP720. The remaining challenge in protein engineering is now to find a way to stabilize the proteins and still decrease the PGE and the red-shift. Broad screening of further mutations and consequent characterization with the OA spectrometer

might thus lead to further improvements for smurFP, so that the protein will be even more attractive as a label in OA imaging.

5.5 Conclusion

In this chapter a novel hybrid absorption-optoacoustic spectrometer based on an OPO laser was introduced that enables to measure both absorption and extinction spectra with high correlation. The usability and applicability of the system are demonstrated by a comprehensive characterization of a representative selection of reversibly switchable fluorescent proteins and other proteins designed for OA imaging such as mutants of the phycobiliprotein smURFP. The hybrid spectrometer also allows to gain important characteristics of the rsFPs such as the switching kinetics [27].

The characterization of the rsFPs allows to draw several conclusions for their use in OA imaging. First, photochromic rsFPs outperform QY changer due to their higher dynamic range in OA signal generation. Second, the switching kinetics of rsFPs under pulsed illumination as used in OA is slowed down compared to CW illumination due to dark relaxation during the laser pulses. However, this effect can be overcome by using lasers with high repetition rates. Moreover, the switching speed exponentially depends on the repetition rate and the laser power as well as photobleaching increases for higher repetition rates. Among the investigated rsFPs, Bacterial Phytochrome exhibits the best characteristics for OA imaging applications: a strong photoacoustic generation efficiency, a high dynamic range, fast switching kinetics and weak photobleaching. Additionally, the NIR excitation wavelengths used for switching BphP1 are highly suitable for OA imaging applications due the high penetration depth and strong absorption of hemoglobin at wavelengths greater than 700 nm. Nevertheless, also green rsFPs such as Dronpa-M159T are highly suitable for OA imaging applications, since BphP1 outperforms Dronpa-M159T only in terms of photobleaching. The switching kinetics shown in this chapter can be exploited for OA imaging in two different ways. Either by full switching and subsequent subtraction of the images in two states towards a differential image [26, 163, 164] or by signal modulation and lock-in detection in the frequency domain. This may be advantageous for imaging systems at high repetition rates ($>$ 400 kHz).

In summary, the hybrid absorption-optoacoustic spectrometer introduced in this chapter allows to characterize important properties of common optoacoustic labels in terms of PGE, spectral features, kinetics and photobleaching. The wide range of applications has been demonstrated by the characterization of rsFPs in optoacoustics, which may contribute to further boost the contrast in imaging with the hybrid SPIM - OA tomography system and other optoacoustic modalities.

6 Conclusion and outlook

For this thesis, a novel hybrid microscopy platform combining SPIM and MSOT was further advanced, in order to enable high-resolution imaging of biological development at penetration depths not accessible to purely optical methods. The thesis describes both SPIM and the OA tomography modality, it first gives an overview of the physical principles underlying optical and optoacoustic imaging in general. Technological aspects and system development are discussed, after which the thesis addresses the applications of the system in developmental biology and beyond. SPIM is an optical microscopy modality well suited for fast volumetric imaging of genetically labeled structures in young and transparent model organisms such as zebrafish. However, SPIM imaging becomes diffusive in older and thicker specimens due to scattering. The OA tomography modality allows the imaging optical absorbance deep within the samples without losing resolution because the generated ultrasound is only weakly scattered in tissue. Combining these two modalities enables tracking of development over longer timescales. SPIM is already a well-established tool in the biological sciences, and high-resolution OA tomography is fast emerging in basic and applied bioimaging as it is offering unique advantages over many other techniques.

In this work, the first implementation of optoacoustic tomography into the SPIM system was based on a high-frequency linear transducer array, which allowed the imaging of endogenous contrast such as blood, melanin and lipids deep in model organisms at resolutions up to 35 μm. The multispectral illumination at wavelengths in both the visible and the near-infrared range allowed spectral unmixing of these endogenous sources of contrast. Experimental results acquired with the array-based optoacoustic modality described in chapter 3 can reveal anatomical structures deep in zebrafish based on the absorption of light by melanin, oxygenized and de-oxygenized hemoglobin and lipid / water. However, due to the small size of the elements in the detector array, the sensitivity of the system was insufficient to detect OA signals of absorbers with a weak photoacoustic generation efficiency such as the fluorescent protein GFP, which is used as genetical label for specific

structures in zebrafish. Thus, the transducer array was replaced with a highly sensitive single-element detector covering a broad detection angle due to its high numerical aperture. A spiral scanning geometry was implemented to rotate and vertically translate the sample in front of the single-element detector and thereby ensure full-view detection for samples up to more than 10 mm in length. Due to the strong SNR of the modality based on single-element detectors, up to 8 wavelengths can be acquired without averaging during one single scan with the system. This novel spiral multispectral optoacoustic tomography approach allowed imaging of genetically labeled structures with fluorescent proteins such as GFP.

The second part of this thesis describes the work on another sample-based approach allowing to boost the contrast-to-noise ratio in optoacoustic imaging based on reversibly switchable FPs. These proteins have enabled tremendous advances in sub-diffraction microscopy [188, 189] and allow to enhance the contrast-to-noise ratio in optoacoustic imaging by a factor of 50 [26]. For this reason, a novel hybrid absorption-optoacoustic spectrometer was developed that was based on the same optical parametric oscillation laser as the hybrid microscope. The system enables the characterization of spectroscopic and switching properties and the photoacoustic generation efficiency of reversibly switchable FPs under pulsed illumination in optoacoustics. The knowledge gained in this research is an important step toward applying the proteins as genetic labels for optoacoustic imaging with the hybrid system and other optoacoustic imaging modalities.

6.1 Outlook

The hybrid SPIM- OA tomography system can be further improved in several domains. These firstly include technical aspects such as the image reconstruction, which still has potential for improvements by including the spatial sensitivity field. Furthermore, applying model-based algorithms has shown advantages in other optoacoustic tomography modalities, since these algorithms can take into account more specific system characteristics such as the transducer's geometry [116]. Due to the lower number of projections when using single-element detectors compared to linear arrays, applying model-based algorithms becomes computationally more feasible compared to the array-based OA tomography. To further increase the system sensitivity, novel ultrasound detectors can be tested which can be based on both novel piezo-electric transducers covering various frequency bands or all-

optical detectors. Using detectors covering different frequency bandwidths leads to interesting insights toward scalable imaging at high-resolution with deep penetration depth. Furthermore, another exciting possibility is the implementation of continuous raster scanning optoacoustic mesoscopy in the system. This can then be applied to biological samples labeled with reversibly switchable fluorescent proteins, which promises to further boost the imaging contrast-to-noise ratio by a factor of 50 [26, 27]. In regard to biological applications, developmental studies with larger genetically labeled structures are a promising first goal. The ability of the system to simultaneously monitor fluorescent and optoacoustic signals may also be exploited by imaging of dynamic fluorescent/optoacoucstic intensity changes such as of the activation of the calcium reporter gCamp, which has recently been exploited as a fluorescent tool to monitor brain activity of swimming zebrafish [190]. After systematically testing the technological feasibility of detecting relevant biological processes, cancer or tissue regeneration studies in model organisms such as zebrafish can be valuable applications.

On the spectroscopy side, further fine-tuning of the system is possible in terms of pulse energy correction (e.g. by implementing live pulse energy correction, possibly with a new fiber that allows 90:10 splitting of the incoming pulses). Live pulse energy correction promises to further improve the spectral quality and correlation between absorbance spectra and OA extinction spectra. Furthermore, the system holds great promise for the extension toward near-infrared applications, where OA spectra and bleaching of wide-spread dyes such as Indocyanine green can be characterized. The NIR range is also interesting in regard to the investigation of far-red reversibly switchable fluorescent proteins such as the promising BphP1 and its derivatives [26, 164]. Also in terms of optoacoustic imaging, the NIR window from 700-900 nm is particularly interesting due to the reduced Rayleigh scattering compared to the visible range. For the NIR extension, some technical challenges need to be addressed, such as the weaker pulse energies of the OPO laser in the NIR range, the coating of the optical elements and the stronger absorption of light by the surrounding water bath.

Overall, this thesis was dedicated to the advancements of high-resolution imaging of biological development in deep tissue by means of OA tomography and SPIM. Developing such tools may contribute to the better understanding of biological processes in deeper tissue layers.

List of Figures

List of Tables

Bibliography

[1] A. Van Leeuwenhoek, "Letter to Royal Society Of London," *J. Hist. Biol.*, vol. 16, pp. 185–224, 1676.

[2] E. Betzig, J. K. Trautman, T. D. Harris, and J. S. Weiner, "Breaking the Diffraction Barrier: Optical Microscopy on a Nanometric Scale," *Science*, vol. 251, no. 5000, pp. 1468–1470, 1991.

[3] S. W. Hell and J. Wichmann, "Stimulated-Emission-Depletion Fluorescence Microscopy," *Optics Letters*, vol. 19, no. 11, pp. 780–782, 1994.

[4] V. Ntziachristos, "Going deeper than microscopy: The optical imaging frontier in biology," *Nature Methods*, vol. 7, no. 8, pp. 603–614, 2010.

[5] L. V. Wang and H.-i. Wu, *Biomedical optics*. Wiley, 2007.

[6] L. V. Wang and S. Hu, "Photoacoustic tomography: In vivo imaging from organelles to organs," *Science*, vol. 335, no. 6075, pp. 1458–1462, 2012.

[7] P. J. Keller, "Imaging morphogenesis: Technological advances and biological insights," *Science*, vol. 340, no. 6137, p. 1234168, 2013.

[8] G. J. Lieschke and P. D. Currie, "Animal models of human disease: Zebrafish swim into view," *Nature Reviews Genetics*, vol. 8, no. 5, pp. 353–367, 2007.

[9] R. White, K. Rose, and L. Zon, "Zebrafish cancer: The state of the art and the path forward," *Nature Reviews Cancer*, vol. 13, no. 9, pp. 624–636, 2013.

[10] A. Seth, D. L. Stemple, and I. Barroso, "The emerging use of zebrafish to model metabolic disease," *Disease Models & Mechanisms*, vol. 6, no. 5, pp. 1080–1088, 2013.

[11] M. Kleinert, C. Clemmensen, S. M. Hofmann, M. C. Moore, S. Renner, S. C. Woods, P. Huypens, J. Beckers, M. H. De Angelis, A. Schürmann, M. Bakhti, M. Klingenspor, M. Heiman, A. D. Cherrington, M. Ristow, H. Lickert, E. Wolf, P. J. Havel, T. D. Müller, and M. H. Tschöp, "Animal models of obesity and diabetes mellitus," *Nature Reviews Endocrinology*, vol. 14, no. 3, pp. 140–162, 2018.

[12] D. M. Langenau and L. I. Zon, "The zebrafish: A new model of T-cell and thymic development," *Nature Reviews Immunology*, vol. 5, no. 4, pp. 307–317, 2005.

[13] M. Gemberling, T. J. Bailey, D. R. Hyde, and K. D. Poss, "The zebrafish as a model for complex tissue regeneration," *Trends in Genetics*, vol. 29, no. 11, pp. 611–620, 2013.

[14] C. A. MacRae and R. T. Peterson, "Zebrafish as tools for drug discovery," *Nature Reviews Drug Discovery*, vol. 14, no. 10, pp. 721–731, 2015.

[15] P. J. Keller, A. D. Schmidt, J. Wittbrodt, and E. H. K. Stelzer, "Reconstruction of Zebrafish Early Embryonic Development by Scanned Light Sheet Microscopy," *Science*, vol. 322, no. 5904, pp. 1065–1069, 2008.

[16] M. Mickoleit, B. Schmid, M. Weber, F. O. Fahrbach, S. Hombach, S. Reischauer, and J. Huisken, "High-resolution reconstruction of the beating zebrafish heart," *Nature Methods*, vol. 11, no. 9, pp. 919–922, 2014.

[17] D. Razansky, M. Distel, C. Vinegoni, R. Ma, N. Perrimon, R. W. Köster, and V. Ntziachristos, "Multispectral opto-acoustic tomography of deep-seated fluorescent proteins in vivo," *Nature Photonics*, vol. 3, no. 7, pp. 412–417, 2009.

[18] R. Ma, M. Distel, X. L. Deán-Ben, V. Ntziachristos, and D. Razansky, "Non-invasive whole-body imaging of adult zebrafish with optoacoustic tomography," *Physics in Medicine and Biology*, vol. 57, no. 22, pp. 7227–7237, 2012.

[19] M. Liu, N. Schmitner, M. G. Sandrian, B. Zabihian, B. Hermann, W. Salvenmoser, D. Meyer, and W. Drexler, "In vivo three dimensional dual wavelength photoacoustic tomography imaging of the far red fluorescent protein E2-Crimson expressed in adult zebrafish," *Biomedical Optics Express*, vol. 4, no. 10, p. 1846, 2013.

[20] N. Huang, H. Guo, W. Qi, Z. Zhang, J. Rong, Z. Yuan, W. Ge, H. Jiang, and L. Xi, "Whole-body multispetral photoacoustic imaging of adult zebrafish," *Biomedical Optics Express*, vol. 7, no. 9, p. 3543, 2016.

[21] G. Wurzinger, R. Nuster, N. Schmitner, S. Gratt, D. Meyer, and G. Paltauf, "Simultaneous three-dimensional photoacoustic and laser-ultrasound tomography," *Biomedical Optics Express*, vol. 4, no. 8, p. 1380, 2013.

[22] M. Omar, J. Rebling, K. Wicker, T. Schmitt-Manderbach, M. Schwarz, J. Gateau, H. López-Schier, T. Mappes, and V. Ntziachristos, "Optical imaging

of post-embryonic zebrafish using multi orientation raster scan optoacoustic mesoscopy," *Light: Science and Applications*, vol. 6, no. 1, pp. 1–6, 2017.

[23] P. Beard, "Biomedical photoacoustic imaging," *Interface Focus*, vol. 1, no. 4, pp. 602–631, 2011.

[24] J. Weber, P. C. Beard, and S. E. Bohndiek, "Contrast agents for molecular photoacoustic imaging," *Nature Methods*, vol. 13, no. 8, pp. 639–650, 2016.

[25] H. C. A. Lin, A. Chekkoury, M. Omar, T. Schmitt-Manderbach, B. Koberstein-Schwarz, T. Mappes, H. López-Schier, D. Razansky, and V. Ntziachristos, "Selective plane illumination optical and optoacoustic microscopy for postembryonic imaging," *Laser and Photonics Reviews*, vol. 9, no. 5, pp. L29–L34, 2015.

[26] J. Yao, A. A. Kaberniuk, L. Li, D. M. Shcherbakova, R. Zhang, L. Wang, G. Li, V. V. Verkhusha, and L. V. Wang, "Multiscale photoacoustic tomography using reversibly switchable bacterial phytochrome as a near-infrared photochromic probe," *Nature Methods*, vol. 13, no. 1, pp. 67–73, 2015.

[27] P. Vetschera, K. Mishra, J. P. Fuenzalida-Werner, A. Chmyrov, V. Ntziachristos, and A. C. Stiel, "Characterization of Reversibly Switchable Fluorescent Proteins in Optoacoustic Imaging," *Analytical Chemistry*, vol. 90, no. 17, pp. 10 527–10 535, 2018.

[28] D. Huang, E. A. Swanson, C. P. Lin, J. S. Schuman, W. G. Stinson, W. Chang, M. R. Hee, T. Flotte, K. Gregory, C. A. Puliafito, and J. G. Fujimoto, "Optical coherence tomography," *Science*, vol. 254, no. 5035, pp. 1178–1181, 1991.

[29] A. F. Fercher, W. Drexler, C. K. Hitzenberger, and T. Lasser, "Optical coherence tomography - Principles and applications," *Reports on Progress in Physics*, vol. 66, no. 2, pp. 239–303, 2003.

[30] S. H. Yun and S. J. J. Kwok, "Light in diagnosis, therapy and surgery," *Nature Biomedical Engineering*, vol. 1, no. 1, p. 0008, 2017.

[31] W. Demtröder, *Experimentalphysik 2*, ser. Experimentalphysik / Wolfgang Demtröder. Springer Berlin Heidelberg, 2005.

[32] L. Brillouin, "Diffusion de la lumière et des rayons X par un corps transparent homogène. Influence de l'agitation thermique," *Ann. Phys.(Paris)*, vol. 17, no. 88-122, p. 21, 1922.

[33] P. A. Tipler and G. Mosca, *Physik*. Elsevier, 2006.

[34] V. Ntziachristos, A. Leroy-Willig, and B. Tavitian, *Textbook of in vivo Imaging in Vertebrates*. J. Wiley & Sons, 2007.

[35] R. Savo, R. Pierrat, U. Najar, R. Carminati, S. Rotter, and S. Gigan, "Observation of mean path length invariance in light-scattering media," *Science*, vol. 358, no. 6364, pp. 765–768, 2017.

[36] L. V. Wang and J. Yao, "A practical guide to photoacoustic tomography in the life sciences," *Nature Methods*, vol. 13, no. 8, pp. 627–638, 2016.

[37] W. Demtröder, *Experimentalphysik 3: Atome, Moleküle und Festkörper*, ser. Experimentalphysik / Wolfgang Demtröder. Springer Berlin Heidelberg, 2005.

[38] S. Kellnberger, "Thermoacoustic Imaging in time and frequency domain. Theory and experiments," Ph.D. dissertation, Technical University of Munich, 2013.

[39] W. Demtröder, *Experimentalphysik 4*, ser. Experimentalphysik / Wolfgang Demtröder. Springer Berlin Heidelberg, 2005.

[40] G. Langer and T. Berer, "Influence of the excited state lifetimes on the photoacoustic signal," *Proceedings of the SPIE*, vol. 10494, no. 1049465, pp. 1–8, 2018.

[41] M. Kasha, "Characterization of electronic transitions in complex molecules," *Discussions of the Faraday Society*, vol. 9, pp. 14–19, 1950.

[42] J. W. Lichtman and J.-A. Conchello, "Fluorescence microscopy," *Nat. Methods*, vol. 2, no. 12, pp. 910–9, 2005.

[43] "https://omlc.org/spectra/hemoglobin/," nov 2018.

[44] "https://omlc.org/spectra/melanin/mua.html," nov 2018.

[45] "https://omlc.org/spectra/water/," nov 2018.

[46] C. L. Tsai, J. C. Chen, and W. J. Wang, "Near-infrared absorption property of biological soft tissue constituents," *Journal of Medical and Biological Engineering*, vol. 21, no. 1, pp. 7–14, 2001.

[47] X. L. Deán-Ben, S. Gottschalk, B. Mc Larney, S. Shoham, and D. Razansky, "Advanced optoacoustic methods for multiscale imaging of in vivo dynamics," *Chemical Society Reviews*, vol. 46, no. 8, pp. 2158–2198, 2017.

[48] X. Yang and E. Stein, "Nanoparticles for photoacoustic imaging," *Wiley Interdisciplinary*, vol. 1, no. 4, pp. 360–368, 2009.

[49] V. V. Verkhusha and K. A. Lukyanov, "The molecular properties and applications of Anthozoa fluorescent proteins and chromoproteins," *Nature Biotechnology*, vol. 22, no. 3, pp. 289–296, 2004.

[50] J. Lippincott-Schwartz and G. H. Patterson, "Development and use of fluorescent protein markers in living cells," *Science*, vol. 300, no. 5616, pp. 87–91, 2003.

[51] "http://www.tsienlab.ucsd.edu/Documents.htm," oct 2018.

[52] R. Heim and R. Y. Tsien, "Engineering green fluorescent protein for improved brightness, longer wavelengths and fluorescence resonance energy transfer," *Current Biology*, vol. 6, no. 2, pp. 178–182, 1996.

[53] R. Y. Tsien, "The Green Fluorescent Protein," *Annual Review of Biochemistry*, vol. 67, no. 1, pp. 509–544, 1998.

[54] D. Razansky, C. Vinegoni, and V. Ntziachristos, "Multispectral photoacoustic imaging of fluorochromes in small animals." *Optics letters*, vol. 32, no. 19, pp. 2891–2893, 2007.

[55] J. Brunker, J. Yao, J. Laufer, and S. E. Bohndiek, "Photoacoustic imaging using genetically encoded reporters: a review," *Journal of Biomedical Optics*, vol. 22, no. 7, p. 070901, 2017.

[56] M. Minsky, "Microscopy apparatus," 1961.

[57] R. H. Webb, "Confocal optical microscopy," *Reports on Progress in Physics*, vol. 59, no. 3, pp. 427–471, 1996.

[58] J. A. Conchello and J. W. Lichtman, "Optical sectioning microscopy," *Nature Methods*, vol. 2, no. 12, pp. 920–931, 2005.

[59] W. B. Amos and J. G. White, "How the confocal laser scanning microscope entered biological research," *Biology of the Cell*, vol. 95, no. 6, pp. 335–342, 2003.

[60] W. Denk, J. Strickler, and W. Webb, "Two-photon laser scanning fluorescence microscopy," *Science*, vol. 248, no. 4951, pp. 73–76, 1990.

[61] F. Helmchen and W. Denk, "Deep tissue two-photon microscopy," *Nature Methods*, vol. 2, no. 12, pp. 932–940, 2005.

[62] E. E. Hoover and J. A. Squier, "Advances in multiphoton microscopy technology," *Nature Photonics*, vol. 7, no. 2, pp. 93–101, 2013.

[63] J. Ripoll, B. Koberstein-Schwarz, and V. Ntziachristos, "Unleashing Optics and Optoacoustics for Developmental Biology," *Trends in Biotechnology*, vol. 33, no. 11, pp. 679–691, 2015.

[64] J. M. Schmitt, "Optical Coherence Tomography (OCT): a review," *IEEE Journal on Selected Topics in Quantum Electronics*, vol. 5, no. 4, pp. 1205–1215, 1999.

[65] J. A. Izatt, E. A. Swanson, J. G. Fujimoto, M. R. Hee, and G. M. Owen, "Optical coherence microscopy in scattering media," *Optics Letters*, vol. 19, no. 8, p. 590, 1994.

[66] J. Sharpe, U. Ahlgren, P. Perry, B. Hill, A. Ross, J. Hecksher-Sørensen, R. Baldock, and D. Davidson, "Optical projection tomography as a tool for 3D microscopy and gene expression studies," *Science*, vol. 296, no. 5567, pp. 541–545, 2002.

[67] J. Sharpe, "Optical projection tomography," *Advanced Imaging in Biology and Medicine: Technology, Software Environments, Applications*, pp. 199–224, 2009.

[68] ——, "Optical projection tomography as a new tool for studying embryo anatomy," *Journal of Anatomy*, vol. 202, no. 2, pp. 175–181, 2003.

[69] V. Ntziachristos, C. H. Tung, C. Bremer, and R. Weissleder, "Fluorescence molecular tomography resolves protease activity in vivo," *Nature Medicine*, vol. 8, no. 7, pp. 757–760, 2002.

[70] S. R. Arridge, "Optical tomography in medical imaging," *Inverse Problems*, vol. 15, no. 2, pp. R41–R93, 1999.

[71] C. Vinegoni, C. Pitsouli, D. Razansky, N. Perrimon, and V. Ntziachristos, "In vivo imaging of Drosophila melanogaster pupae with mesoscopic fluorescence tomography," *Nature Methods*, vol. 5, no. 1, pp. 45–47, 2008.

[72] J. Huisken, J. Swoger, F. Del Bene, J. Wittbrodt, and E. H. Stelzer, "Optical sectioning deep inside live embryos by selective plane illumination microscopy," *Science*, vol. 305, no. 5686, pp. 1007–1009, 2004.

[73] J. Huisken and D. Y. R. Stainier, "Selective plane illumination microscopy techniques in developmental biology," *Development*, vol. 136, no. 12, pp. 1963–1975, 2009.

[74] S. Preibisch, S. Saalfeld, J. Schindelin, and P. Tomancak, "Software for bead-

based registration of selective plane illumination microscopy data," *Nature Methods*, vol. 7, no. 6, pp. 418–419, 2010.

[75] S. Preibisch, F. Amat, E. Stamataki, M. Sarov, R. H. Singer, E. Myers, and P. Tomancak, "Efficient bayesian-based multiview deconvolution," *Nature Methods*, vol. 11, no. 6, pp. 645–648, 2014.

[76] A. G. Bell, "On the production and reproduction of sound by light," *American Journal of Science*, vol. 3, no. 20, pp. 305–324, 1880.

[77] G. J. Diebold, T. Sun, and M. I. Khan, "Photoacoustic monopole radiation in one, two, and three dimensions," *Physical Review Letters*, vol. 67, no. 24, pp. 3384–3387, 1991.

[78] I. G. Calasso, W. Craig, and G. J. Diebold, "Photoacoustic point source," *Physical Review Letters*, vol. 86, no. 16, pp. 3550–3553, 2001.

[79] G. J. Diebold, M. I. Khan, and S. M. Park, "Photoacoustic "signatures" of particulate matter: Optical production of acoustic monopole radiation," *Science*, vol. 250, no. 4977, pp. 101–104, 1990.

[80] C. Li and L. V. Wang, "Photoacoustic tomography and sensing in biomedicine," *Physics in Medicine and Biology*, vol. 54, no. 19, pp. 319–335, 2009.

[81] B. E. Treeby and B. T. Cox, "Fast tissue-realistic models of photoacoustic wave propagation for homogeneous attenuating media," *Proceedings of the SPIE*, vol. 7177, no. 717716, pp. 1–10, 2009.

[82] X. L. Deán-Ben, D. Razansky, and V. Ntziachristos, "The effects of acoustic attenuation in optoacoustic signals," *Physics in Medicine and Biology*, vol. 56, no. 18, pp. 6129–6148, 2011.

[83] A. M. Winkler, K. Maslov, and L. V. Wang, "Noise-equivalent sensitivity of photoacoustics," *Journal of Biomedical Optics*, vol. 18, no. 9, pp. 0 970 031–10, 2013.

[84] G. Wissmeyer, M. A. Pleitez, A. Rosenthal, and V. Ntziachristos, "Looking at sound: optoacoustics with all-optical ultrasound detection," *Light: Science and Applications*, vol. 7, no. 1, pp. 53–69, 2018.

[85] E. Zhang, J. Laufer, and P. Beard, "Backward-mode multiwavelength photoacoustic scanner using a planar Fabry-Perot polymer film ultrasound sensor for high-resolution three-dimensional imaging of biological tissues," *Applied Optics*, vol. 47, no. 4, pp. 561–577, 2008.

[86] E. Z. Zhang, B. Povazay, J. Laufer, A. Alex, B. Hofer, B. Pedley, C. Glittenberg, B. Treeby, B. Cox, P. Beard, and W. Drexler, "Multimodal photoacoustic and optical coherence tomography scanner using an all optical detection scheme for 3D morphological skin imaging," *Biomedical Optics Express*, vol. 2, no. 8, pp. 2202–2215, 2011.

[87] A. Rosenthal, D. Razansky, and V. Ntziachristos, "High-sensitivity compact ultrasonic detector based on a pi-phase-shifted fiber Bragg grating," *Optics Letters*, vol. 36, no. 10, pp. 1833–1835, 2011.

[88] A. Rosenthal, M. Omar, H. Estrada, S. Kellnberger, D. Razansky, and V. Ntziachristos, "Embedded ultrasound sensor in a silicon-on-insulator photonic platform," *Applied Physics Letters*, vol. 104, no. 2, pp. 0 211 161–4, 2014.

[89] R. Shnaiderman, G. Wissmeyer, M. Seeger, D. Soliman, H. Estrada, D. Razansky, A. Rosenthal, and V. Ntziachristos, "Fiber interferometer for hybrid optical and optoacoustic intravital microscopy," *Optica*, vol. 4, no. 10, pp. 1180–1187, 2017.

[90] C.-y. Chao, S. Ashkenazi, S.-w. Huang, M. O. Donnell, and L. J. Guo, "High-Frequency Ultrasound Sensors Using," *IEEE Transactions on Ultrasonics, Ferroelectrics, and Frequency Control*, vol. 54, no. 5, pp. 957–965, 2007.

[91] A. Maxwell, S. W. Huang, T. Ling, J. S. Kim, S. Ashkenazi, and L. J. Guo, "Polymer microring resonators for high-frequency ultrasound detection and imaging," *IEEE Journal on Selected Topics in Quantum Electronics*, vol. 14, no. 1, pp. 191–197, 2008.

[92] K. K. Shung and M. J. Zipparo, "Ultrasonic transducers and arrays," *IEEE Engineering in Medicine and Biology Magazine*, vol. 15, no. 6, pp. 20–30, 1996.

[93] E. Benes, M. Gröschl, W. Burger, and M. Schmid, "Sensors based on piezoelectric resonators," *Sensors and Actuators A: Physical*, vol. 48, no. 1, pp. 1–21, 1995.

[94] S. Michau, P. Mauchamp, and R. Dufait, "Piezocomposite 30MHz linear array for medical imaging: design challenges and performances evaluation of a 128 elements array," *IEEE Ultrasonics Symposium*, vol. 2, pp. 898–901, 2004.

[95] H. W. Persson and C. H. Hertz, "Acoustic impedance matching of medical ultrasound transducers," *Ultrasonics*, vol. 23, no. 2, pp. 83–89, 1985.

[96] T. D. Khokhlova, I. M. Pelivanov, and A. A. Karabutov, "Optoacoustic tomography utilizing focused transducers: The resolution study," *Applied Physics Letters*, vol. 92, no. 2, pp. 2–5, 2008.

[97] R. Bouchard, O. Sahin, and S. Emelianov, "Ultrasound-guided photoacoustic imaging: Current state and future development," *IEEE Transactions on Ultrasonics, Ferroelectrics, and Frequency Control*, vol. 61, no. 3, pp. 450–466, 2014.

[98] J. Rebling, O. Warshavski, C. Meynier, and D. Razansky, "Optoacoustic characterization of broadband directivity patterns of capacitive micromachined ultrasonic transducers," *Journal of Biomedical Optics*, vol. 22, no. 4, pp. 0 410 051–9, 2016.

[99] I. Ladabaum, X. Jin, H. T. Soh, A. Atalar, and B. T. Khuri-Yakub, "Surface micromachined capacitive ultrasonic transducers," *IEEE Transactions on Ultrasonics, Ferroelectrics, and Frequency Control*, vol. 45, no. 3, pp. 678–690, 1998.

[100] X. Jin, I. Ladabaum, and B. T. Khuri-Yakub, "The microfabrication of capacitive ultrasonic transducers," *Journal of Microelectromechanical Systems*, vol. 7, no. 3, pp. 295–302, 1998.

[101] J. Rebling, O. Warshavski, C. Meynier, and D. Razansky, "Broadband optoacoustic characterization of cMUT and PZT transducer directivity in receive mode," *Proceedings of the SPIE*, vol. 10139, no. 101391K, pp. 1–7, 2017.

[102] J. Xia, J. Yao, and L. H. V. Wang, "Photoacoustic tomography: principles and advances," *Progress In Electromagnetics Research*, vol. 147, pp. 1–22, 2014.

[103] J. Yao and L. V. Wang, "Photoacoustic Microscopy," *Laser Photon Rev*, vol. 7, no. 5, pp. 1–36, 2012.

[104] M. Omar, J. Gateau, and V. Ntziachristos, "Raster-scan optoacoustic mesoscopy in the 25–125 MHz range," *Optics Letters*, vol. 38, no. 14, p. 2472, 2013.

[105] M. Omar, D. Soliman, J. Gateau, and V. Ntziachristos, "Ultrawideband reflection-mode optoacoustic mesoscopy." *Optics letters*, vol. 39, no. 13, pp. 3911–4, 2014.

[106] X. Wang, Y. Pang, G. Ku, X. Xie, G. Stoica, and L. V. Wang, "Noninvasive

laser-induced photoacoustic tomography for structural and functional in vivo imaging of the brain," *Nature Biotechnology*, vol. 21, no. 7, pp. 803–806, 2003.

[107] R. Ma, A. Taruttis, V. Ntziachristos, and D. Razansky, "Multispectral optoacoustic tomography (MSOT) scanner for whole-body small animal imaging," *Optics Express*, vol. 17, no. 24, pp. 21 414–21 426, 2009.

[108] R. J. Zemp, L. Song, R. Bitton, K. K. Shung, and L. V. Wang, "Realtime photoacoustic microscopy in vivo with a 30-MHz ultrasound array transducer," *Optics Express*, vol. 16, no. 11, pp. 7915–7928, 2008.

[109] T. N. Erpelding, C. Kim, M. Pramanik, L. Jankovic, K. Maslov, Z. Guo, J. A. Margenthaler, M. D. Pashley, and L. V. Wang, "Sentinel Lymph Nodes in the Rat: Noninvasive Photoacoustic and US Imaging with a Clinical US System," *Radiology*, vol. 256, no. 1, pp. 102–110, 2010.

[110] J. Gateau, M. Á. A. Caballero, A. Dima, and V. Ntziachristos, "Three-dimensional optoacoustic tomography using a conventional ultrasound linear detector array: Whole-body tomographic system for small animals," *Medical Physics*, vol. 40, no. 1, pp. 0 133 021–11, 2013.

[111] J. Gateau, A. Chekkoury, and V. Ntziachristos, "High-resolution optoacoustic mesoscopy with a 24 MHz multidetector translate-rotate scanner," *Journal of Biomedical Optics*, vol. 18, no. 10, pp. 1 060 051–10, 2013.

[112] Y. Wang, T. N. Erpelding, L. Jankovic, Z. Guo, J.-L. Robert, G. David, and L. V. Wang, "In vivo three-dimensional photoacoustic imaging based on a clinical matrix array ultrasound probe," *Journal of Biomedical Optics*, vol. 17, no. 6, pp. 0 612 081–5, 2012.

[113] X. L. Deán-Ben and D. Razansky, "Adding fifth dimension to optoacoustic imaging: Volumetric time-resolved spectrally enriched tomography," *Light: Science and Applications*, vol. 3, no. May 2013, pp. 1–5, 2014.

[114] X. L. Deán-Ben, H. López-Schier, and D. Razansky, "Optoacoustic micro-tomography at 100 volumes per second," *Scientific Reports*, vol. 7, no. 1, pp. 1–8, 2017.

[115] X. L. Deán-Ben, T. F. Fehm, S. J. Ford, S. Gottschalk, and D. Razansky, "Spiral volumetric optoacoustic tomography visualizes multi-scale dynamics in mice," *Light: Science and Applications*, vol. 6, no. 4, pp. 1–8, 2017.

[116] A. Rosenthal, V. Ntziachristos, and D. Razansky, "Acoustic Inversion in

Optoacoustic Tomography: A Review," *Current Medical Imaging Reviews*, vol. 9, no. 4, pp. 318–336, 2013.

[117] V. Ntziachristos and D. Razansky, "Molecular imaging by means of multispectral optoacoustic tomography (MSOT)," *Chemical Reviews*, vol. 110, no. 5, pp. 2783–2794, 2010.

[118] A. Rosenthal, "Algebraic determination of back-projection operators for optoacoustic tomography," *Biomedical Optics Express*, vol. 9, no. 11, pp. 5173–5193, 2018.

[119] G. Paltauf, J. A. Viator, S. A. Prahl, and S. L. Jacques, "Iterative reconstruction algorithm for optoacoustic imaging," *The Journal of the Acoustical Society of America*, vol. 112, no. 4, pp. 1536–1544, 2002.

[120] A. Rosenthal, D. Razansky, and V. Ntziachristos, "Fast semi-analytical model-based acoustic inversion for quantitative optoacoustic tomography," *IEEE Transactions on Medical Imaging*, vol. 29, no. 6, pp. 1275–1285, 2010.

[121] X. L. Dean-Ben, A. Buehler, V. Ntziachristos, and D. Razansky, "Accurate model-based reconstruction algorithm for three-dimensional optoacoustic tomography," *IEEE Transactions on Medical Imaging*, vol. 31, no. 10, pp. 1922–1928, 2012.

[122] M. A. A. Caballero, A. Rosenthal, A. Buehler, D. Razansky, and V. Ntziachristos, "Optoacoustic determination of spatio-temporal responses of ultrasound sensors," *IEEE Transactions on Ultrasonics, Ferroelectrics, and Frequency Control*, vol. 60, no. 6, pp. 1234–1244, 2013.

[123] M. A. Áraque Caballero, J. Gateau, X. L. Dean-Ben, and V. Ntziachristos, "Model-based optoacoustic image reconstruction of large three-dimensional tomographic datasets acquired with an array of directional detectors," *IEEE Transactions on Medical Imaging*, vol. 33, no. 2, pp. 433–443, 2014.

[124] M. Goitein, M. Abrams, D. Rowell, H. Pollari, and J. Wiles, "Multi-dimensional treatment planning: II. Beam's eye-view, back projection, and projection through CT sections," *International Journal of Radiation Oncology • Biology • Physics*, vol. 9, no. 6, pp. 789 – 797, 1983.

[125] W. A. Kalender, "X-ray computed tomography," *Physics in Medicine and Biology*, vol. 51, no. 13, pp. R29–R43, 2006.

[126] R. A. Kruger, P. Liu, Y. R. Fang, and C. R. Appledorn, "Photoacoustic ultrasound (PAUS)—Reconstruction tomography," pp. 1605–1609, 1995.

[127] M. Xu and L. V. Wang, "Universal back-projection algorithm for photoacoustic computed tomography," *Physical Review E - Statistical, Nonlinear, and Soft Matter Physics*, vol. 71, no. 1, pp. 1–7, 2005.

[128] L. Wang, *Photoacoustic Imaging and Spectroscopy*. CRC Press, 2009.

[129] C. G. A. Hoelen and F. F. M. de Mul, "Image reconstruction for photoacoustic scanning of tissue structures," *Applied Optics*, vol. 39, no. 31, p. 5872, 2000.

[130] M. Xu and L. V. Wang, "Photoacoustic imaging in biomedicine," *Review of Scientific Instruments*, vol. 77, no. 4, pp. 041 101–22, 2006.

[131] ——, "Analytic explanation of spatial resolution related to bandwidth and detector aperture size in thermoacoustic or photoacoustic reconstruction," *Physical Review E*, vol. 67, no. 5, p. 15, 2003.

[132] N. Keshava and J. Mustard, "Spectral unmixing," *IEEE Signal Processing Magazine*, vol. 19, no. 1, pp. 44–57, 2002.

[133] N. Keshava, "A Survey of Spectral Unmixing Algorithms," *Lincoln Laboratory Journal*, vol. 14, no. 1, pp. 55–78, 2003.

[134] S. Tzoumas, N. Deliolanis, S. Morscher, and V. Ntziachristos, "Unmixing molecular agents from absorbing tissue in multispectral optoacoustic tomography," *IEEE Transactions on Medical Imaging*, vol. 33, no. 1, pp. 48–60, 2014.

[135] B. Cox, J. G. Laufer, S. R. Arridge, and P. C. Beard, "Quantitative spectroscopic photoacoustic imaging: a review," *Journal of Biomedical Optics*, vol. 17, no. 6, pp. 0 612 021–22, 2012.

[136] J. Glatz, N. C. Deliolanis, A. Buehler, D. Razansky, and V. Ntziachristos, "Blind source unmixing in multi-spectral optoacoustic tomography," *Optics Express*, vol. 19, no. 4, pp. 3175–3184, 2011.

[137] D. Razansky, "Multispectral optoacoustic tomography-volumetric color hearing in real time," *IEEE Journal on Selected Topics in Quantum Electronics*, vol. 18, no. 3, pp. 1234–1243, 2012.

[138] S. Tzoumas, A. Nunes, I. Olefir, S. Stangl, P. Symvoulidis, S. Glasl, C. Bayer, G. Multhoff, and V. Ntziachristos, "Eigenspectra optoacoustic tomography achieves quantitative blood oxygenation imaging deep in tissues," *Nature Communications*, vol. 7, no. 12121, pp. 1–10, 2016.

[139] P. Vetschera, B. Koberstein-Schwarz, T. Schmitt-Manderbach, C. Dietrich, W. Hellmich, A. Chekkoury, P. Symvoulidis, J. Reber, G. Westmeyer,

H. López-Schier, M. Omar, and V. Ntziachristos, "Beyond early development: observing zebrafish over 6 weeks with hybrid optical and optoacoustic imaging," *bioRxiv*, p. 586933, 2019.

[140] L. K. Mathew, S. Sengupta, A. Kawakami, E. A. Andreasen, C. V. Löhr, C. A. Loynes, S. A. Renshaw, R. T. Peterson, and R. L. Tanguay, "Unraveling tissue regeneration pathways using chemical genetics," *Journal of Biological Chemistry*, vol. 282, no. 48, pp. 35 202–35 210, 2007.

[141] H. Feitsma and E. Cuppen, "Zebrafish as a Cancer Model," *Mol Cancer Res*, vol. 6, no. 5, pp. 685–94, 2008.

[142] David M Langenau, *Cancer and Zebrafish*. Springer, Cham, 2016, vol. 916.

[143] R. Fior, V. Póvoa, R. V. Mendes, T. Carvalho, A. Gomes, N. Figueiredo, and M. G. Ferreira, "Single-cell functional and chemosensitive profiling of combinatorial colorectal therapy in zebrafish xenografts," *Proceedings of the National Academy of Sciences*, vol. 114, no. 39, pp. E8234–E8243, 2017.

[144] A. Chekkoury, J. Gateau, and V. Ntziachristos, "Multiple bandwidth volumetric optoacoustic tomography using conventional ultrasound linear arrays," *European Conferences on Biomedical Optics*, vol. 8800, no. 1, pp. 88 001–4, 2013.

[145] A. Chekkoury, J. Gateau, W. Driessen, P. Symvoulidis, N. Bézière, A. Feuchtinger, A. Walch, and V. Ntziachristos, "Optical mesoscopy without the scatter: broadband multispectral optoacoustic mesoscopy," *Biomedical Optics Express*, vol. 6, no. 9, pp. 3134–3148, 2015.

[146] A. Chekkoury, A. Nunes, J. Gateau, P. Symvoulidis, A. Feuchtinger, N. Beziere, S. V. Ovsepian, A. Walch, and V. Ntziachristos, "High-Resolution Multispectral Optoacoustic Tomography of the Vascularization and Constitutive Hypoxemia of Cancerous Tumors," *Neoplasia (United States)*, vol. 18, no. 8, pp. 459–467, 2016.

[147] B. Koberstein-Schwarz, "Hybrid selective plane illumination microscopy and optoacoustic mesoscopy," Ph.D. dissertation, Technical University of Munich, 2017.

[148] "https://www.pco.de/scmos-cameras/pcoedge-55/," dec 2019.

[149] ISO Standard 11146-1:2005(E), "Laser beam test methods," 2005.

[150] U. Leischner, W. Zieglgänsberger, and H. U. Dodt, "Resolution of ultrami-

croscopy and field of view analysis," *PLoS ONE*, vol. 4, no. 6, pp. 1435–1439, 2009.

[151] S. Kedenburg, M. Vieweg, T. Gissibl, and H. Giessen, "Linear refractive index and absorption measurements of nonlinear optical liquids in the visible and near-infrared spectral region," *Optical Materials Express*, vol. 2, no. 11, pp. 1588–1611, 2012.

[152] C. Chen, C. M. Cohrs, J. Stertmann, R. Bozsak, and S. Speier, "Human beta cell mass and function in diabetes: Recent advances in knowledge and technologies to understand disease pathogenesis," *Molecular Metabolism*, vol. 6, no. 9, pp. 943–957, 2017.

[153] R. Y. Tsien, "Imagining imaging's future." *Nature Cell Biology*, vol. 4, pp. SS16–21, 2003.

[154] J. A. Jensen, "FIELD: A Program for Simulating Ultrasound Systems," *10th Nordic-Baltic Conference on Biomedical Imaging*, vol. 4, no. 1, pp. 351–353, 1996.

[155] M. A. Pleitez, A. A. Khan, J. Reber, A. Chmyrov, M. Seeger, M. Scheideler, S. Herzig, and V. Ntziachristos, "Mid-infrared optoacoustic microscopy with label-free chemical contrast in living cells and tissues," *bioRxiv*, p. 270082, 2018.

[156] G. J. Tserevelakis, D. Soliman, M. Omar, and V. Ntziachristos, "Hybrid multiphoton and optoacoustic microscope," *Optics Letters*, vol. 39, no. 7, pp. 1819–1822, 2014.

[157] A. Chekkoury, "3D mesoscopic scale optoacoustic imaging using linear array transducers," Ph.D. dissertation, Technical University of Munich, 2016.

[158] R. Heim, D. C. Prasher, and R. Y. Tsien, "Wavelength mutations and posttranslational autoxidation of green fluorescent protein." *Proceedings of the National Academy of Sciences*, vol. 91, no. 26, pp. 12 501–12 504, 1994.

[159] G. H. Patterson, S. M. Knobel, W. D. Sharif, S. R. Kain, and D. W. Piston, "Use of the green fluorescent protein and its mutants in quantitative fluorescence microscopy," *Biophysical Journal*, vol. 73, no. 5, pp. 2782–2790, 1997.

[160] J. D. Pédelacq, S. Cabantous, T. Tran, T. C. Terwilliger, and G. S. Waldo, "Engineering and characterization of a superfolder green fluorescent protein," *Nature Biotechnology*, vol. 24, no. 1, pp. 79–88, 2006.

[161] A. C. Stiel, X. L. Deán-Ben, Y. Jiang, V. Ntziachristos, D. Razansky, and G. G. Westmeyer, "High-contrast imaging of reversibly switchable fluorescent proteins via temporally unmixed multispectral optoacoustic tomography," *Optics Letters*, vol. 40, no. 3, pp. 367–370, 2015.

[162] X. L. Deán-Ben, A. C. Stiel, Y. Jiang, V. Ntziachristos, G. G. Westmeyer, and D. Razansky, "Light fluence normalization in turbid tissues via temporally unmixed multispectral optoacoustic tomography," *Optics letters*, vol. 40, no. 20, pp. 4691–4694, 2015.

[163] J. Märk, H. Dortay, A. Wagener, E. Zhang, J. Buchmann, C. Grötzinger, T. Friedrich, and J. Laufer, "Dual-wavelength 3D photoacoustic imaging of mammalian cells using a photoswitchable phytochrome reporter protein," *Communications Physics*, vol. 1, no. 1, pp. 1–10, 2018.

[164] L. Li, A. A. Shemetov, M. Baloban, P. Hu, L. Zhu, D. M. Shcherbakova, R. Zhang, J. Shi, J. Yao, L. V. Wang, and V. V. Verkhusha, "Small near-infrared photochromic protein for photoacoustic multi-contrast imaging and detection of protein interactions in vivo," *Nature Communications*, vol. 9, no. 1, pp. 1–14, 2018.

[165] S. W. Hell, "Microscopy and its focal switch," *Nature Methods*, vol. 6, no. 1, pp. 24–32, 2009.

[166] M. Andresen, A. C. Stiel, J. Fölling, D. Wenzel, A. Schönle, A. Egner, C. Eggeling, S. W. Hell, and S. Jakobs, "Photoswitchable fluorescent proteins enable monochromatic multilabel imaging and dual color fluorescence nanoscopy," *Nature Biotechnology*, vol. 26, no. 9, pp. 1035–1040, 2008.

[167] M. L. Veingerov, "New method of gas analysis based on Tyndall-Röntgen optic-acoustic effect," *Dokl. Akad. Nauk. USSR*, vol. 19, pp. 687–688, 1938.

[168] A. Rosencwaig, "Photoacoustic spectroscopy of biological materials." *Science (New York, N.Y.)*, vol. 181, no. 100, pp. 657–658, 1973.

[169] ——, "Photoacoustic Spectroscopy. New Tool for Investigation of Solids," *Analytical Chemistry*, vol. 47, no. 6, pp. 592A–604A, 1975.

[170] A. Rosencwaig and A. Gersho, "Theory of photoacoustic effect with solids," *Journal of Applied Physics*, vol. 47, no. 1, pp. 64–69, 1976.

[171] J. Laufer, A. Jathoul, M. Pule, and P. Beard, "In vitro characterization of genetically expressed absorbing proteins using photoacoustic spectroscopy," *Biomedical Optics Express*, vol. 4, no. 11, pp. 2477–2490, 2013.

[172] S. Abbruzzetti, C. Viappiani, D. H. Murgida, R. Erra-Balsells, and G. M. Bilmes, "Non-toxic, water-soluble photocalorimetric reference compounds for UV and visible excitation," *Chemical Physics Letters*, vol. 304, no. 3-4, pp. 167–172, 1999.

[173] H. Chen and G. Diebold, "Chemical Generation of Acoustic Waves: A Giant Photoacoustic Effect," *Science*, vol. 270, no. 5238, pp. 963–966, 1995.

[174] R. Ando, H. Mizuno, and A. Miyawaki, "Regulated fast nucleocytoplasmic shuttling observed by reversible protein highlighting," *Science*, vol. 306, no. 5700, pp. 1370–1373, 2004.

[175] A. C. Stiel, S. Trowitzsch, G. Weber, M. Andresen, C. Eggeling, S. W. Hell, S. Jakobs, and M. C. Wahl, "1.8 Å bright-state structure of the reversibly switchable fluorescent protein Dronpa guides the generation of fast switching variants," *Biochemical Journal*, vol. 402, no. 1, pp. 35–42, 2007.

[176] R. Ando, C. Flors, H. Mizuno, J. Hofkens, and A. Miyawaki, "Highlighted generation of fluorescence signals using simultaneous two-color irradiation on Dronpa mutants," *Biophysical Journal*, vol. 92, no. 12, pp. L97–L99, 2007.

[177] T. Grotjohann, I. Testa, M. Reuss, T. Brakemann, C. Eggeling, S. W. Hell, and S. Jakobs, "rsEGFP2 enables fast RESOLFT nanoscopy of living cells," *eLife*, vol. 2012, no. 1, pp. 1–14, 2012.

[178] A. C. Stiel, M. Andresen, H. Bock, M. Hilbert, J. Schilde, A. Schönle, C. Eggeling, A. Egner, S. W. Hell, and S. Jakobs, "Generation of monomeric reversibly switchable red fluorescent proteins for far-field fluorescence nanoscopy," *Biophysical Journal*, vol. 95, no. 6, pp. 2989–2997, 2008.

[179] F. Lavoie-Cardinal, N. A. Jensen, V. Westphal, A. C. Stiel, A. Chmyrov, J. Bierwagen, I. Testa, S. Jakobs, and S. W. Hell, "Two-color RESOLFT nanoscopy with green and red fluorescent photochromic proteins," *ChemPhysChem*, vol. 15, no. 4, pp. 655–663, 2014.

[180] F. V. Subach, L. Zhang, T. W. J. Gadella, N. G. Gurskaya, K. A. Lukyanov, and V. V. Verkhusha, "Red fluorescent protein with reversibly photoswitchable absorbance for photochromic FRET," *Chemistry and Biology*, vol. 17, no. 7, pp. 745–755, 2010.

[181] D. M. Shcherbakova, P. Sengupta, J. Lippincott-Schwartz, and V. V. Verkhusha, "Photocontrollable Fluorescent Proteins for Superresolution Imaging," *Annual Review of Biophysics*, vol. 43, no. 1, pp. 303–329, 2014.

[182] X. X. Zhou and M. Z. Lin, "Photoswitchable fluorescent proteins: Ten years of colorful chemistry and exciting applications," *Current Opinion in Chemical Biology*, vol. 17, no. 4, pp. 682–690, 2013.

[183] A. Stylogiannis, L. Prade, A. Buehler, J. Aguirre, G. Sergiadis, and V. Ntziachristos, "Continuous wave laser diodes enable fast optoacoustic imaging," *Photoacoustics*, vol. 9, pp. 31–38, 2018.

[184] S. Roberts, M. Seeger, Y. Jiang, A. Mishra, F. Sigmund, A. Stelzl, A. Lauri, P. Symvoulidis, H. Rolbieski, M. Preller, X. L. Deán-Ben, D. Razansky, T. Orschmann, S. C. Desbordes, P. Vetschera, T. Bach, V. Ntziachristos, and G. G. Westmeyer, "Calcium Sensor for Photoacoustic Imaging," *Journal of the American Chemical Society*, vol. 140, no. 8, pp. 2718–2721, 2018.

[185] E. A. Rodriguez, G. N. Tran, L. A. Gross, J. L. Crisp, X. Shu, J. Y. Lin, and R. Y. Tsien, "A far-red fluorescent protein evolved from a cyanobacterial phycobiliprotein," *Nature Methods*, vol. 13, no. 9, 2016.

[186] J. P. Fuenzalida-Werner, K. Mishra, P. Vetschera, Y. Huang, K. Richter, V. Ntziachristos, and A. C. Stiel, "A louder smURFP: Semi-rational site-directed mutagenesis of the phycobiliprotein smURFP for optoacoustics," *in preparation*, 2019.

[187] W.-l. Ding, D. Miao, Y.-n. Hou, S.-p. Jiang, B.-q. Zhao, M. Zhou, H. Scheer, and K.-h. Zhao, "BBA - Molecular Cell Research Small monomeric and highly stable near-infrared fluorescent markers derived from the thermophilic phycobiliprotein , ApcF2," *BBA - Molecular Cell Research*, vol. 1864, no. 10, pp. 1877–1886, 2017.

[188] S. W. Hell, "Toward fluorescence nanoscopy," *Nature Biotechnology*, vol. 21, no. 11, pp. 1347–1355, 2003.

[189] M. Hofmann, C. Eggeling, S. Jakobs, and S. W. Hell, "Breaking the diffraction barrier in fluorescence microscopy at low light intensities by using reversibly photoswitchable proteins," *Proceedings of the National Academy of Sciences*, vol. 102, no. 49, pp. 17 565–17 569, 2005.

[190] P. Symvoulidis, A. Lauri, A. Stefanoiu, M. Cappetta, S. Schneider, H. Jia, A. Stelzl, M. Koch, C. C. Perez, A. Myklatun, S. Renninger, A. Chmyrov, T. Lasser, W. Wurst, V. Ntziachristos, and G. G. Westmeyer, "NeuBtracker - Imaging neurobehavioral dynamics in freely behaving fish," *Nature Methods*, vol. 14, no. 11, pp. 1079–1082, 2017.

List of publications

Journal publications

1. J.P. Fuenzalida-Werner, K. Mishra, **P. Vetschera**, Y. Huang, K. Richter, V. Ntziachristos, A.C. Stiel, "A louder smURFP: Semi-rational site-directed mutagenesis of the phycobiliprotein smURFP for optoacoustics", *in preparation.*

2. J.Li, A. Chekkoury, J. Prakash, S. Glasl, **P. Vetschera**, B. Koberstein-Schwarz, I. Olefir, V. Gujrati, M. Omar, V. Ntziachristos, "Spatial heterogeneity of oxygenation and hemodynamics in breast cancer resolved in vivo by conical multispectral optoacoustic mesoscopy ", *in preparation.*

3. **P. Vetschera**, B. Koberstein-Schwarz, T. Schmitt-Manderbach, C. Dietrich, W. Hellmich, A. Chekkoury, P. Symvoulidis, G. G. Westmeyer, H. López-Schier, M. Omar, Vasilis Ntziachristos, "Beyond early development: observing zebrafish over 6 weeks with hybrid optical and optoacoustic imaging", *bioRxiv*, p. 586933, 2019.

4. **P. Vetschera**, K. Mishra, J. P. Fuenzalida-Werner, A. Chmyrov, V. Ntziachristos, and A. C. Stiel, "Characterization of Reversibly Switchable Fluorescent Proteins in Optoacoustic Imaging", *Analytical Chemistry*, vol. 90, no. 17, pp. 10527-10535, 2018.

5. S. Roberts, M. Seeger, Y. Jiang, A. Mishra, F. Sigmund, A. Stelzl, A. Lauri, P. Symvoulidis, H. Rolbieski, M. Preller, X. L. Deán-Ben, D. Razansky, T. Orschmann, S. C. Desbordes, **P. Vetschera**, T. Bach, V. Ntziachristos, and G. G. Westmeyer, "Calcium Sensor for Photoacoustic Imaging", *Journal of the American Chemical Society*, vol. 140, no. 8, pp. 2718-2721, 2018.

Conference proceedings

1. Y. Huang, J.P. Fuenzalida-Werner, K. Mishra, **P. Vetschera**, Y. Huang, A. Chmyrov, V. Ntziachristos, A.C. Stiel, "Analytical Optoacoustic Spectrometer", *in preparation.*

2. J. Li, S. Zhang, A. Chekkoury, S. Glasl, **P. Vetschera**, B. Koberstein-Schwarz, M. Omar, V. Ntziachristos, "Three-dimensional optoacoustic mesoscopy of the tumor heterogeneity in vivo using high depth-to-resolution multispectral optoacoustic tomography", *Proc. SPIE 10064, Photons Plus Ultrasound: Imaging and Sensing, 2017*, 100643C, 2017.